THEORETICAL AND COMPUTATIONAL ANALYSIS OF UNSTEADY FLOW OVER AN ASYMMETRIC AIRFOIL

By

Shiwei Qin

A DISSERTATION

Submitted to
Michigan State University
in partial fulfillment of the requirement
for the degree of

DOCTOR OF PHILOSOPHY

Mechanical Engineering

2012

ABSTRACT

THEORETICAL AND COMPUTATIONAL ANALYSIS OF UNSTEADY FLOW OVER AN ASYMMETRIC AIRFOIL

By

Shiwei Qin

Various methods are employed for studying steady and unsteady flows over an asymmetric SD7003 airfoil. First, linear stability methods are used for the investigation of airfoil flow stability. Second, flows over the stationary airfoil with steady and unsteady freestream conditions are computed by the large eddy simulation (LES) method.

The laminar separation bubble (LSB) region of the airfoil flow at Reynolds number of 60,000 and angle of attack (AoA) of 4° is analyzed by the local and global stability methods. Both methods correctly predict that the flow is unstable and transitions to turbulence at these conditions. The maximum growth rates predicted by the two methods are in agreement.

The LES results for several steady freestream flows are shown to be consistent with the available experimental and numerical data, and then three types of unsteady freestream flows are simulated by the LES method. In the first type, the AoA is fixed at 4°, while the freestream velocity magnitude varies harmonically with a mean Reynolds number of 60,000, reduced frequency from $\pi/8$ to 2π, and amplitudes of 0.183 and 0.366 of the mean velocity. In the second type of unsteady flows, the freestream velocity magnitude is fixed at Reynolds number of 60,000, but the AoA varies harmonically with a mean value of 4°, reduced frequency from $\pi/8$ to 2π, and amplitudes of 4° and 8°. In the third type of unsteady flow, a wind gust model is employed.

For the flows with oscillating freestream velocity magnitude, the effect of freestream unsteadiness on the aerodynamic forces, vorticity field, velocity fluctuations, and boundary layer

separation and reattachment are studied. The vorticity plots show that the size of the recirculation region changes slightly during a freestream cycle. The mean lift and drag coefficients are nearly the same as those obtained for the steady mean freestream flow. However, there is a phase shift between the aerodynamic forces and the freestream velocity which is mainly affected by the reduced frequency. Higher reduced frequencies and freestream amplitudes cause "wider" oscillations in the lift and drag forces, separation and reattachment locations. For the case with the highest frequency and the largest amplitude, the spanwise velocity fluctuations are much lower than those of the streamwise and normal velocities, while the fluctuation in the streamwise velocity is slightly more than that of the normal velocity.

For the flows with oscillating freestream AoA, higher reduced frequencies and AoA amplitudes cause wider oscillations in the lift and drag forces. The amplitude of the lift force is, however, about one order of magnitude larger than that of the drag force. Compared to the steady mean freestream flow, there is little change in the mean lift, while the mean drag is reduced due to Katzmayr effect. The size of the recirculation region changes significantly during a freestream cycle at low reduced frequencies and high AoA amplitudes. Higher reduced frequency decreases the amplitude of separation point oscillations, but higher AoA amplitude increases it. Significant oscillation in the surface friction occurs near the trailing edge at high reduced frequencies and AoA amplitudes, resulting from strong vortex shedding at the trailing edge. Compared to the steady mean freestream flow, the mean separation point moves downstream and the mean reattachment point moves upstream when the freestream velocity magnitude or AoA oscillates.

The wind gust simulation shows a rapid increase in the aerodynamic loads on the airfoil at the beginning of the gust. It is also shown that small fluctuations in the gust can cause significant fluctuations in the aerodynamic forces.

Copyright by
SHIWEI QIN
2012

ACKNOWLEDGEMENTS

I would like to thank my advisors Profs. Farhad Jaberi and Mei Zhuang for their endless support, advice and patience during my PhD studies. I greatly appreciate their faith in allowing me to work on this project, which has been very challenging and rewarding. I would also like to thank other members of my PhD committee, Profs. Alejandro Diaz, Zhengfang Zhou, and Manoochehr Koochesfahani. I am sincerely grateful for their very helpful suggestions.

Additionally, I like to thank very much the Air Force Research Laboratory at Wright-Patterson Air Force Base and Drs. Jack Benek and Miguel Visbal for supporting this project and for their valuable comments and suggestions. I also want to thank Marshall Galbraith for his assistance.

Finally, I would like to thank my friends and especially my family for their support during my PhD studies at Michigan State University. Special thanks to my wife, Yanming.

TABLE OF CONTENTS

LIST OF TABLES

LIST OF FIGURES

LIST OF SYMBOLS

Symbols

A, B	Assembly mass matrices
C	Acoustic speed in fluid, or Chord length
C_D	Drag coefficient
C_F	Skin friction coefficient
C_{ij}	Cross stress tensor
C_L	Lift coefficient
C_P	pressure coefficient
C_w	WALE model constant
D	Drag force per unit span of the airfoil
$D_1 - D_7$	Constants in wind gust model
G	Filter function
$G_1 - G_3$	Functions in wind gust model
I	Unit matrix
L	Lift force per unit span of the airfoil
M_a	Mach number
R_e	Reynolds number
R_{ij}	Reynolds stress tensor
S	Acoustic speed in the fluid
$\overline{S}_{ij}$	Filtered rate-of-strain tensor

S_{ij}^{d}	Tensor in WALE LES model
T	Period
T_R	Residence time
U	Freestream velocity in x direction
V	Freestream velocity in y direction, or Volume of a computational cell
W	Freestream velocity in z direction
V_0	Reference velocity
X_S	Separation location
X_R	Reattachment location
X_T	Transition location
f	Fluid body force (e.g. gravitation)
$\overline{g}_{ij}$	Filtered velocity gradient
i	Imaginary unit
k	Wavenumber or reduced frequency
n	Boundary surface normal
p	Pressure
s	axis tangent to the airfoil surface
t	Time
u, v, w	Velocity components in x, y, and z directions
v	Velocity vector
x, y, z	Cartesian coordinates
Δ	Filter width

∞	Infinity

Greek Symbols

Φ	Vector of eigenfunctions
$\|\Omega\|$	Vorticity Magnitude
α	Angle of attack
δ_{ij}	Kronecker symbol
κ	Von Karman constant
ν	Kinematic viscosity
ν_t	Turbulent viscosity
ρ	Density
ρ_0	Reference density
τ_{ij}	Subgrid-scale stress tensor
ω	Angular frequency or vorticity

Subscripts

f	Fluctuation quantities
i	Imaginary part of complex number
i, j, k	Coordinate index
m	Mean quantities
r	Real part of complex number
t	Turbulent quantities
*	Two-dimensional operator

Superscripts

$\bar{}$	Averaged or filtered quantities
^	Amplitude of disturbance quantities
'	Disturbance quantities or relative coordinate vector
",""	Second- and fourth-order derivatives

Operators

∇^2	Laplace Operator

1. Introduction

There has been a growing interest in small Unmanned Air Vehicles, including Micro Air Vehicles (MAVs), in recent years due to their growing capability to perform a wide range of missions. These vehicles typically operate at low to moderate Reynolds numbers in the order of 10^4 to 10^5 due to low speed and small vehicle size. At this range of Reynolds numbers, the flow near the airfoil leading edge is still laminar, and flow separation occurs at some point due to substantial adverse pressure gradients. At not very high Reynolds number and AoA, the flow can reattach to the airfoil. The flow streamlines show a laminar separation bubble (LSB) [1-3] bounded by the separation and reattachment points. Based on its size, a LSB can be categorized as either a small bubble or a large bubble. A small bubble covers a small portion of the airfoil surface and does not have a significant effect on the velocity and pressure distributions. A large bubble covers a considerable portion of the surface and significantly changes the pressure distribution and the velocity field. A separation bubble, especially a large one, decreases the lift and increases the drag, and consequently reduces the efficiency of the airfoil. The onset and successive breakdown of the LSB at low Reynolds number flows is known to be detrimental to the performance, endurance, and stability of MAVs.

To better understand the stability characteristics of the flow over a 2D wing at low Reynolds number, local and global stability methods are used in this study to analyze the flow instability over the SD7003 airfoil with a considerable LSB. Stability analysis is considered to be useful for better understanding of the instability of attached and separated flows [4]. Hammond and Redekopp [5] used a modeled separation bubble with the assumption of quasi-parallel flow and performed linear local stability analysis with a one-dimensional eigenvalue and Orr-Sommerfeld solver to determine the conditions for absolute instability of the flow over an airfoil

with LSB. Theofilis et al. [6], on the other hand, used non-parallel two-dimensional steady flows as base flows in their "BiGlobal" linear stability analyses. Since stability analysis is sensitive to the base flow, it is important that the base flow is carefully quantified. Thus, experimental measurements or "reliable" numerical simulations are necessary for doing an accurate stability analysis. In the current study, the base flow is computed by LES [7]. Results of local and global stability analyses are compared, and stability features of the flow over the SD7003 airfoil are discussed.

Many studies have been done on the characterization and control of LSB over symmetric and asymmetric airfoils. A commonly studied asymmetric airfoil for low-moderate Reynolds number flows is the SD7003 airfoil. Experimental study and measurements of flows around the SD7003 airfoil have been reported by a number of researchers using different facilities and methods. Radespiel et al [8] conducted experiments in a water channel and a low-noise wind tunnel at Technical University of Braunschweig (TU-BS) and obtained high resolution velocity and Reynolds stress data. Detailed particle image velocimetry (PIV) measurements were conducted by Ol et al. [9] at the Air Force Research Laboratory (AFRL) water channel. Measurements in a water channel using Molecular Tagging Velocimetry (MTV) were conducted by Katz et al. [10-13] at Turbulent Mixing and Unsteady Aerodynamics Laboratory (TMUAL) at Michigan State University. Numerical tools were also applied to simulate flows over the SD7003 airfoil. Reynolds-averaged Navier-Stokes (RANS) [14-17] and LES [7, 18-21] models were both employed to capture the flow dynamics and to predict the aerodynamic forces.

Unsteady aerodynamics of maneuvering airfoils has also been studied by experimental and numerical methods [22-24]. Both rigid and flexible airfoils were considered. The airfoil motions studied include pitching, plunging, or combination of the two. Bohl and Koochesfahani [22, 25]

reported measurements of the vortical field in the wake of a pitching airfoil. LES computation of flows past a plunging airfoil was reported by Visbal [23]. A comparison between measurement and computation of an airfoil in pitching and plunging motions was given by McGowan et al. [24]. Inviscid theory for this type of flows has a 75 years history and has provided valuable insight to many questions regarding unsteady flows over moving airfoils. For example, Theodorsen [26] presented the lift and pitching moment for a two-dimensional, flat-plate airfoil under harmonic pitching and plunging motions. Von Kármán and Sears [27] developed a general theory for unsteady aerodynamics of an airfoil in non-uniform motion. An excellent review of works in this area is given in reference [28].

Discrepancy of the measured mean separation and reattachment points in flows over the SD7003 airfoil, obtained from different facilities has been reported [9, 11, 29]. The main reason for these discrepancies is suggested to be the different levels of freestream turbulence in the experimental facilities. Experiments by Olson [12] confirmed that the increased freestream turbulence delays the separation and triggers earlier reattachment.

For MAVs typically flying at low speeds, freestream unsteadiness may cause significant changes in aerodynamic forces and thus possible flight instability. Some analytical works based on inviscid theory were developed by Isaacs [30] and Greenberg [31] for unsteady flows over airfoils. By extending the method of Theodorsen [26], they calculated the lift and moment of an airfoil at a fixed AoA in a freestream with harmonic velocity magnitude oscillation. Although different assumptions are applied to the wake, the predicted results by Isaacs and Greenberg are shown to be very similar. There are not many experimental studies on fixed airfoils operating in an unsteady freestream flow. This might be partly due to difficulty of controlling the flow in experiments. The frequency of freestream flow oscillation is limited by the fact that the

freestream uniformity across the test section becomes unacceptable even at relatively low frequencies [32]. Therefore, experiments of this type usually have very low reduced frequencies. To verify the Katzmayr effect [33], Toussaint et al. [34] used an array of pitching blades in front of the tested airfoil to create a freestream with oscillating flow direction. In this experiment, the maximum reduced frequency is less than 0.5, and freestream properties (e.g. level of turbulence) behind the oscillating blades were not given. Williams et al. [35] measured flows over a semi-circular wing in a wind tunnel that generates sinusoidal oscillations in the freestream velocity magnitude with reduced frequencies less than 0.7. They found that the measured lift force lags the freestream velocity by a noticeable amount even at low reduced frequencies, and the phase shift does not show a strong dependence on the mean AoA. The amplitude of oscillations in the lift coefficient was shown to be affected by both the AoA amplitude and the frequency of oscillations in freestream AoA. However, the measured amplitude and phase shift in lift coefficient differed significantly from predictions by Greenberg's theory. Using k-ω turbulence model and a 2D mesh, Gharali and Johnson [36] conducted unsteady RANS simulations of flows over fixed S809 airfoil with oscillating freestream velocity direction. In these simulations, the reduced frequency ranges from 0.026 to 18. The results for a case with a very low reduced frequency of 0.026 were compared to experimental results of a pitching airfoil with some level of agreement. Their study also showed that, at high reduced frequencies, the airfoil experiences oscillations in lift and drag coefficients with very large amplitude.

In this work, we study the details of the unsteady flow over the SD7003 airfoil by unsteady numerical simulations with the LES method. The simulated oscillation frequencies extend from a relatively low value to high values, well beyond the highest found in experiments conducted with freestream flow oscillations. This provides a better understanding of the unsteady flow physics

over two-dimensional airfoils. Three types of unsteady freestream flows are considered. In the first type, the freestream velocity direction and AoA are fixed, but the freestream velocity magnitude oscillates harmonically in time. Frequency and amplitude of the oscillation are varied (within a range possible in our simulation) to investigate the flow response to different levels of flow unsteadiness. In the second type of unsteady flows considered in this study, the freestream velocity magnitude is fixed but the freestream velocity direction or AoA is changed harmonically in time. Again, the flow direction is changed over a range of frequencies and amplitudes. Effects of these two types of freestream flow oscillations on the aerodynamic forces, vorticity field, velocity fluctuations, boundary layer separation and reattachment are studied. The computed lift coefficients are compared to those predicted by the inviscid theory. Finally in the third unsteady flow type considered in this study, a wind gust model is used for studying the flow over the airfoil exposed to more realistic "wind type" flow conditions.

The SD7003 airfoil is used in all analyses presented in this dissertation. Figure 1 shows a schematic 2D view of this airfoil, which has a maximum thickness and camber of 8.5% and 1.48% of the chord length, respectively. This airfoil is chosen because of the availability of experimental and computational data.

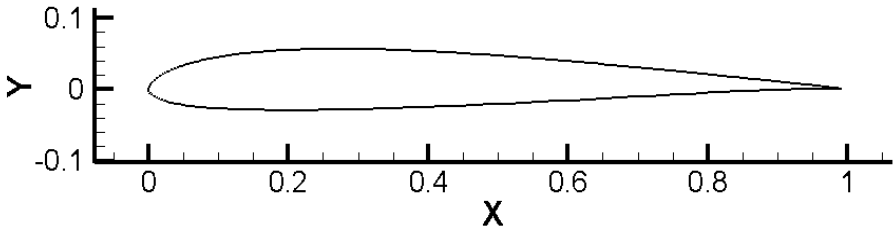

Figure 1: The SD7003 airfoil.

2. Linear Stability Analysis

2.1 Global Stability Formulation

The global stability analysis conducted here is based on the numerical solutions of a three-dimensional partial-derivative eigenvalue problem, which describes small-amplitude three-dimensional disturbances developing on a two-dimensional steady or time-averaged base flow around the airfoil. The base flow is assumed to be the same in the spanwise direction (denoted by z) such that $\partial/\partial z=0$ for the base flow. Following Ding and Kawahara [37], slight compressibility is assumed so that the singularity in the spectrum of the eigenproblem is avoided. The singularity arises from the continuity constraint of incompressible flow as explained by Malkus [38]. The nondimensional scales for length, velocity, time, density, and kinematic pressure are taken to be C, U_0, C/U_0, ρ_0, and SU_0, where S is the sound speed in the fluid. The dimensionless form of the continuity equation is

$$\frac{D\rho}{Dt}+\rho\nabla\cdot\mathbf{V}=0, \tag{1}$$

where $\frac{D}{Dt}=\frac{\partial}{\partial t}+(\mathbf{V}\cdot\nabla)$ is the substantial derivative. With the assumption of small compressibility, the kinematic pressure p (which is the pressure divided by density) is a function of density as [37],

$$\frac{Dp}{Dt}=\frac{1}{\rho M_a}\frac{D\rho}{Dt} \tag{2}$$

where $M_a=U_0/S$ is the Mach number of the flow. By substituting Equation (2) into Equation (1), a modified continuity equation is obtained

$$\frac{Dp}{Dt}+\frac{1}{M_a}\nabla\cdot\mathbf{V}=0\,. \tag{3}$$

Under small compressibility conditions, considering the kinematic viscosity ν of the fluid to be constant and f to be a constant body force (e.g. gravitational force), the nondimensional momentum equation can be written as

$$\frac{D\mathbf{v}}{Dt}=-\frac{1}{M_a}\nabla p+\frac{1}{R_e}\left[\nabla^2\mathbf{v}+\frac{1}{3}\nabla\left(\nabla\cdot\mathbf{v}\right)\right]+f\,, \tag{4}$$

where $Re=U_0\,C/\nu$ is the Reynolds number.

2.1.1 Base flow

For global stability analysis, the airfoil is assumed to be infinitely long in the spanwise direction, so that the base flow becomes two-dimensional and steady. Compressibility is neglected in computing the base flow. Therefore, the base flow equations become

$$\nabla\cdot\bar{\mathbf{V}}=0 \tag{5}$$

$$\left(\bar{\mathbf{V}}\cdot\nabla_*\right)\bar{\mathbf{V}}=-\nabla_*\bar{P}+\frac{1}{R_e}\nabla_*^2\bar{\mathbf{V}}\,, \tag{6}$$

where $\bar{\mathbf{V}}$ and $\bar{P}$ are the velocity and kinematic pressure in the base flow, respectively. ∇_* represents the two-dimensional gradient operator.

2.1.2 Perturbation equations

A flow variable may be decomposed into a steady base flow and an unsteady perturbation. The perturbed flow variables may be described in the following form

$$\mathbf{v}\left(x,y,z,t\right)=\bar{\mathbf{V}}(x,y)+\mathbf{v}'\left(x,y,z,t\right) \tag{7}$$

$$p\left(x,y,z,t\right)=\bar{P}(x,y)+p'\left(x,y,z,t\right). \tag{8}$$

The perturbations u', v', w', p' are assumed to be inhomogeneous in x and y, have a harmonic dependence on the spanwise coordinate z, and grow exponentially in time as,

$$p' = i\hat{p}(x,y)e^{ikz+\omega t}, \tag{9}$$

$$u' = i\hat{u}(x,y)e^{ikz+\omega t}, \tag{10}$$

$$v' = i\hat{v}(x,y)e^{ikz+\omega t}, \tag{11}$$

$$w' = \hat{w}(x,y)e^{ikz+\omega t}. \tag{12}$$

In Equations (9) to (12), i is the imaginary number, $k = 2\pi C/L_z$ is the nondimensional spanwise wavenumber where L_z is the spanwise wavelength, and $\omega = \omega_r + i\omega_i$ denotes the complex growth rate. The reason for using the imaginary amplitude in the normal modes is to avoid complex arithmetic in the calculation of eigenproblem [37].

Substituting Equations (7) and (8) into the continuity Equation (3) and the momentum Equation (4), subtracting the base flow Equations (5) and (6), neglecting the high order terms of perturbations and replacing the perturbed variables with Equations (9) to (12) result in the following eigenproblem for perturbations with the growth rate as the eigenvalue and perturbation amplitudes $\hat{u}, \hat{v}, \hat{w}, \hat{p}$ as the eigenfunctions.

$$\omega\hat{u} + (\bar{\mathbf{V}}\cdot\nabla_*)\hat{u} + (\hat{\mathbf{v}}\cdot\nabla_*)\bar{U} + M_a{}^{-1}\frac{\partial\hat{p}}{\partial x} = R_e{}^{-1}\left[\left(\nabla_*^2 - k^2\right)\hat{u} + \frac{1}{3}\frac{\partial}{\partial x}\left(\nabla_*\cdot\hat{\mathbf{v}} + k\hat{w}\right)\right] \tag{13}$$

$$\omega\hat{v} + (\bar{\mathbf{V}}\cdot\nabla_*)\hat{v} + (\hat{\mathbf{v}}\cdot\nabla_*)\bar{V} + M_a{}^{-1}\frac{\partial\hat{p}}{\partial y} = R_e{}^{-1}\left[\left(\nabla_*^2 - k^2\right)\hat{v} + \frac{1}{3}\frac{\partial}{\partial y}\left(\nabla_*\cdot\hat{\mathbf{v}} + k\hat{w}\right)\right] \tag{14}$$

$$\omega\hat{w} + (\bar{\mathbf{V}}\cdot\nabla_*)\hat{w} - M_a{}^{-1}k\hat{p} = R_e{}^{-1}\left[\left(\nabla_*^2 - k^2\right)\hat{w} - \frac{1}{3}k\left(\nabla_*\cdot\hat{\mathbf{v}} + k\hat{w}\right)\right] \tag{15}$$

$$\omega\hat{p} + (\bar{\mathbf{V}}\cdot\nabla_*)\hat{p} + (\hat{\mathbf{v}}\cdot\nabla_*)\bar{P} + M_a{}^{-1}\left(\nabla_*\cdot\hat{\mathbf{v}} + k\hat{w}\right) = 0 \tag{16}$$

For the stability analysis of the separated flow, the following boundary conditions are implemented: all disturbance velocity components are zero on the solid wall and in the freestream. On the solid wall, the compatibility conditions (Equations (17) and (18) below) are derived from the equations for the pressure perturbation. In Equation (17), $\mathbf{I}^*$ is the two-dimensional identity matrix. All disturbances at the inflow boundary are zero, which, from a physical point of view, serves to ensure that no perturbations other than those due to potentially self-excited global eigenmodes enter the separated flow region. Linear extrapolation from the interior of the domain is applied for obtaining the disturbances on the outflow boundary.

$$\left(-\frac{1}{M_a}\hat{p}\mathbf{I}^* + \frac{1}{R_e}\left(\nabla\hat{\mathbf{v}} + \frac{1}{3}\mathbf{I}^*\left(\nabla_* \cdot \hat{\mathbf{v}} + k\hat{w} \right) \right) \right) \cdot \mathbf{n} = 0 \tag{17}$$

$$\nabla\hat{w} \cdot \mathbf{n} = 0 \tag{18}$$

Finite element method is used to discretize Equations (13)-(16). With this method, the imposition of the boundary conditions results in a real non-symmetric generalized eigenvalue problem in the form of

$$\mathbf{A\Phi} = \omega\mathbf{B\Phi}, \tag{19}$$

where **A** and **B** are the assembly mass matrices calculated from the base flow and $\Phi = \{\hat{u}, \hat{v}, \hat{w}, \hat{p}\}$ is the assembly vector of the eigenfunctions. Details on how **A** and **B** are computed are presented in APPENDIX A. According to linear stability theory, the stability properties of the flow depend on the eigenvalue ω. When ω is real, the disturbances either grow or decay monotonically and the critical Reynolds number is one for which $\omega = 0$. When ω is complex, the neutral condition is $\omega_r = 0$, and the onset of instability is oscillatory with dimensionless angular frequency ω_i. This normal mode form also includes the time-dependent two-dimensional instability of the steady flow for which $k = 0$.

With eigenmodes obtained from stability computation, the total three-dimensional flow field can be reconstructed on the basis of the two-dimensional base flow with an arbitrary number of disturbance eigenmodes. When these eigenmodes are chosen to be conjugate pairs of most unstable modes of an eigenspectrum, the three-dimensional flows can be expressed by the following superposition of eigenfunctions (the pressure and y-velocity v have a similar form as that of u)

$$u = \bar{U} - 2\sum_{n=1}^{N} e^{t\omega_r^n} \cos(kz)\left[\hat{u}_i^n \cos\left(t\omega_i^n\right) + \hat{u}_r^n \sin\left(t\omega_i^n\right)\right] \tag{20}$$

$$w = 2\sum_{n=1}^{N} e^{t\omega_r^n} \cos(kz)\left[\hat{w}_r^n \cos\left(t\omega_i^n\right) - \hat{w}_i^n \sin\left(t\omega_i^n\right)\right] \tag{21}$$

where subscripts r , i , n , N denotes the real and imaginary parts of the eigenfunctions, the n_{th} pair of eigenmodes and the total number of conjugate pairs of eigenmodes, respectively.

2.2 Local Stability Formulation

As the first validation step of global stability analysis, local stability analysis is carried out for the same base flow, and its results are compared to those of global stability analysis. The base flow closely satisfies $\partial/\partial x << \partial/\partial y$ at all locations, therefore it is reasonable to assume that in a short streamwise distance, the flow over airfoil is a parallel flow, which justifies the application of local stability analysis to local x-velocity profiles $\bar{U}$ at different streamwise locations.

For a parallel viscous flow $\bar{U}(y)$, with perturbations assumed to be in form of Equation (22) below, the temporal local stability variables are governed by the Orr-Sommerfeld Equation (23). For simplification, the viscosity is neglected and the Orr-Sommerfeld equation is reduced to the Rayleigh equation (24) [39] with boundary conditions described in Equation (25).

$$(u', v', w', p') = \left[\hat{u}(y), \hat{v}(y), \hat{w}(y), \hat{p}(y)\right] \exp(ikx + \omega t) \tag{22}$$

$$\left(\bar{U} - i\frac{\omega}{k}\right)\left(\hat{v}'' - k^2\hat{v}\right) - \bar{U}''\hat{v} + \frac{i\nu}{k}\left(\hat{v}'''' - 2k^2\hat{v}'' + k^4\hat{v}\right) = 0 \tag{23}$$

$$\hat{v}'' - \left(k^2 + \frac{\bar{U}''}{\bar{U} - i\,\omega/k}\right)\hat{v} = 0 \tag{24}$$

$$\hat{v}(0) = 0 \quad \text{and} \quad \hat{v}(y \to \infty) = e^{-k\,y} \tag{25}$$

A smoothing-spline method is developed in this study to enable exact fitting of any base flow profile obtained from experiments or computations with smooth first- and second-order derivatives. Simple analytical expressions of the velocity profiles were used by others [40-42] to perform local stability analysis. However, it is not practical to find simple analytical profiles for all experimental or simulation data. Inaccurate representation of the base flow could cause significant error in the stability analysis. The smoothing-spline method gives a nearly perfect fitting and is used in the current study. This fitting method is implemented in the eigensolver developed in this study. A shooting method [43] is used in the eigensolver to solve the Rayleigh equation.

2.3 Base Flow Results

The base flow used in the present work is the same as that obtained by Galbraith et al. [7] with high-order implicit large eddy simulation (LES) method. The airfoil flow has a Reynolds number of 60,000 and an AoA of 4°. The computational domain (shown in Figure 2 as an enclosed rectangle) for the global stability analysis covers the domain in the range of X/C $\in$ (0.1941, 1.0156) and Y/C $\in$ (0.0011, 0.2914), which ensures that the whole LSB is enclosed for

the global stability analysis. For local stability analysis, x-velocity profiles at different streamwise locations in the same base flow are used.

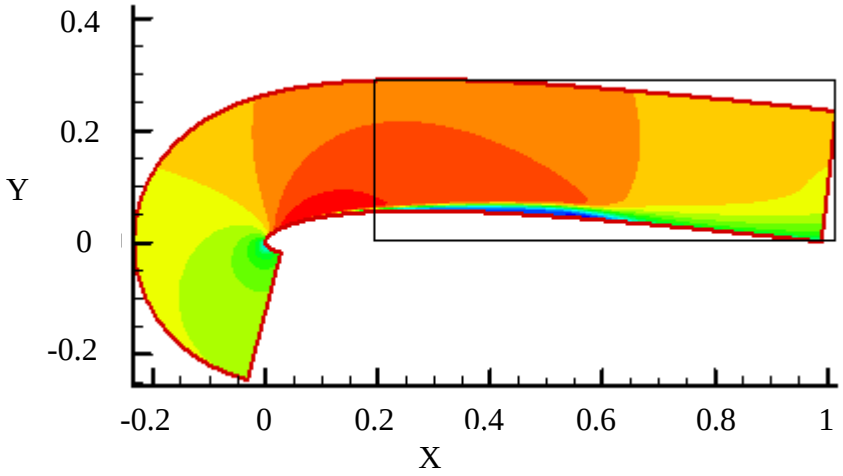

Figure 2: Base flow around a SD7003 airfoil, Re=60,000, α=4° [7]. Contours represent time-averaged x-velocity. The rectangular solid line shows the domain used in the global stability analysis (For interpretation of the references to color in this and all other figures, the reader is referred to the electronic version of this dissertation).

2.4 Local Stability Results

To obtain the most unstable modes, local stability analysis is applied to a series of x-velocity profiles at different streamwise locations with an increment of 0.05C. The most unstable mode is found to occur with the velocity profile at x/C=0.5 shown in Figure 3. The Rayleigh Equation (24) is solved with boundary condition described in Equation (25) for the eigenmodes. Details of the numerical solution procedure can be found in reference [42]. The most unstable mode of is calculated to be $\omega=17.94+41.48i$ (Figure 4), corresponding to a most unstable nondimensional frequency (normalized by C/U_0) of 6.6.

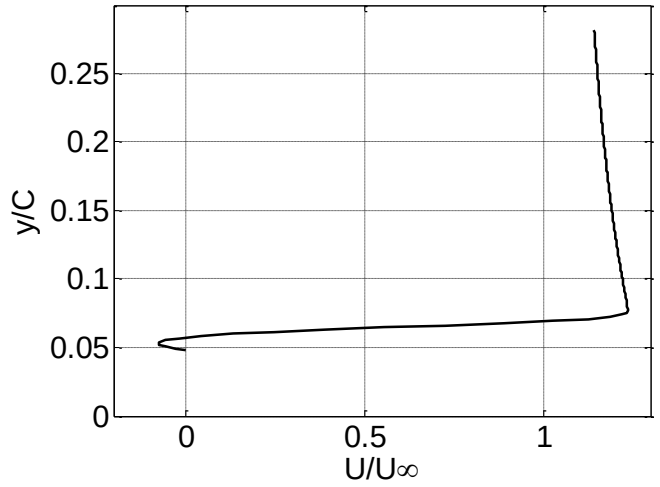

Figure 3: Time-averaged x-velocity (U) profile at x/C=0.5.

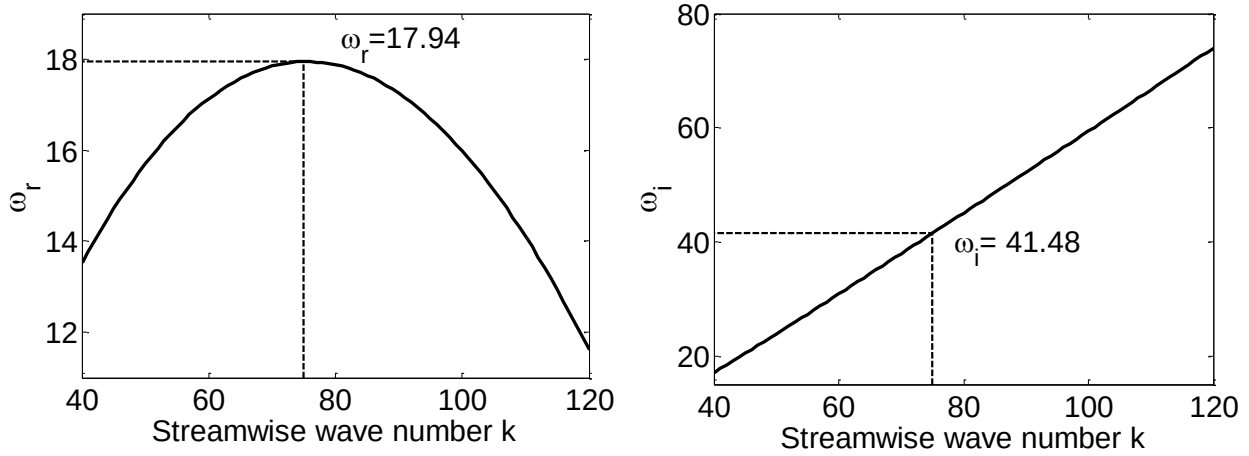

Figure 4: Local stability analysis results for time-averaged x-velocity (U) profile at x/C=0.5; (left) growth rate vs. wavenumber, (right) angular frequency vs. wavenumber.

2.5 Global Stability Results

A computational model/code is developed based on the formulation in Section 2.1. To validate our code, a series of computations on the global stability of the lid-driven cavity flow are performed with the same equations, different base flows and boundary conditions. The results are found to be in agreement with those obtained by Ding and Kawahara [37] and Theofilis [44].

The effect of grid resolution on the solution is tested by considering six different meshes with the following resolutions: 29×21, 41×30, 47×35, 56×41, 70×51, and 76×80 (Figure 5). The largest difference between the results obtained by meshes 70×51 and 76×80 is about 3%, which indicates that the effect of mesh resolution is relatively small for the 70×51 mesh. This non-uniform mesh is used for global stability analysis.

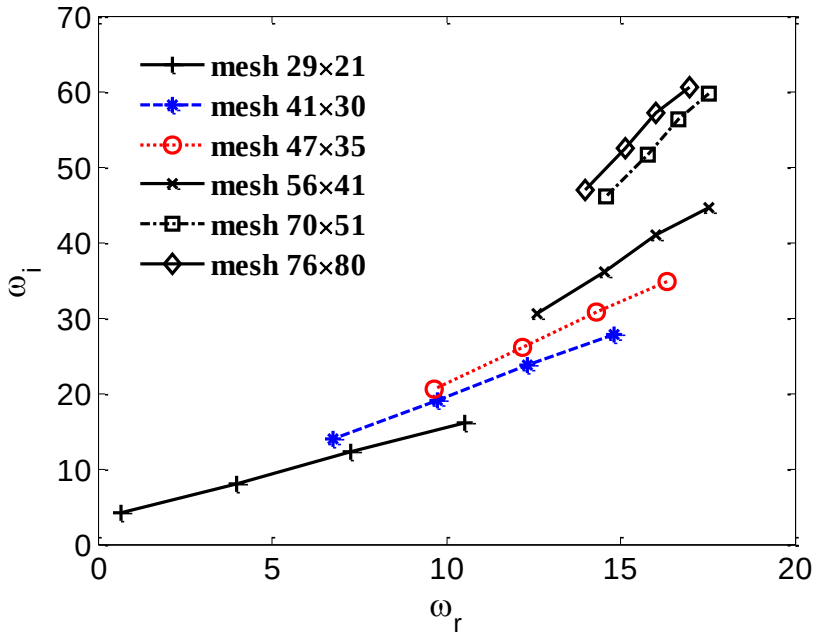

Figure 5: The four most unstable modes at wavenumber k=20, obtained with different base flow grids.

For each wavenumber k, the most unstable mode is sought. A wide range of wavenumber values (0.2, 90) is considered. It should be noted that the upper limit of k is relatively high due to the fact that the airfoil chord is used as the length scale in our analysis ($k = 2\pi C/L_z$). If a smaller length scale is used, the wavenumbers will be proportionally reduced. This wavenumber range corresponds to a range of wavelength normalized by the airfoil chord L_z/C (0.070, 31.4). The relation between the most unstable eigenvalue, the one with the largest real part, and the wavenumber is shown in Figure 6. It is shown that the growth rate decreases as wavenumber

increases. In Equations (13) to (15), the terms $-k^2$ and ω are on opposite sides. Therefore, for k larger than 90, the growth rate of the most unstable mode is expected to decrease further. Since the real part of the growth rate of the most unstable mode is positive for all k values, the flow is unstable. Moreover, the angular frequency increases as the wavenumber increases, indicating that the shorter wavelength perturbations are less unstable. With wavenumber k being close to zero, the most unstable mode reaches a plateau of $\omega=18+59.4i$ at which the angular frequency 59.4 corresponds to a nondimensional frequency of 9.5. The maximum growth rates from the global and local analyses are roughly in agreement, and both methods predict an unstable flow. However, the most unstable frequency from the global analysis is higher than that predicted by the local analysis. This difference is caused by the combined effect of using local velocity profiles and neglecting viscosity in the local stability analysis. Galbraith et al. [7] monitored in their simulation the time variation of velocity at a point directly above the airfoil surface at x/C=0.5, and plotted the turbulent kinetic energy spectrum at that point (Figure 7). They pointed out that the nondimensional frequency of 9 may be the most unstable frequency of the flow even though it is not the dominant frequency observed in the velocity energy spectrum. Their later stability analysis [20] also yields a most unstable frequency close to 9.

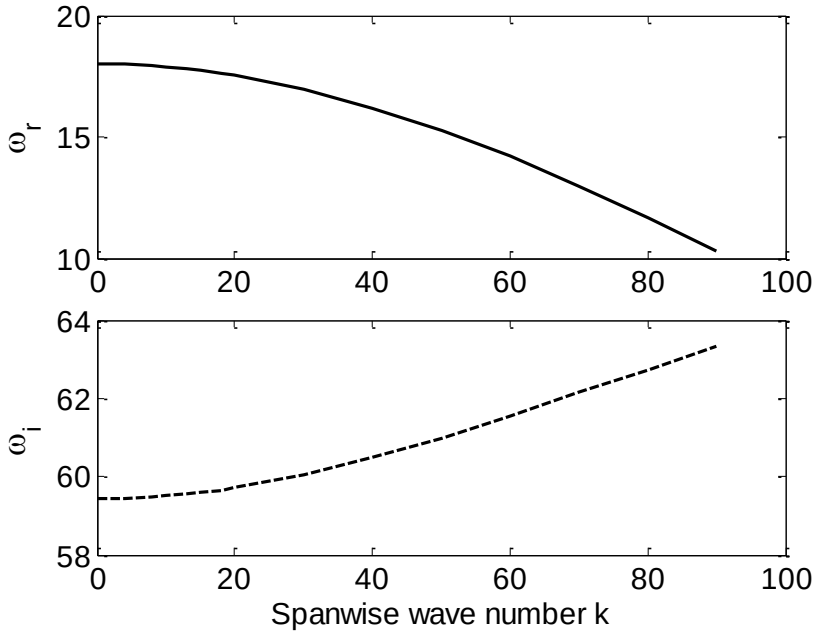

Figure 6: The most unstable modes vs. wavenumber; (upper) maximum growth rate, (lower) angular frequency.

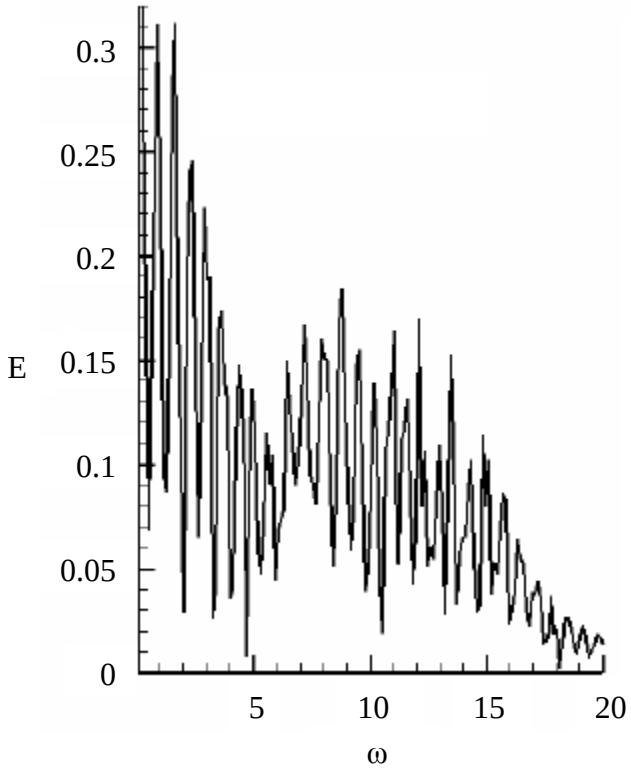

Figure 7: Turbulent-kinetic-energy frequency spectra at x/C=0.5 (about center of LSB) [7].

According to Equations (20) and (21), the three-dimensional velocity field can be reconstructed by adding the summation of a number of eigenmodes to the base flow. Since linear instability is assumed, reconstructed velocities do not necessarily resemble the real flow. But the emphasis here is on the distribution of velocity disturbances and their relation. Figure 8 shows the reconstructed x-velocity given by Equation (20) for k=1, obtained with the conjugate pair of the most unstable eigenmodes. The eigenvalue for the most unstable mode is $\omega=18+59.4i$ with a nondimensional period of T=0.1058. Figures 8 shows the velocity at times 0, T/4, T/2, and 3T/4. Since the growth rate of the most unstable mode is greater than zero, the stability analysis predicts that the disturbances will amplify in time and become dominant over the base flow. The increasing range of the color bar in Figure 8 confirms this. Figure 9 shows the reconstructed disturbances (without the base flow velocity) of the three velocity components at T/2 obtained with the same eigenmodes. Evidently, the three velocity disturbances share some similar features. First, the disturbances are zero at inlet, at airfoil surface and at far-field boundaries, as enforced by the boundary conditions. It should be noted that disturbances are also zero at the outlet, which is not restricted by the boundary condition. Second, all disturbances are confined to the region $0.2<x/C<0.65$ and $y/C<0.2$, which corresponds to the LSB region where reverse flow occurs in the base flow. The maximum magnitude and maximum gradient of disturbances occur around $x/C=0.4$. It is found that the z-velocity disturbance is much smaller in magnitude than the disturbances of x- and y-velocities. Similar differences in disturbances were also found in the stability analysis of lid-driven cavity flow by Ding and Kawahara [37]. For wavenumbers other than 1, the qualitative structure of the velocity disturbances, calculated based on the pair of the most unstable eigenmodes, is similar to that shown in Figure 9. Therefore, the above remarks are valid at different wavenumber values.

The spanwise eigenmodes indicate the existence of oscillatory flow structure perpendicular to the base flow plane. This can be verified by the instantaneous z-velocity contours shown in Figure 10 at a z-section plane which are obtained from the 3D LES data of a fully developed flow.

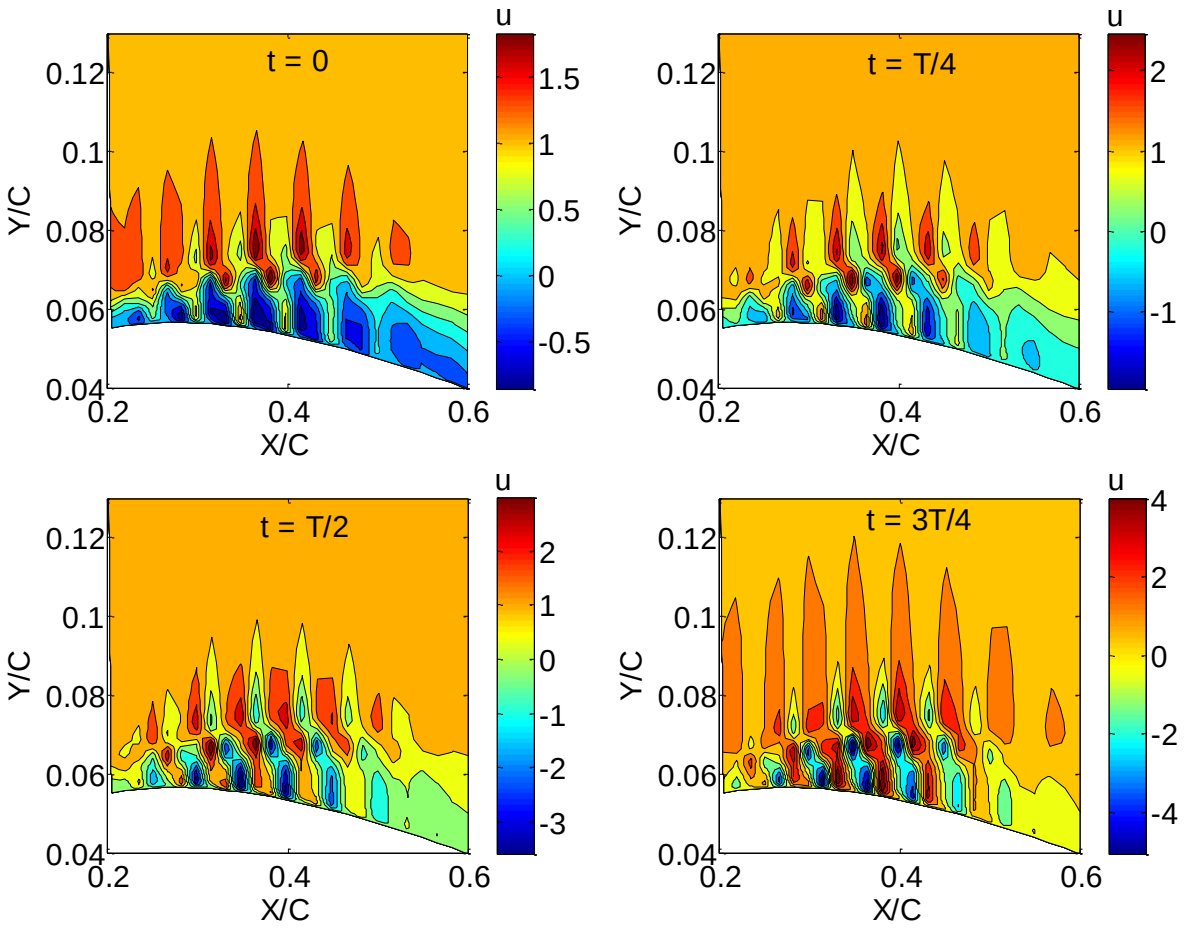

Figure 8: Reconstructed total x-velocity using the conjugate pair of most unstable modes for k=1; (a) t=0, (b) t=T/4, (c) t=T/2, (d) t=3T/4.

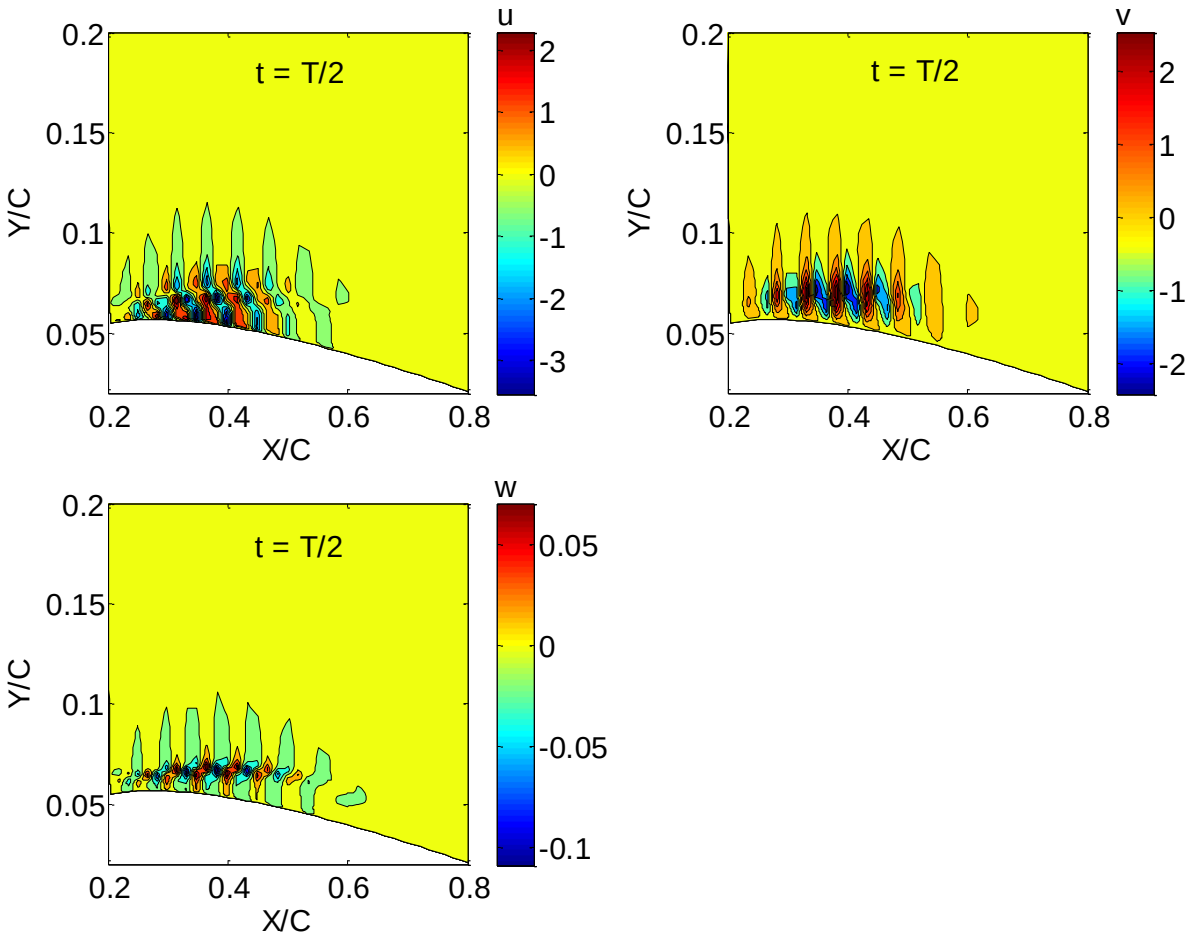

Figure 9: Reconstructed velocity disturbances using the conjugate pair of most unstable modes for k=1 at t=T/2.

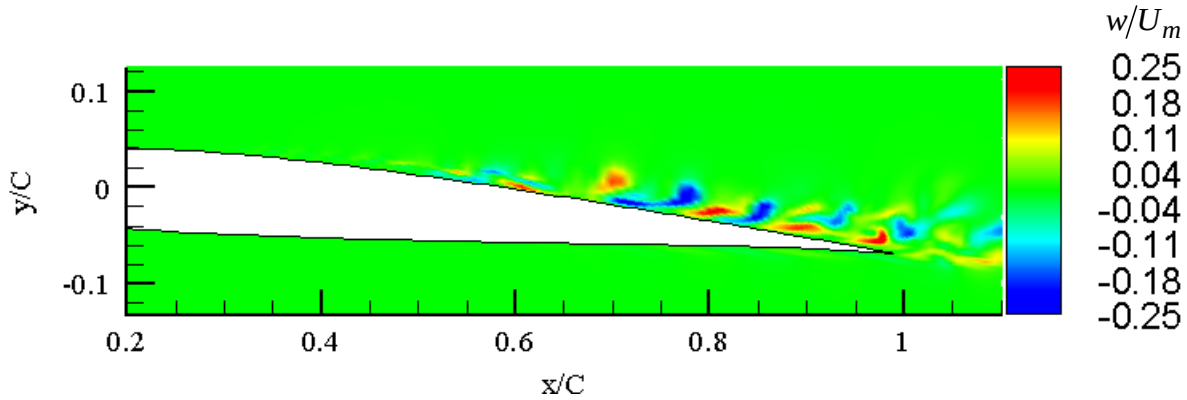

Figure 10: Instantaneous normalized z-velocity w/U_m on a z-section, α=4°, Re=60,000.

3. Simulation Method

3.1 Background

In addition to stability analysis discussed in the previous chapter, detailed simulations of steady and unsteady flows over SD7003 airfoil are conducted with the large eddy simulation (LES) method. Reynolds-averaged Navier-Stokes (RANS) models are much computationally less demanding than LES but they can only predict the ensemble- or time-averaged behavior of the flow. Furthermore, RANS solutions greatly depend on empirical model constants and often fail to capture some of the key features of the flow such as flow separation and reattachment. In LES, large eddies of the flow are explicitly computed by solving the "filtered" Navier-Stocks equations, while smaller eddies are modeled using a subgrid-scale (SGS) model. The rationale behind LES is that by modeling less, the error caused by the modeling of turbulence can be reduced. It is also believed to be easier and more accurate to model small scales, since they are more isotropic and less affected by the boundary conditions. Although LES usually requires substantially more computational resources than RANS, it is computationally less demanding than direct numerical simulation (DNS) method, and hence can be applied to relatively high Reynolds number flows.

The governing equations for LES are obtained by filtering the time-dependent Navier-Stokes equations. The filtering process effectively removes eddies with sizes smaller than the filter width or grid spacing used in the computation. In some of LES calculations such as those conducted by the FLUENT code [45], the filtering is implicit, which means that the filtered equations do not explicitly show the information on the filter shape or width. The information is implicitly contained in the SGS model and the discretization of the equations.

3.2 Filtered Equations

In any LES method, the resolved or filtered value of variable ϕ is computed as

$$\bar{\phi}(\mathbf{x}) = \int_D \phi(\mathbf{x}') G(\mathbf{x}, \mathbf{x}') d\mathbf{x}' , \tag{26}$$

where D is the flow domain, and G is the filter function which satisfies the normalization function $\int_D G(\mathbf{x}, \mathbf{x}') d\mathbf{x}' = 1$. There are a variety of filter functions such as Gaussian filter, Fourier cut-off filter, or box filter [46] available for LES. In the adopted code, the finite-volume discretization itself implicitly provides the box filtering operation as

$$\bar{\phi}(\mathbf{x}) = \frac{1}{V} \int_V \phi(\mathbf{x}') d\mathbf{x}' , \tag{27}$$

where V is the volume of a computational cell. The implied box filter function is over the physical space, and it has the following form

$$G(x, x') = \begin{cases} 1/V, & x' \in v \\ 0, & otherwise \end{cases} . \tag{28}$$

The filtered continuity and momentum equations for an incompressible and Newtonian fluid take the following form [47]:

$$\frac{\partial \bar{u}_i}{\partial x_i} = 0 \tag{29}$$

$$\frac{\partial \bar{u}_i}{\partial t} + \frac{\partial \left(\bar{u}_i \bar{u}_j \right)}{\partial x_j} = -\frac{1}{\rho} \frac{\partial \bar{p}}{\partial x_i} + \frac{\partial}{\partial x_j} \left(\nu \frac{\partial \bar{u}_i}{\partial x_j} \right) - \frac{\partial \tau_{ij}}{\partial x_j} \tag{30}$$

where

$$\tau_{ij} \equiv \overline{u_i u_j} - \bar{u}_i \bar{u}_j \tag{31}$$

is the unclosed subgrid-scale (SGS) stress tensor.

Often, the SGS turbulence models used for τ_{ij} are based on Boussinesq hypothesis [48] and are expressed by the following equation

$$\tau_{ij} - \frac{1}{3}\delta_{ij}\tau_{kk} = -2\nu_t \bar{S}_{ij} \quad , \tag{32}$$

where ν_t is the subgrid-scale eddy viscosity and $\bar{S}_{ij}$ is the resolved-scale strain rate tensor,

$$\bar{S}_{ij} \equiv \frac{1}{2}\left(\frac{\partial \bar{u}_i}{\partial x_j} + \frac{\partial \bar{u}_j}{\partial x_i} \right) \tag{33}$$

With a model for ν_t, Equation (30) is closed and may be solved for the resolved variables.

3.3 Subgrid-Scale Model

The subgrid-scale model used in this study is the Wall-Adapting Local Eddy-viscosity (WALE) model of Nicoud et al. [49]. Compared to dynamic Smagorinsky and Kinetic Energy Transport SGS models, WALE model is relatively simple yet sufficiently accurate for the flows considered in this study. The model is based on the square of the velocity gradient tensor. The eddy viscosity is obtained from the following equation

$$\nu_t = \left(C_w \Delta\right)^2 \frac{\left(S_{ij}^d S_{ij}^d\right)^{3/2}}{\left(\bar{S}_{ij}\bar{S}_{ij}\right)^{5/2} + \left(S_{ij}^d S_{ij}^d\right)^{5/4}} \quad , \tag{34}$$

where S_{ij}^d is defined as

$$S_{ij}^d = \frac{1}{2}\left(\bar{g}_{ij}^2 + \bar{g}_{ji}^2\right) - \frac{1}{3}\delta_{ij}\bar{g}_{kk}^2 \, , \tag{35}$$

$$\bar{g}_{ij} = \frac{\partial \bar{u}_i}{\partial x_j} \tag{36}$$

In Equation (34), Δ is the filter width computed as the cubic root of the computational cell volume, and C_w is the WALE model constant. A C_w value of 0.325 has been found to yield satisfactory results for a wide range of flows [45].

The WALE SGS model is a mixed model based on local rate of strain and rotational tensors, thus, suitable for prediction of the SGS kinetic energy dissipation. The eddy-viscosity goes naturally to zero in the model in the vicinity of the wall, and the model is able to return the correct wall asymptotic (y^3) behavior for wall bounded flows; therefore no dynamic procedure is required. Additionally, the WALE model generates zero eddy viscosity in laminar flows, while reproducing laminar to turbulent transition through the growth of linear instability modes. Guleren [50] tested several SGS models and concluded that WALE model performs generally better than other tested SGS models.

A comparison between WALE and other SGS models is made in Figure 11, where the mean surface pressure coefficient over SD7003 airfoil as computed with different SGS models are compared with the LES results generated by Galbraith et al. [7], whose results are in good agreement with the experiment. Figure 11 shows that the WALE model yields a very good agreement. Based on these findings, all simulations considered below are conducted with the WALE SGS model.

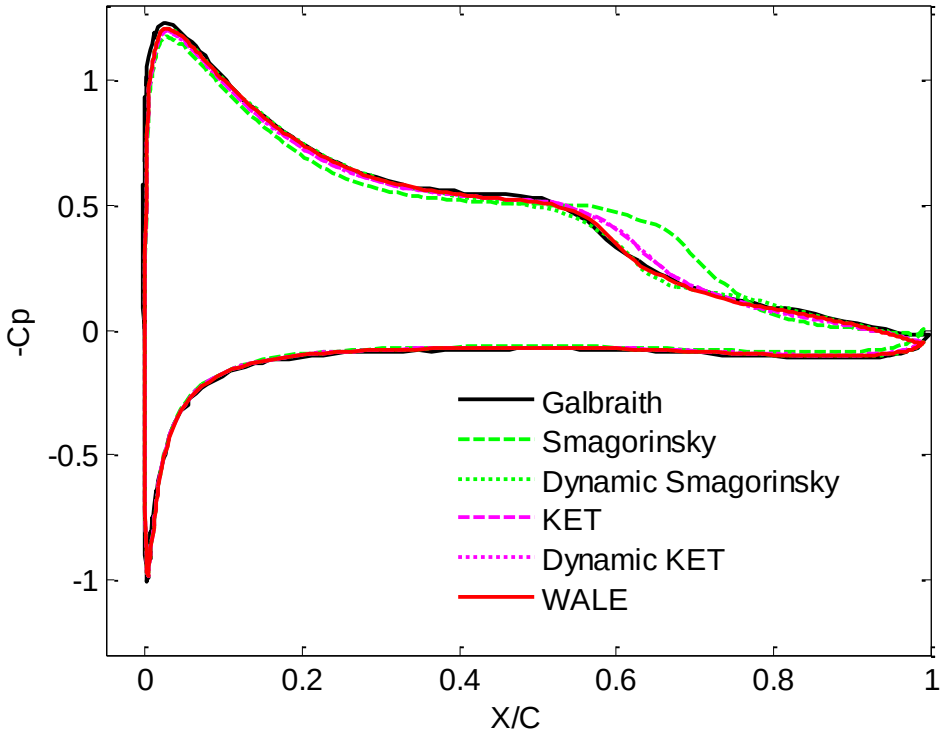

Figure 11: Comparison of time- and spanwise-averaged pressure coefficient over the SD7003 airfoil, obtained by our LES with different SGS models and compared with those obtained by Galbraith et al. [7]. The flow Reynolds number based on freestream velocity and airfoil chord is 60,000, and AoA=4 °. KET stands for Kinetic Energy Transportation model.

3.4 Grid and Boundary Conditions

Initially, a structured 2D O-grid (Figure 12a) of size 315×151 is generated for the SD7003 airfoil with a rounded trailing edge (Figure 12c). To generate accurate solution, the mesh is made to be highly orthogonal and is stretched rapidly from the surface of the airfoil outward (about 70% of the grid points are within a chord distance away from the airfoil center) to ensure high resolution of the flow near the airfoil (Figure 12c). The far field boundary is made to be almost a circle with the center at the chord mid-point and a radius of about 27 chords. The 2D mesh is copied in the spanwise (z) direction to form a 3D grid. The 3D grid has 101 nodes in the spanwise direction, and thus the total grid size is 315×151×101. The grids are evenly spaced in

the spanwise direction with a spanwise extent of 0.2C. The grid is similar to that used by Galbraith [20].

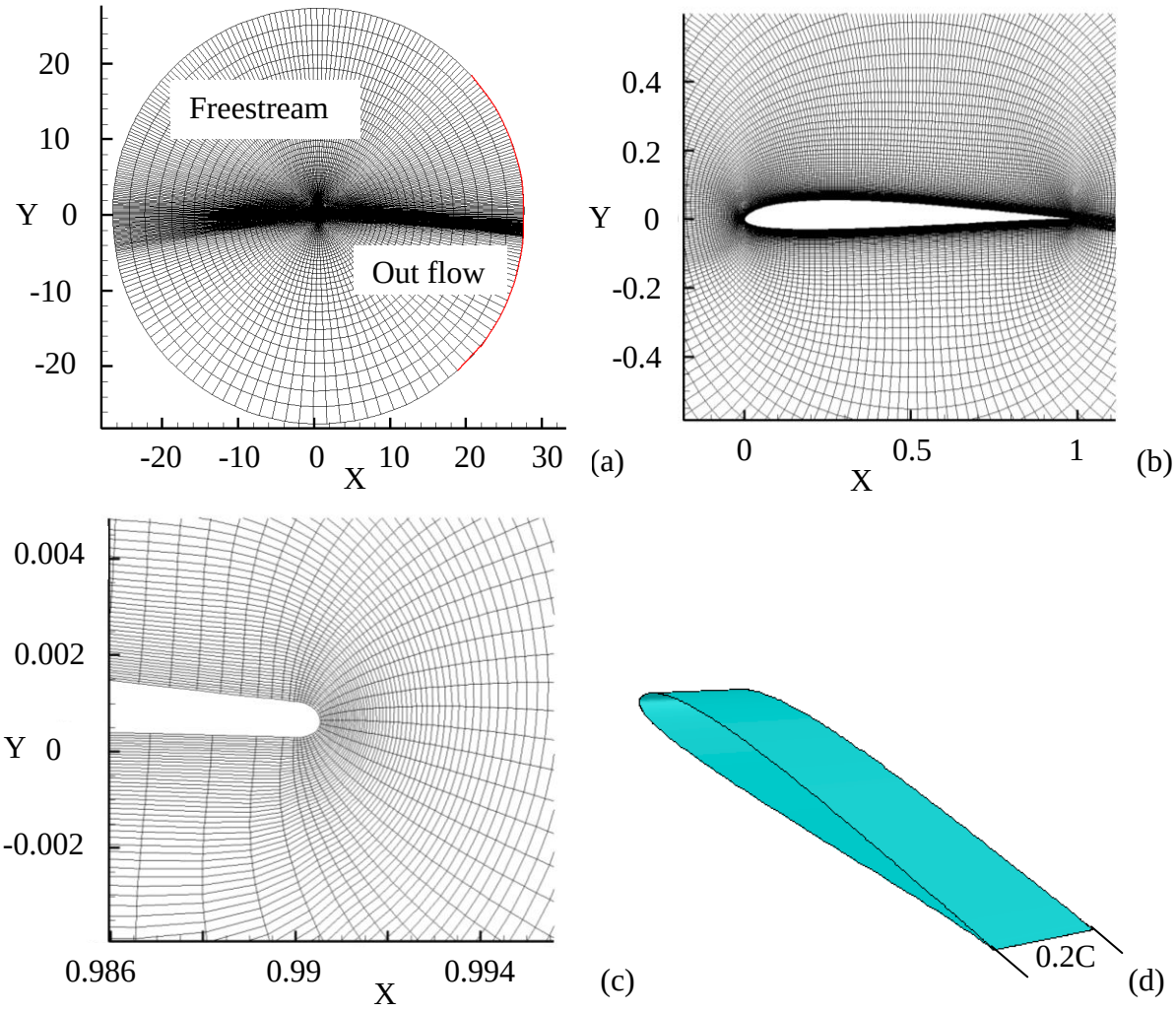

Figure 12: Computational grid: (a) grid on XY plane, (b) grid in the vicinity of airfoil, (c) grid near the trailing edge, (d) 3D airfoil.

Solutions for the steady flow over SD7003 airfoil were obtained using the 3D 315×151×101 grid and three other coarser and finer grids [20]. It was found that the 315×151×101 grid captures the flow features well and generates results that closely match those obtained based on substantially finer grids, even though the substantially finer grids provide slightly better details

of the flow in the transition region. The $315 \times 151 \times 101$ grid provides an adequate flow resolution for the quantities reported here and is used in this study.

Boundary conditions are specified in the following manner. On most of the far-field boundary, freestream velocity conditions with no perturbations are prescribed with steady or unsteady flow conditions for velocity and pressure. For wake region of the outer boundary, we use the outflow boundary condition in which variables on the boundary are extrapolated from the interior of the computational domain. The airfoil surface is modeled with a no-slip adiabatic wall boundary condition. A spanwise periodic boundary condition is imposed on the side faces, which, equivalently, requires the two side faces to be frictionless and have the same flow properties (e.g. velocity and pressure).

In all simulations considered in this study, sufficient time is given to the flow to become fully developed before any data are recorded or analyzed. A flow with steady freestream is considered fully developed when lift and drag forces become stabilized and their moving averages over two residence times show no change in time. For a flow with periodic freestream to be considered fully developed, the monitored lift and drag forces are required to become periodic and their peak values become steady. In order to reduce the computational time associated with initial development of the 3D flow, a fully developed 2D flow is generated first, and the 2D data is then transferred to the 3D mesh and used as the initial condition. The non-dimensional time step $\Delta t U_\infty / C$ is kept constant at 1.37×10^{-4} which is sufficiently small for resolving the temporal variations in the flow.

The momentum equations are discretized using a second-order bounded central difference scheme, and the continuity equation is discretized using a second-order central scheme. With very fine mesh near the airfoil surface, implicit time integration is chosen over explicit methods

in order to avoid very small time steps. The transient terms are discretized using second-order implicit scheme.

3.5 Separation, Transition, Reattachment, and Force Coefficients

The mean separation and reattachment points are where the mean skin friction coefficient changes signs. To define the transition point we follow the approach described in reference [8]. Laminar to turbulent transition is assumed to occur where the normalized Reynolds shear stress reaches 0.1% of the free steam velocity and grows significantly after that [8].

For flows with steady freestream, the x-direction is defined as the steady freestream direction, and the y-direction is perpendicular to the x-direction, as shown in Figure 13. The lift force is defined as the total force on the airfoil in the y-direction, and the drag force is defined as the total force on the airfoil in the x-direction. The lift and drag coefficients are defined as $C_L = L/(\rho U_\infty^2 C/2)$ and $C_D = D/(\rho U_\infty^2 C/2)$ where L is the total lift force per unit span length, D is the total drag force per unit span length, and U_∞ is the freestream velocity. The pressure coefficient C_P is calculated as $C_P = (p - p_\infty)/(\rho U_\infty^2/2)$, where p_∞ is the freestream pressure. The skin friction coefficient C_F is calculated as $C_F = \mu \frac{\partial u}{\partial \mathbf{n}} \Big/ (\rho U_\infty^2/2)$.

For flows with harmonically oscillating freestream velocity magnitude or direction, the x-direction is defined as the mean freestream direction, and the y-direction is perpendicular to the x-direction. The lift and drag forces are also obtained by decomposing the total aerodynamic force along the x-direction. The same definition of lift and drag for flows with oscillating freestream velocity direction was used by other researchers [34, 36]. For flows with a steady freestream and an oscillating airfoil (not considered in this study), it is not uncommon to decompose the drag and lift along the freestream direction even though the effective AoA is

constantly changing due to the airfoil oscillation [23, 54]. Thus, C_L, C_D, C_P, and C_F are defined the same as for flows with steady freestream, except that U_∞ is now changed to U_m, the mean freestream velocity magnitude. Unlike flows with steady freestream where pressure gradient is zero, flows with unsteady freestream have time-dependent pressure gradient related to the freestream velocity acceleration in either velocity magnitude or direction. Therefore for flows with unsteady freestream, the reference pressure p_∞ in the C_P definition is chosen to be the pressure at the point (0, 25C, 0.1C), on the y-axis and 25 chords away from the airfoil leading edge.

All C_L, C_D, C_P, and C_F calculated in our study are based on either both time- and spanwise-averaged data or just spanwise-averaged data. Figure 13 shows a schematic view of the flow directions for both steady and unsteady flows.

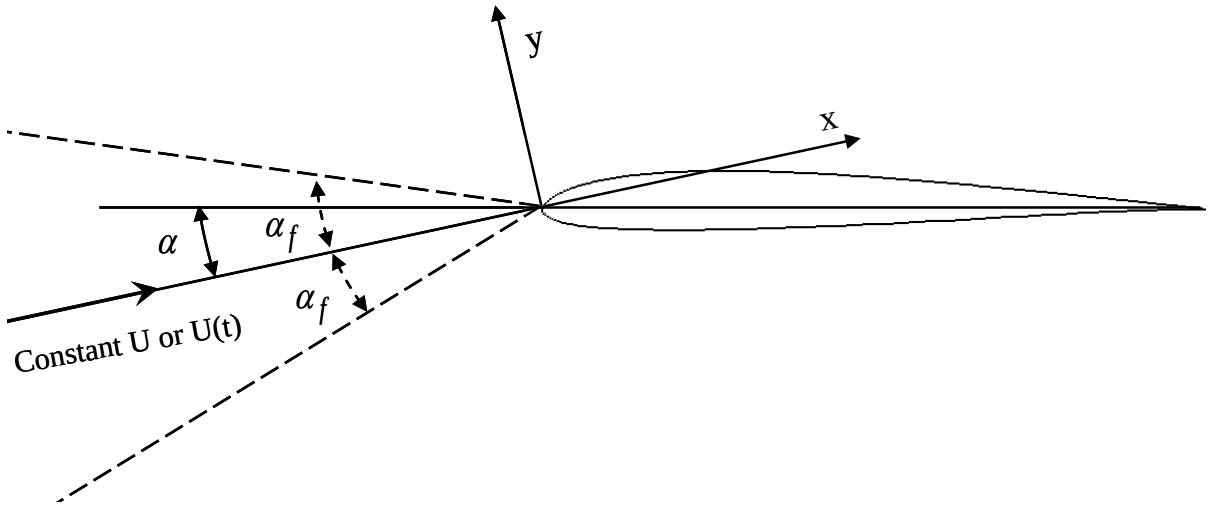

Figure 13: Schematic of flow over airfoil, showing the freestream and the coordinate system.

3.6 Comparison of 2D and 3D Simulations

The effect of flow three-dimensionality flow on the aerodynamic forces, the separation and reattachment of the boundary layer, and the flow structure is discussed in this section before considering the 3D steady and unsteady LES results in detail. For the flow with steady freestream, Re=60,000 and AoA=4°, 2D and 3D solutions are compared in Table 1 and Figures 14-16. Table 1 shows that the aerodynamic forces obtained from 2D solution are similar to that of 3D solution, though 2D simulation predicts a slightly longer LSB. Surface pressure coefficient obtained from the 2D solution also agrees reasonably well with the 3D solution. However, the separation occurs earlier in 2D simulation and the reattachment point is predicted by the 2D model to further downstream than that predicted by the 3D model. Also, the skin friction coefficient from the 2D solution does not increase to the same level as that of the 3D solution downstream of the reattachment point. The maximum difference in friction coefficient between 2D and 3D solutions is 5.8% of the total variation of C_F and it occurs at X/C=0.67. Figure 16 shows that the difference observed in the spanwise-averaged instantaneous 2D and 3D z-vorticity contours is significant. In the 2D solution, the separated boundary layer develops into a series of large-scale connected vortices which do not breakdown to smaller structures, consistent with the observations made by Galbraith [20] and Hodge et al. [51]. The 2D and 3D results for larger angle of attack of AoA=8° (but same Reynolds number) in Table 2 and Figures 17-18 show trends similar to those for flows with AoA=4°, even though the differences are more noticeable at higher angle of attack.

Date Set	Separation X_s/C	Transition X_t/C	Reattachment X_r/C	Lift coeff. C_L	Drag Coeff. C_D
LES, 2D	0.23	0.44	0.67	0.55	0.021
LES, 3D	0.25	0.50	0.64	0.59	0.020

Table 1: Mean quantities obtained from 2D and 3D solutions for the flow with steady freestream and Re=60,000 and AoA=4 °.

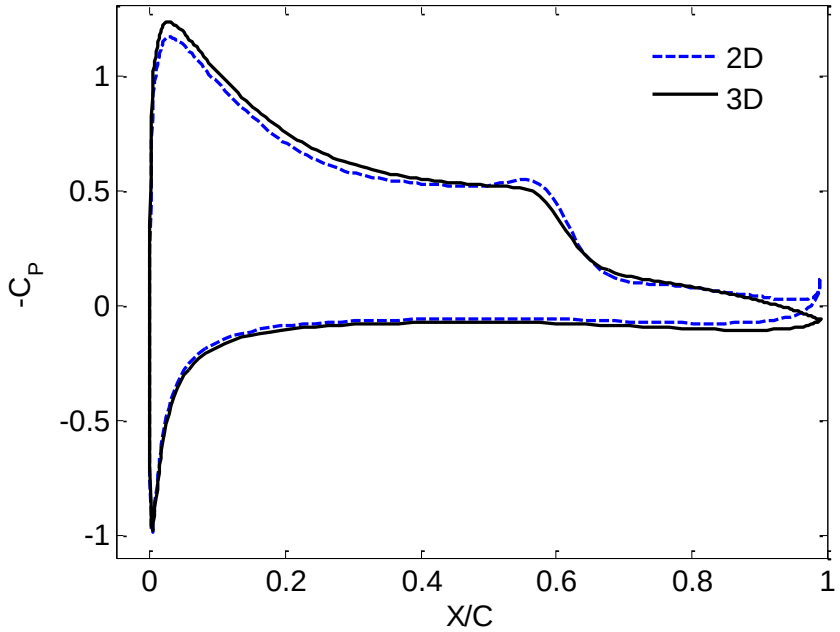

Figure 14: Time-averaged surface pressure coefficient obtained by 2D and 3D simulations of the flow with steady freestream and Re=60,000 and AoA=4 °.

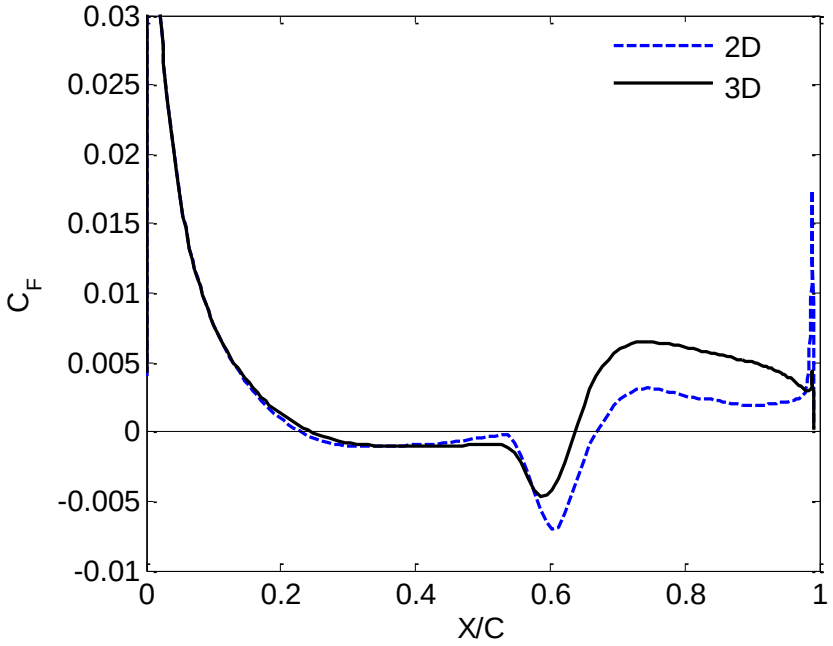

Figure 15: Time-averaged skin friction coefficient on the upper surface of the airfoil obtained by 2D and 3D simulations of the flow with steady freestream and Re=60,000 and AoA=4 °.

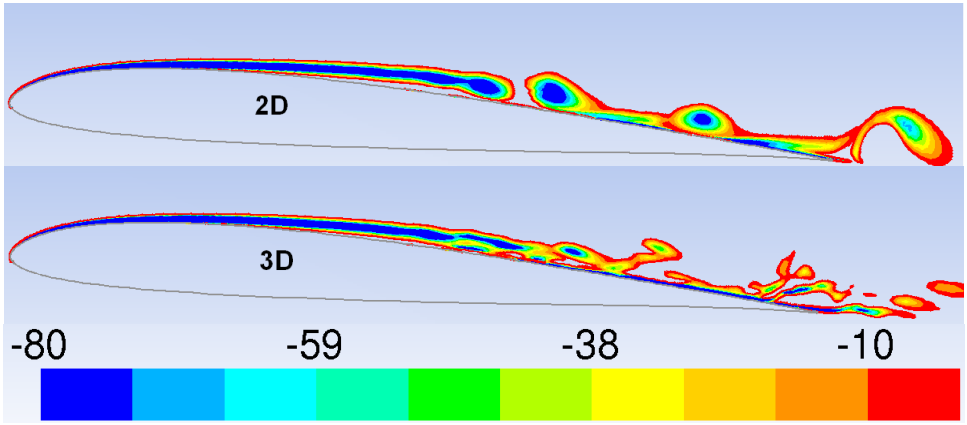

Figure 16: Instantaneous normalized z-vorticity ($\omega_z C/U_m$) contours obtained by 2D and 3D simulations of the flow with steady freestream and Re=60,000 and AoA=4 °.

Date Set	Separation X_s/C	Transition X_t/C	Reattachment X_r/C	Lift coeff. C_L	Drag Coeff. C_D
LES, 2D	0.037	0.15	0.29	0.91	0.042
LES, 3D	0.042	0.16	0.25	0.93	0.040

Table 2: Mean quantities obtained from 2D and 3D solutions for the flow with steady freestream and Re=60,000 and AoA=8 °.

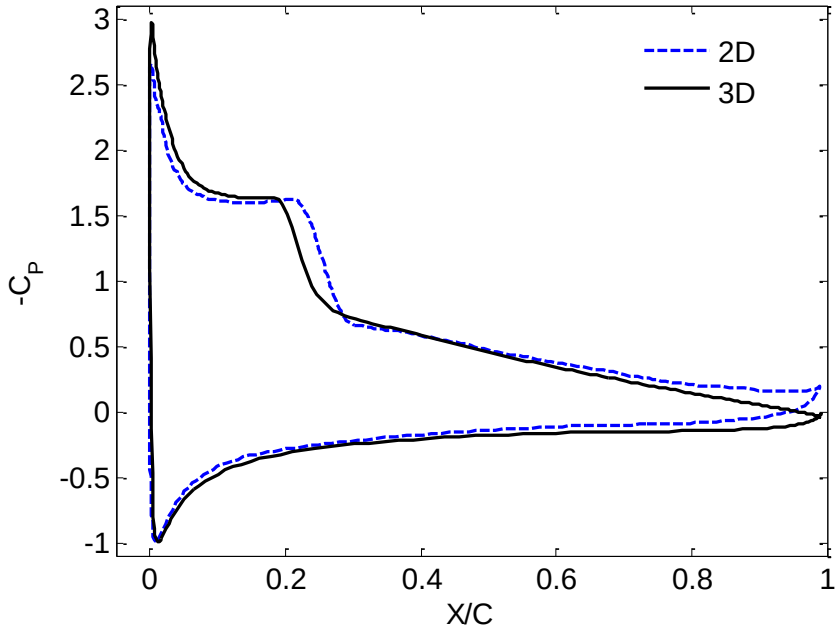

Figure 17: Time-averaged surface pressure coefficient obtained by 2D and 3D simulations of the flow with steady freestream and Re=60,000 and AoA=8 °.

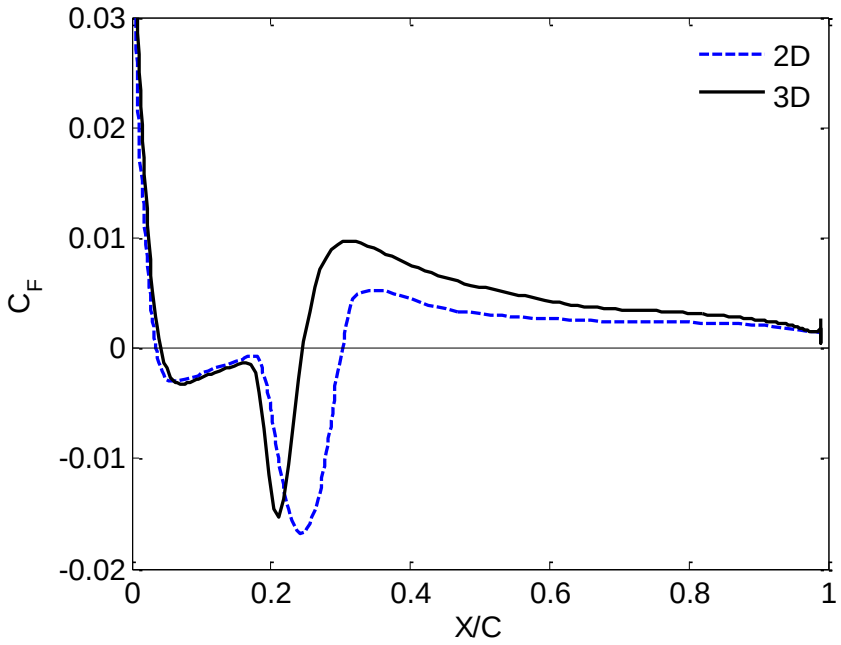

Figure 18: Time-averaged skin friction coefficient on the upper surface of the airfoil obtained by 2D and 3D simulations of the flow with steady freestream and Re=60,000 and AoA=8°.

The differences between 2D and 3D solutions are further examined for unsteady freestream flows over the airfoil. Comparison is made among three cases with oscillating freestream AoA. In each case, the velocity direction or AoA varies sinusoidally in the x-y plane as $\alpha(t) = 4^\circ + 8^\circ \times \sin(2\pi U_m t/C)$ where U_m is the constant freestream velocity magnitude. The z-velocity component is zero at freestream. The Reynolds number is calculated as $\mathrm{Re} = \rho U_m C/\mu$, and it is 10,000, 30,000 and 60,000 for the three cases simulated, respectively. The 2D and 3D values of C_L, C_D and z-vorticity iso-surfaces obtained by LES are compared in Figures 19-24. As explained in Section 3.5, C_L and C_D are calculated by normalizing the aerodynamic forces with U_m. In the z-vorticity iso-surface figures 20, 22, and 24, t0 is the beginning of a cycle when the AoA is at its mean value and increasing. When showing the vorticity iso-surfaces for the 2D solutions, the 2D domain is extended in the spanwise direction to the same spanwise size as the

3D domain for easier comparison. For all three Reynolds numbers, 2D and 3D solutions provide similar C_L and C_D profiles except in the peaks and valleys. In the 2D profiles, the peaks and valleys are somewhat "chopped off", and the amount "chopped off" increases slightly at higher Reynolds numbers. This is directly related to the difference in static pressure between 2D and 3D solutions. For the airfoil flows studied here, static pressure contributes vast majority of the lift (or drag).

For the unsteady case with oscillating AoA and Re=60,000, the pressure coefficient C_P on the airfoil surface at different times of a cycle is plotted in Figure 25. It can be seen that at times t0 and t0+T/2 when there is a significant acceleration in freestream AoA, the C_P curves of the 2D solution are narrower than those of the 3D solution, which causes the "chop-off" in the 2D C_L and C_D curves. There is no significant difference in the overall shape of C_P curves obtained from 2D and 3D solutions at times t0+T/4 and t0+3T/4. This indicates that lack of spanwise instability in the 2D simulations prevents the pressure in the separation region from reaching the same low and high values as in the 3D simulations at times of fast changing freestream AoA. This difference between 2D and 3D solutions also happens at relatively low Reynolds number of 10,000, which indicates that the spanwise instability has a significant effect on pressure even in laminar flows.

The z-vorticity iso-surfaces obtained from 3D simulations clearly show that the flow changes from laminar to turbulent as Reynolds number increases, while 2D solutions fail to capture this trend. At lower Re=10,000, the 2D and 3D solutions show very similar flow structures that are laminar and similar in spanwise direction. At higher Re=30,000, the 3D simulation shows spanwise fluctuation, and breakdown of vortices near the trailing edge while a large portion of the flow over the airfoil remains laminar. As Reynolds number further increases

to 60,000, the 3D simulation shows that the large-scale vortices break down earlier. At both Reynolds numbers of 30,000 and 60,000, the 2D simulations predict the flows to be laminar. As Reynolds number increases, the flow structures predicted by 2D and 3D simulations become less similar; at Re=30,000, the similarity is still noticeable, but it is much less so at Re=60,000.

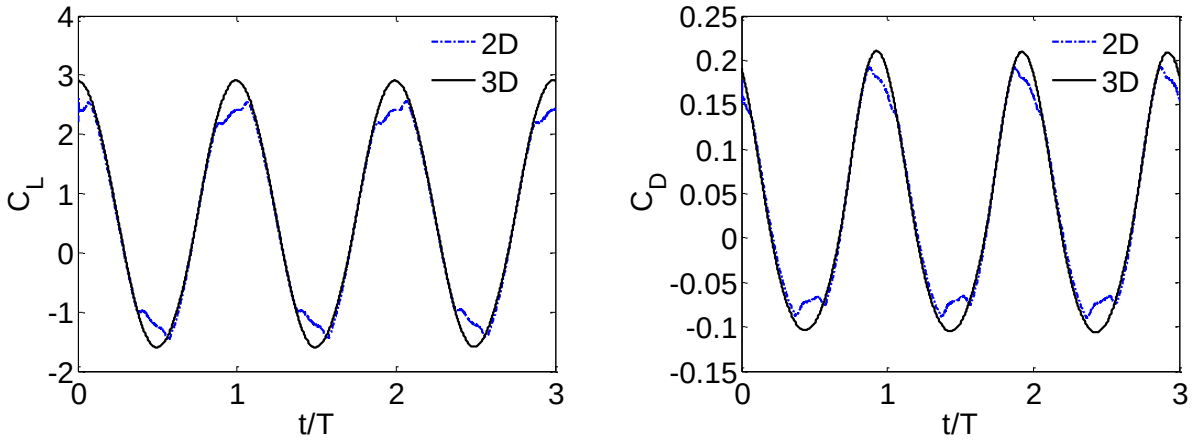

Figure 19: Lift and drag coefficients obtained by 2D and 3D simulations of the flow with oscillating AoA and Re=10,000.

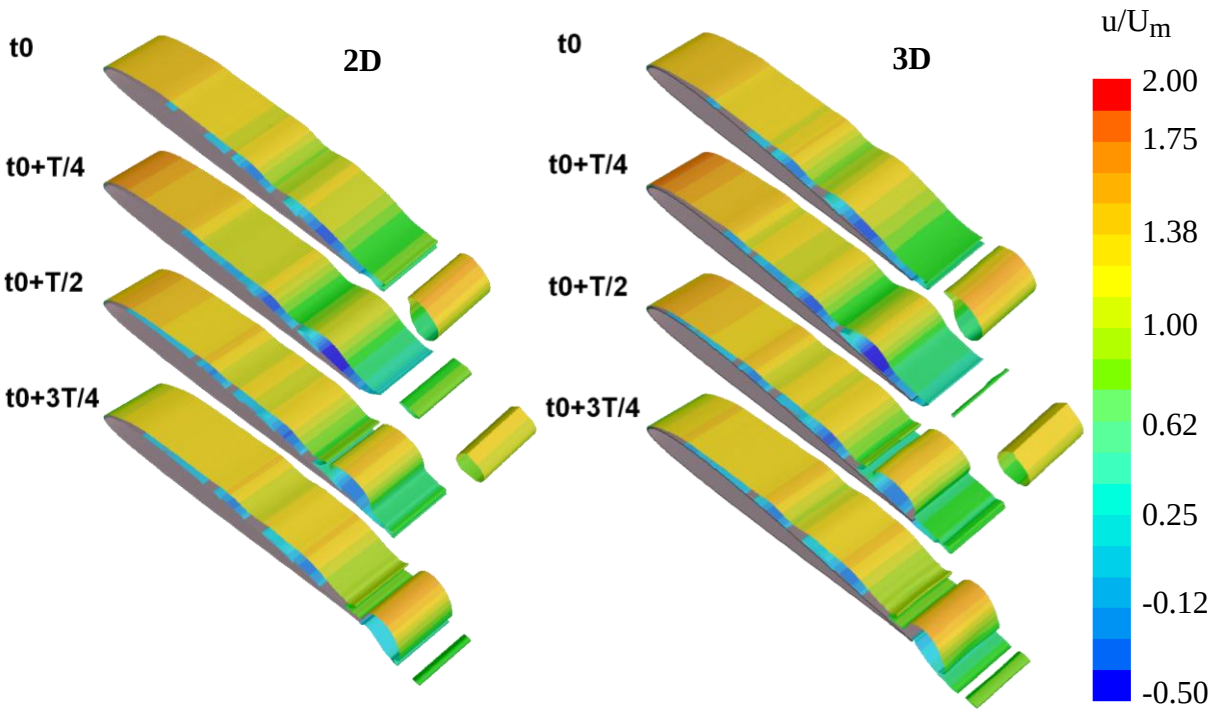

Figure 20: Iso-surfaces of z-vorticity ($\omega_z C/U_m = -10$) obtained by 2D and 3D simulations of the flow with oscillating AoA and Re=10,000 (colored by u/U$_m$ for better visibility).

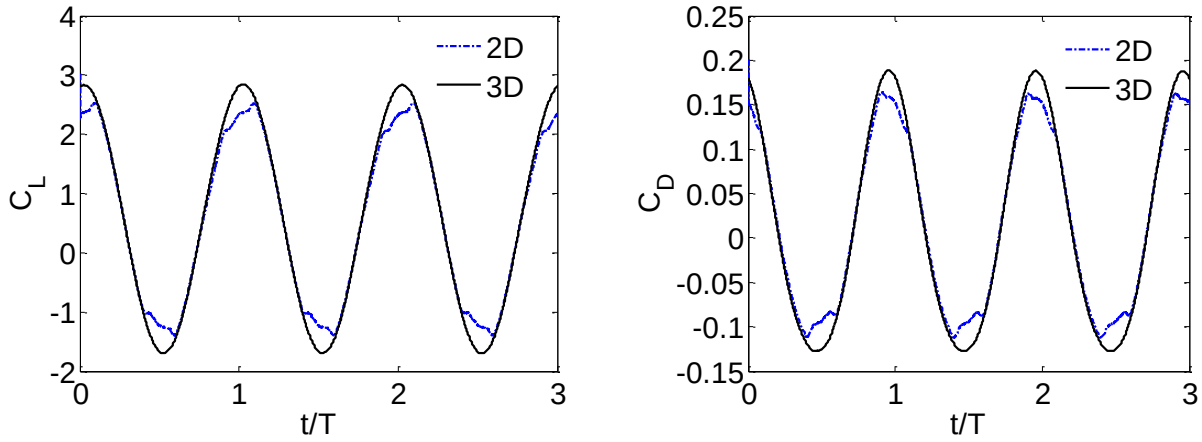

Figure 21: Lift and drag coefficients obtained by 2D and 3D simulations of the flow with oscillating AoA and Re=30,000.

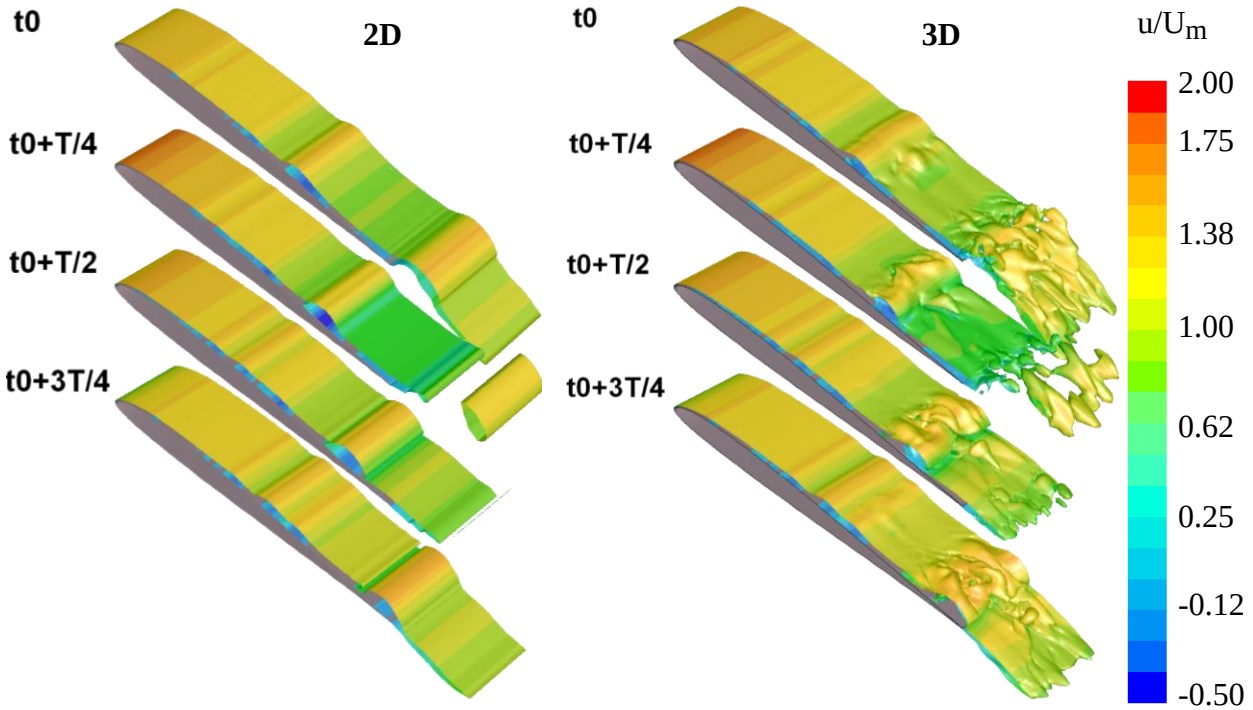

Figure 22: Iso-surfaces of z-vorticity ($\omega_z C/U_m = -10$) obtained by 2D and 3D simulations of the flow with oscillating AoA and Re=30,000.

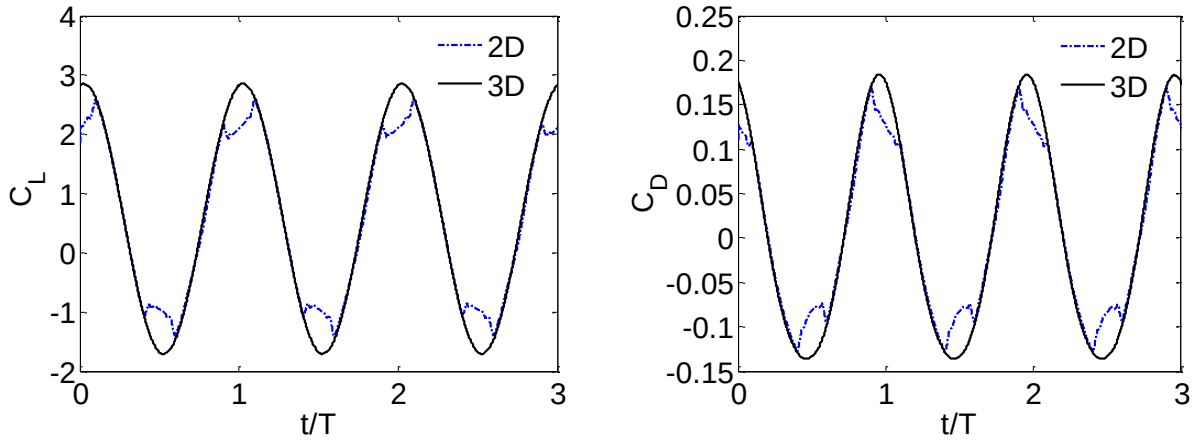

Figure 23: Lift and drag coefficients obtained by 2D and 3D simulations of the flow with oscillating AoA and Re=60,000.

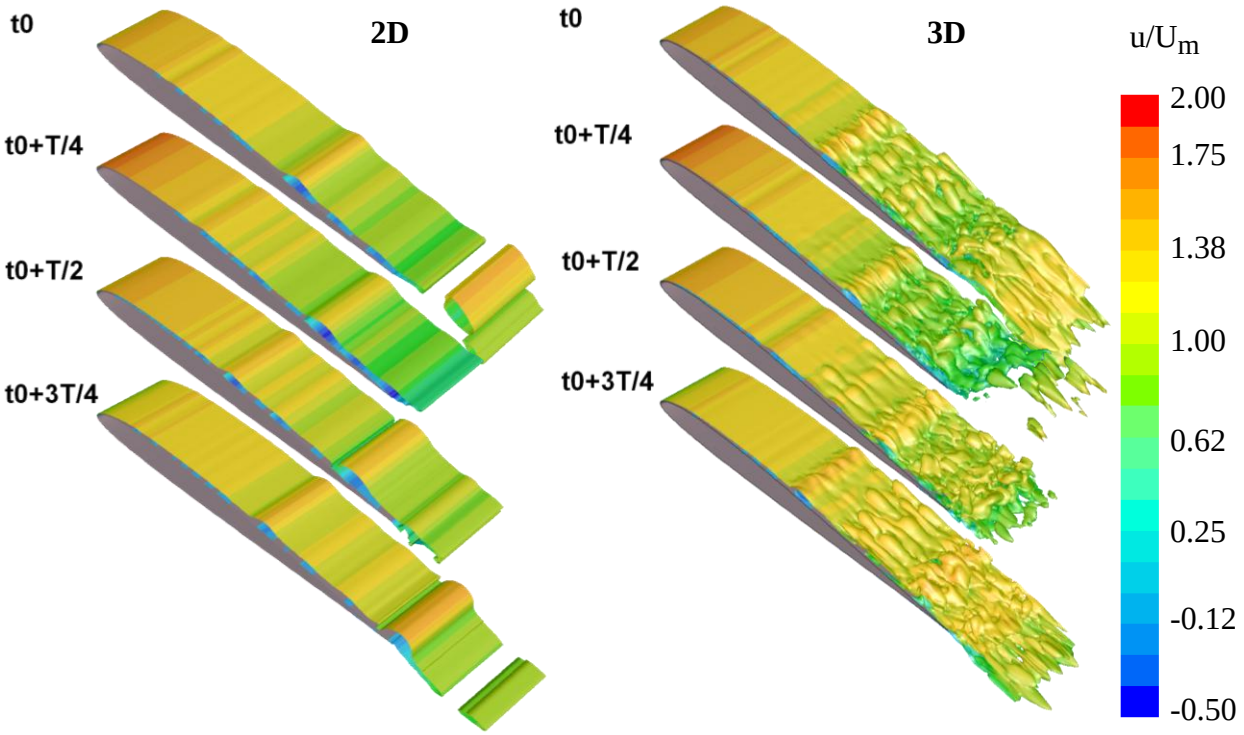

Figure 24: Iso-surfaces of z-vorticity ($\omega_z C/U_m = -10$) obtained by 2D and 3D simulations of the flow with oscillating AoA and Re=60,000.

The spanwise domain size Z/C=0.2 is selected based on Galbraith and Visbal findings [20, 23]. They compared solutions with spanwise extent ranging from 0.1C to 0.3C and concluded that Z/C≥0.1 is sufficient for capturing flow details in the spanwise direction. To further verify this, the size of flow vortices in planes perpendicular to the freestream direction was examined in the most "extreme" case with Re=60,000 and AoA=16° which involves relatively large vortical flow structures in comparison to cases with smaller AoAs. Contours of x-vorticity obtained from the LES data for AoA=16° case at several x/C locations are plotted in Figure 26, which shows that the size of almost all large-scale vortices in the spanwise direction is less than 1/5 of the spanwise extent. Therefore, flow properties in the spanwise direction are not affected by the chosen spanwise size.

Based on the above discussion, the 3D mesh with spanwise extent Z/C=0.2 will be used for all computations in the rest of this thesis.

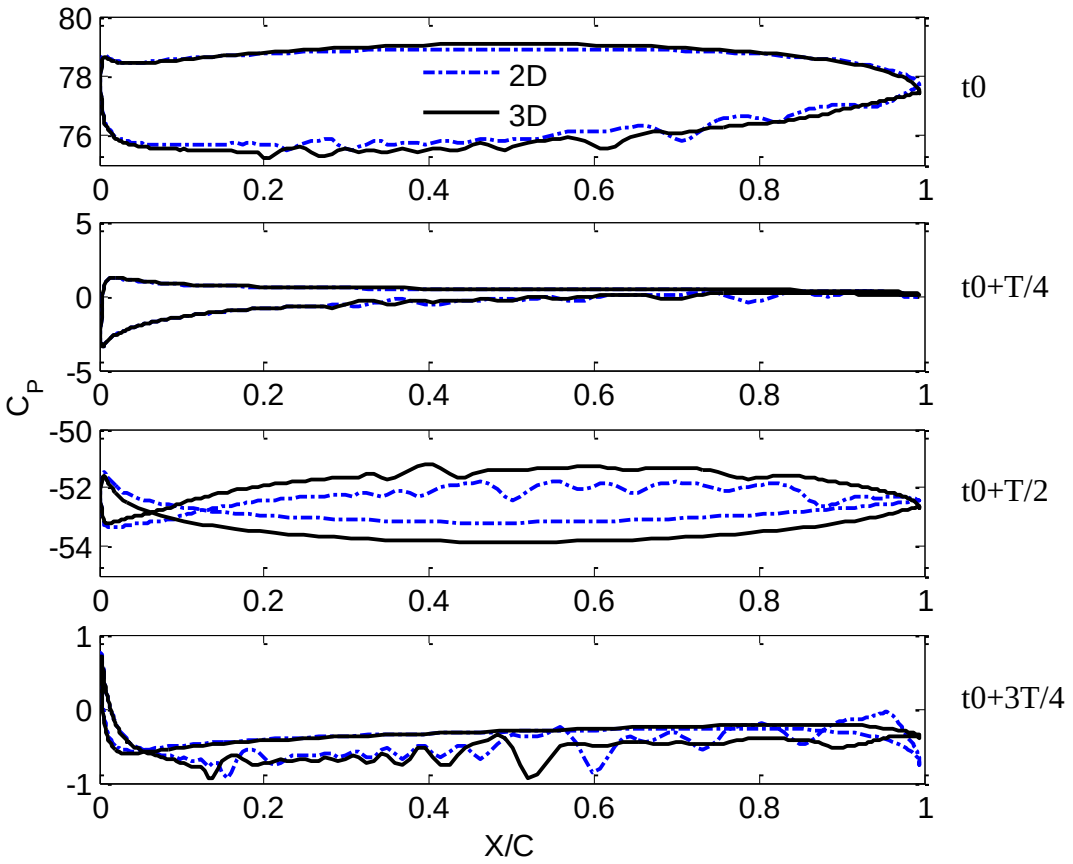

Figure 25: Pressure coefficient obtained by 2D and 3D simulations of the flow with oscillating AoA and Re=60,000.

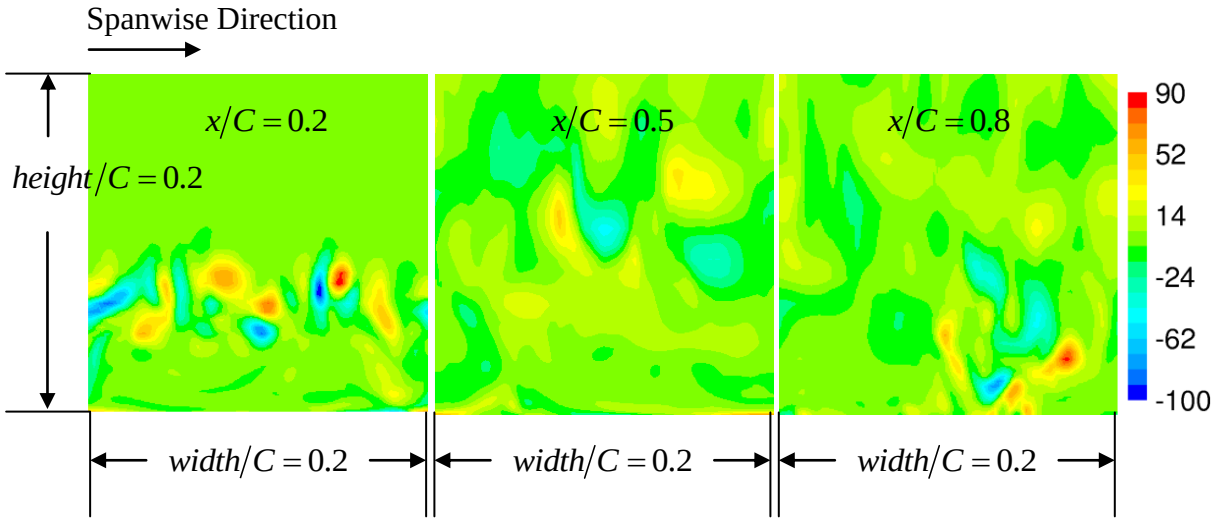

Figure 26: Instantaneous contours of x-vorticity ($\omega_x C/U_m$) obtained by 3D simulations of the flow with steady freestream and Re=60,000, AoA=16 °.

4. Large Eddy Simulations of Steady Freestream Flows over SD7003 Airfoil

To validate the computational method and to establish reference cases for comparison with unsteady flows considered in the next chapter, flows around SD7003 airfoil with steady freestream are computed in this chapter and compared to available experimental and computational data. The z-vorticity iso-surfaces of flows with Re=60,000 and AoA=4°, 8°, 12° and 16° as obtained by LES in Figure 27 show the general expected trend that at higher AoA the size of recirculation region over the airfoil is bigger and so are the sizes of the vortices formed by the separation. For steady flow conditions, high resolution velocity and Reynolds stress measurements have been reported by Radespiel et al. [8] whose experiments were conducted in a water channel and a low-noise wind tunnel at Technical University of Braunschweig (TU-BS). Detailed particle image velocimetry (PIV) measurements for the SD7003 airfoil were also conducted by Ol et al. [9] at the Air Force Research Laboratory (AFRL) water channel. Katz et al. [10-13] at Turbulent Mixing and Unsteady Aerodynamics Laboratory (TMUAL) at Michigan State University also measured the flow over SD7003 airfoil in a water channel with the molecular tagging velocimetry (MTV) method. Galbraith et al. [7] simulated steady flows over SD7003 airfoil with LES and a high-order low-pass filter as a SGS model. Results obtained by two compact differencing schemes (2nd-order and 6th-order) and two meshes (base-line mesh and overset mesh) were reported. The base-line mesh used in reference [7] is similar to the one used in our study, while the overset mesh has a refined region around the upper surface of the airfoil.

For the steady flow with Re=60,000 and AoA=4°, the predicted separation, transition, and reattachment points and lift and drag coefficients are compared to the numerical and experimental results in Table 3. These variables are defined in Section 3.5.

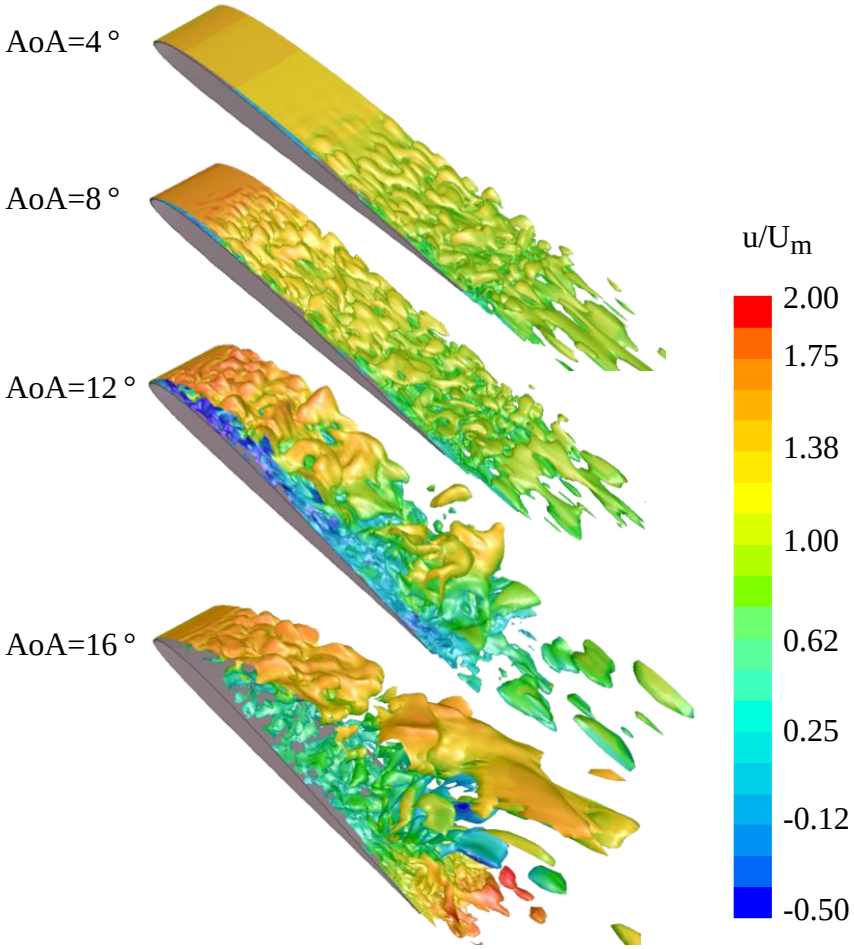

Figure 27: Instantaneous iso-surfaces of z-vorticity ($\omega_z C/U_m = -10$) for the flow with steady freestream, Re=60,000, AoA=4 °, 8 °, 12 °and 16 °.

Date Set	Separation X_s/C	Transition X_t/C	Reattachment X_r/C	Lift coeff. C_L	Drag Coeff. C_D
LES	0.25	0.50	0.64	0.59	0.020
Galbraith 2nd-order [20]	0.25	0.46	0.66	-	-
Galbraith 6th-order [20]	0.23	0.55	0.65	0.59	0.021
TU-BS [8]	0.30	0.53	0.62	-	-
AFRL [9]	0.18	0.47	0.58	0.56	-

Table 3: Computed and measured time-averaged data for the flow with steady freestream, Re=60,000 and AoA=4 °. LES refers to our simulations with WALE SGS model.

There are some quantitative differences between the computed data and the AFRL experimental data. According to Galbraith and Ol [20], some of these differences may be attributed to the fact that the tested airfoil had a tendency to vibrate at certain AoAs, promoting premature flow transition.

The LES predictions are generally in agreement with those measured in TU-BS wind tunnel, but seem to predict earlier separation and latter reattachment, thus a larger LSB. Similar trends are reported by Radespiel et al. [14], Yuan et al. [16], and Galbraith [20]. Part of the differences may be caused by the freestream turbulence intensity in the experimental facility [12, 29, 52]. Another possible reason is the reported discrepancy between the nominal and effective angles of attack due to interference effects in the wind tunnel.

Figures 28 and 29 compare the surface pressure coefficient C_P and skin friction coefficient C_F obtained from LES to those by Galbraith [20]. Our LES results obtained with a 2nd-order scheme are expected to be comparable to those of Galbraith obtained with the 2nd-order scheme. The comparison shows overall good agreement between the two LES results. However, our LES predictions seem to be closer to Galbraith baseline 6th-order and overset 6th-order predictions, instead of their baseline 2nd-order results.

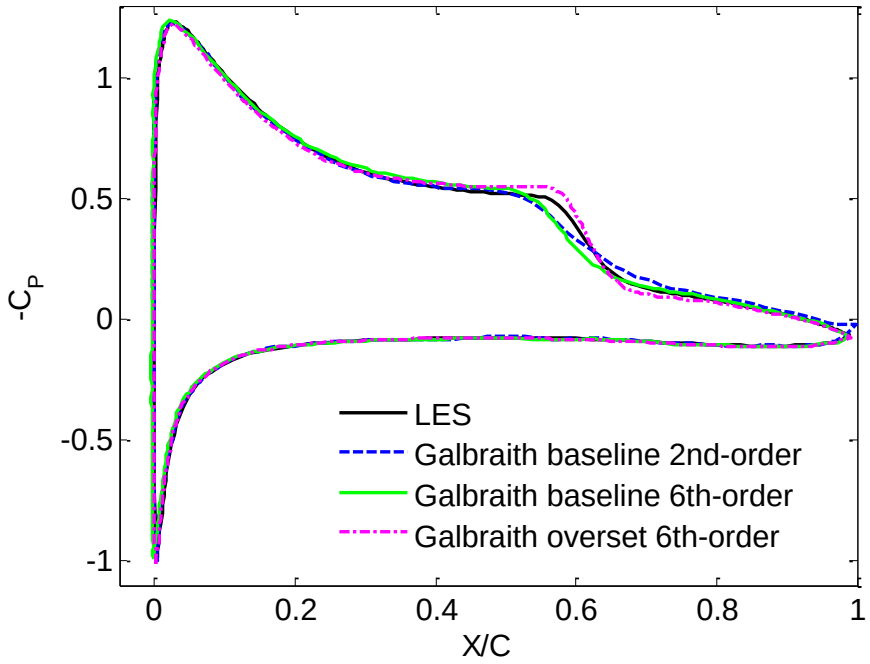

Figure 28: Time-averaged surface pressure coefficient for the flow with steady freestream, Re=60,000 and AoA=4 °.

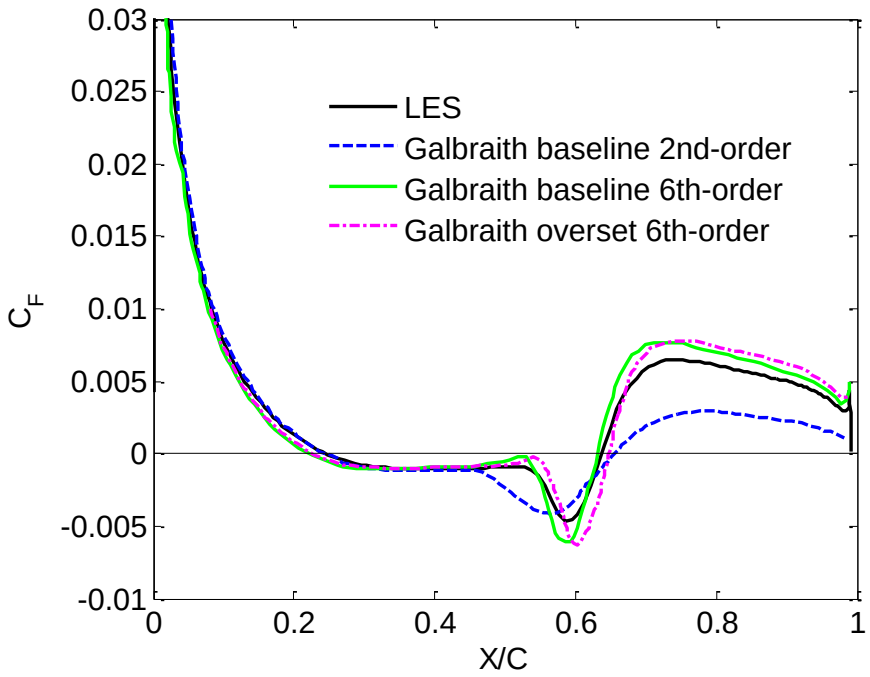

Figure 29: Time-averaged skin friction coefficient on the upper airfoil surface for the flow with steady freestream, Re=60,000 and AoA=4 °.

Table 4 and Figures 30 and 31 compare LES results for higher AoA of 8 ° and Reynolds number of 60,000. The trends and conclusions are similar to those shown above for the case with AoA=4 ° and Re=60,000. There seems to be a slight shift in the C_P and C_F curves predicted by the two LES models which is due to differences in the SGS model, mesh, and discretization method.

Date Set	Separation X_s/C	Transition X_t/C	Reattachment X_r/C	Lift Coeff. C_L	Drag Coeff. C_D
LES	0.042	0.16	0.25	0.93	0.040
Galbraith 6th-order	0.04	0.18	0.28	0.92	0.043

Table 4: Computed time-averaged data for the flow with steady freestream, Re=60,000 and AoA=8 °.

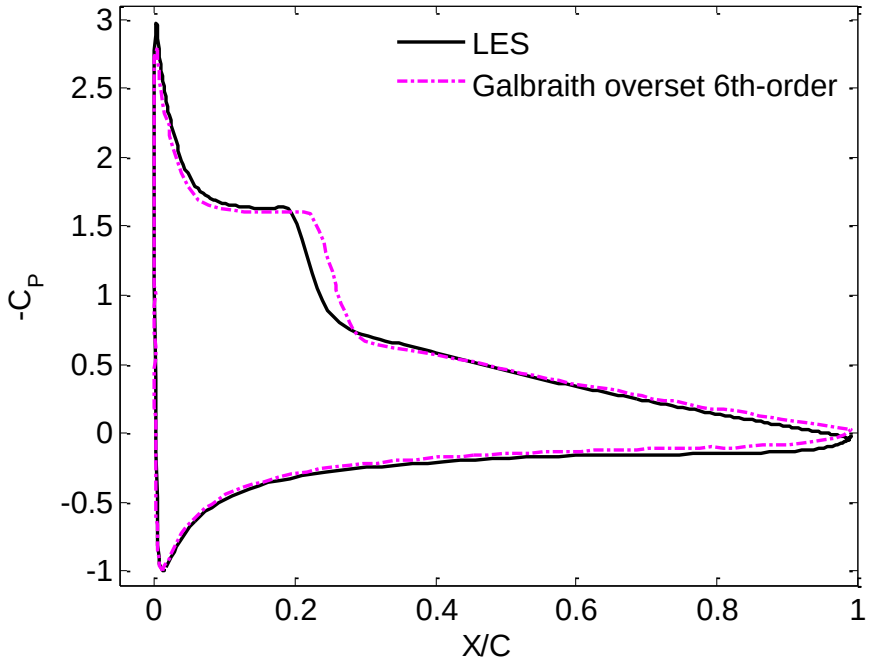

Figure 30: Time-averaged surface pressure coefficient for the flow with steady freestream, Re=60,000 and AoA=8 °.

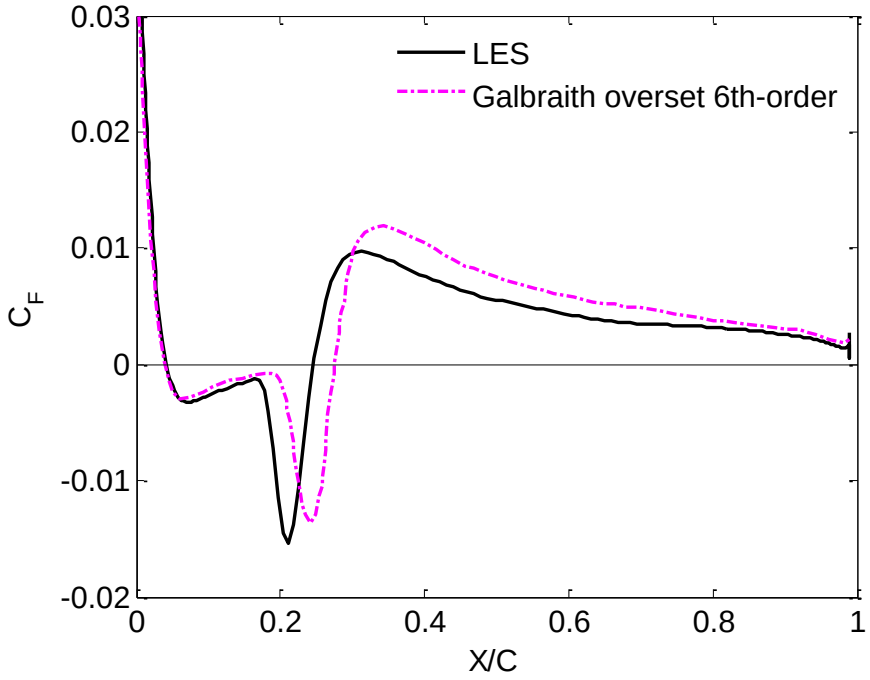

Figure 31: Time-averaged skin friction coefficient on the airfoil upper surface for the flow with steady freestream, Re=60,000 and AoA=8 °.

To consider a much more extreme case in terms of flow separation, the 3D flow over the airfoil for AoA=16 ° and Re=60,000 is also computed. The time- and spanwise-averaged data for this case are presented in Table 5. For comparison, the results for AoA=4 °, 8 °, and 12 ° are also listed. The instantaneous vorticity iso-surfaces for AoA=16 ° in Figure 27 clearly show the rapid separation of the flow at the leading edge. At this steep AoA, the flow is not able to recover the static pressure (as shown in the C_P plot in Figure 32) and thus cannot reattach to the airfoil surface. The AFRL measurements [9] show that the maximum C_L for SD7003 airfoil at this Reynolds number is around 1.05, and C_L drops to 0.96 at AoA=14 °. Following this trend, the predicted C_L=0.91 at AoA=16 ° seems reasonable. Since experimental and numerical data for the simulated Re and AoA are not available for direct comparison, the time-averaged pressure coefficient is compared with Galbraith [7] results at AoA=14 °, Re=60,000 in Figure 32. Also shown in this figure are the LES results for the same Reynolds number but lower AoAs of 4 ° and

8°. The difference between LES results at different AoA is much more significant on the upper side of the airfoil as expected. The overall trends observed in current LES results are similar to that of Galbraith, though minor differences exist.

AoA (°)	Separation X_s/C	Transition X_t/C	Reattachment X_r/C	Lift Coeff. C_L	Drag Coeff. C_D
4	0.25	0.50	0.64	0.59	0.020
8	0.042	0.16	0.25	0.93	0.040
12	0.008	-	0.92	1.14	0.124
16	0.006	-	-	0.91	0.277

Table 5: Time-averaged data for the flow with steady freestream, Re=60,000, and AoA=4°, 8°, 12°, 16°.

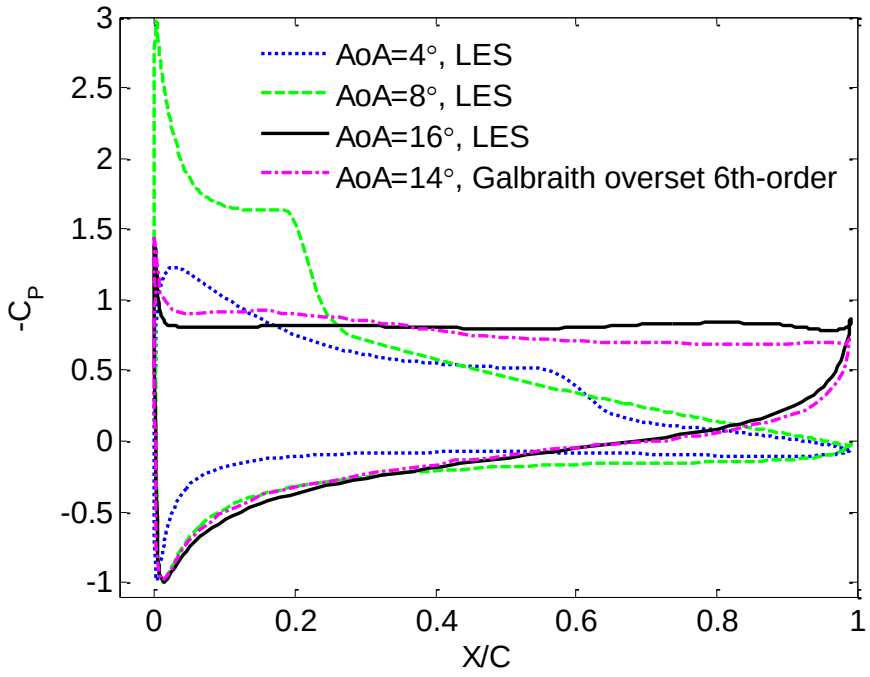

Figure 32: Time-averaged surface pressure coefficient for the flow with steady freestream at different AoAs and Re=60,000.

Katz et al. [11] at MSU's TMUAL conducted a series of water channel measurements for steady freestream flows around a fixed SD7003 airfoil using Molecular Tagging Velocimetry

(MTV) method. The reported freestream turbulence intensity in the water channel was about 2.8% of the mean freestream velocity. Also, the Reynolds number in this experiment varied from 20,000 to 40,000 and AoA varied from $3.75°$ to $10.44°$. These experiments are simulated here via LES. Table 6 compares the LES predictions and the experimental data. There are some differences between the numerical and experimental results. At relatively small AoAs, LES predicts earlier separation in comparison to experiment. The prediction of reattachment point is generally not as good as that of the separation point. Some of these differences are inevitably due to modeling and numerical issues. There could be some issues related to the experiment. One possible reason is the relatively high turbulence intensity in the water channel. Recent measurements by Olson [12] show that freestream turbulence will move the separation point downstream and move the reattachment point upstream. More discussion regarding the effect of freestream unsteadiness on mean separation and reattachment points is given in Section 5.3. Katz et al. [11] also reported uncertainty of $\pm 0.4°$ in the AoA measurement. This may be another reason for the discrepancy between numerical and experimental results.

Reynolds Number		20,000	30,000	40,000	
AoA (°)		3.75	7.39	5.49	10.44
Separation (X_s)	LES	0.303	0.063	0.121	0.017
	TMUAL	0.402	0.054	0.223	0.024
Reattachment (X_r)	LES	0.981	0.661	0.652	0.102
	TMUAL	0.994	0.438	0.526	0.144

Table 6: Separation and reattachment points obtained by LES and TMUAL experiments.

The lift and drag coefficients by LES for all steady freestream cases are compared in Figure 33. C_L and C_D for the cases with Re=60,000 have been compared to the available experimental and numerical results. For other Reynolds numbers and AoAs, we found no numerical or

experimental data for C_L and C_D in the literature. A rough comparison at data of different Reynolds numbers suggest that, for the same AoA, lift coefficient increases as Reynolds number increases, and drag coefficient decreases as Reynolds number increases. The same trend was observed in simulation results of Galbraith [20] at AoA=4 ° and 8 ° and Re=10,000 to 90,000.

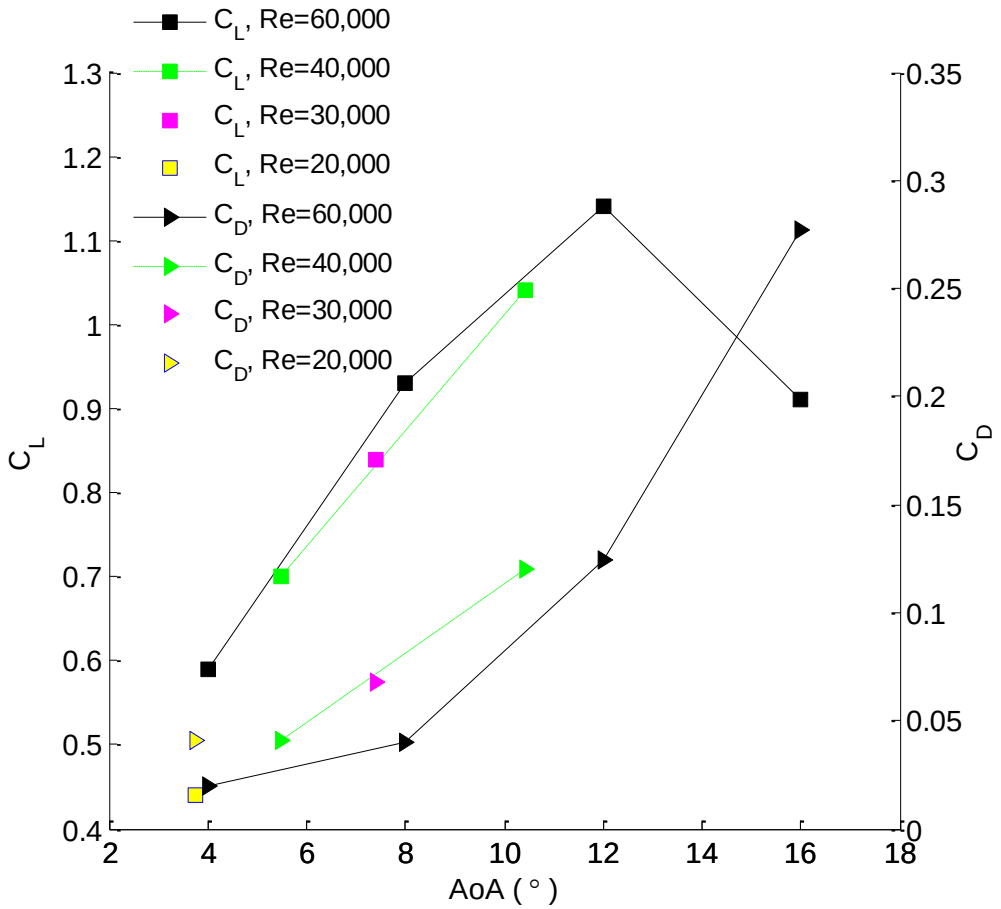

Figure 33: Time-averaged lift and drag coefficients obtained by LES for flows with steady freestream condition.

5. Large Eddy Simulation of Unsteady Freestream Flows over SD7003 Airfoil

In this chapter, 3D flows with unsteady freestream condition over SD7003 are computed by LES with the WALE model. The effects of flow unsteadiness on the aerodynamic force, boundary layer separation/reattachment, vorticity and velocity fluctuations are systematically studied. The unsteadiness in freestream flow is assumed to be simple and sinusoidal. Two sets of unsteady flows are considered. In Section 5.1, the freestream flow direction or AoA is fixed, while the freestream velocity magnitude or speed is varied harmonically in time. In Section 5.2, the freestream velocity magnitude is fixed, while the freestream flow direction or AoA is changed harmonically in time. The effect of freestream flow unsteadiness on boundary layer separation and reattachment is discussed in Section 5.3. Section 5.4 considers cases involving a wind gust.

5.1 Flows with Oscillating Freestream Velocity Magnitude

In this set of unsteady flows, the airfoil is fixed at $4°$ relative to the freestream flow direction or x-axis, so the AoA is fixed at $4°$ but the velocity magnitude oscillates sinusoidally in time according to Equation (37) (Figure 13). In this equation, U_m is the mean velocity magnitude, σ denotes the amplitude of freestream velocity oscillation normalized by the mean velocity, and $\omega = 2\pi f$ is the angular frequency. The reduced frequency is $k = \pi f C/U_m$ and the mean Reynolds number based on U_m is 60,000.

$$\begin{cases} \alpha = 4^\circ \\ U(t) = U_m\left(1+\sigma\sin(\omega t)\right) \\ V = W = 0 \end{cases} \tag{37}$$

Case	σ	k	C_L Mean	C_L Amplitude	C_D Mean	C_D Amplitude	X_S/C Mean	X_R/C Mean
Steady mean freestream	0	-	0.59	2.6×10^{-3} (standard deviation)	0.020	2.5×10^{-4} (standard deviation)	0.25	0.64
U1	0.183	2π	0.56	0.43	0.021	0.485	0.33	0.53
U2	0.183	π	0.57	0.25	0.020	0.243	0.33	0.51
U3	0.183	$\pi/2$	0.57	0.18	0.020	0.123	0.33	0.46
U4	0.183	$\pi/4$	0.57	0.17	0.020	0.063	0.33	0.44
U5	0.183	$\pi/8$	0.57	0.16	0.020	0.033	0.32	0.47
U6	0.366	2π	0.60	0.86	0.021	0.968	0.30	0.53
U7	0.366	π	0.60	0.49	0.020	0.489	0.32	0.49
U8	0.366	$\pi/2$	0.60	0.36	0.020	0.248	0.31	0.35
U9	0.366	$\pi/4$	0.60	0.34	0.020	0.126	0.31	0.37
U10	0.366	$\pi/8$	0.60	0.33	0.020	0.066	0.32	0.40

Table 7: Mean quantities for cases with oscillating velocity magnitude.

Table 7 lists the flow parameters for ten simulated cases with unsteady freestream speed (labeled U1 to U10). In cases U1-U5 and cases U6-U10 the amplitude of oscillations is the same but the frequencies are different. The amplitudes and frequencies chosen cover a range of these parameters limited by the LES grid. The force coefficients discussed below are defined in Section 3.5.

5.1.1 Aerodynamic forces

Figures 34-37 show the variation of C_L and C_D during a cycle after the flows have fully developed under the periodic freestream condition. In these figures, a negative C_D value implies a net thrust force on the airfoil. Both C_L and C_D oscillate periodically with the frequency of the freestream velocity, and a phase shift with respect to freestream velocity which is a function of the reduced frequency and freestream velocity amplitude. The mean and amplitude of lift and

drag coefficients are listed in Table 7 along with data for the steady freestream flow with AoA=4° and Re=60,000. Low values of the standard deviation of C_L and C_D in Table 7 for the steady flow indicate that lift and drag forces are constant when there is no oscillation in freestream velocity. Interestingly, Table 7 also show that the freestream velocity oscillation has little or no effect on the mean C_L and C_D which stay close to their steady freestream values. A comparison between cases U1~U5 and cases U6~U10 (five pairs: U1-U6, U2-U7, …, U5-U10) shows that the mean lift increases slightly (around 5%) when the freestream amplitude is doubled.

C_L and C_D in Figures 34-37 are normalized by the mean freestream velocity U_m as explained in Section 3.5. If the instantaneous freestream velocity U(t) is used for the normalization, a new set of lift and drag coefficients can be defined/computed as $C_L^* = L/(\rho U(t)^2 C/2)$ and $C_D^* = D/(\rho U(t)^2 C/2)$ which are plotted in Figures 38-39 for cases U6-10. Evidentially, the time profiles of C_L^* and C_D^* are significantly different from those of C_L and C_D and are no longer "sinusoidal-like".

Figure 40 shows amplitudes of fluctuations in C_L and C_D as functions of reduced frequency k and the amplitude of freestream velocity oscillation σ. Evidently, C_D amplitude increases linearly with the reduced frequency. However, C_L is not fully linear with respect to the reduced frequency. At relatively low reduced frequency, C_L amplitude increases slowly with increasing reduced frequency. At higher reduced frequency, C_L amplitude increases faster and its relation with the reduced frequency seems to become closer to being linear. At any reduced frequencies considered in this study, doubling the amplitude of freestream velocity oscillation causes both C_L and C_D amplitudes to double, suggesting a linear relation between the amplitude of freestream velocity oscillation and the aerodynamic forces. Figure 40 also shows comparison with the Greenberg theory [53] which will be discussed later.

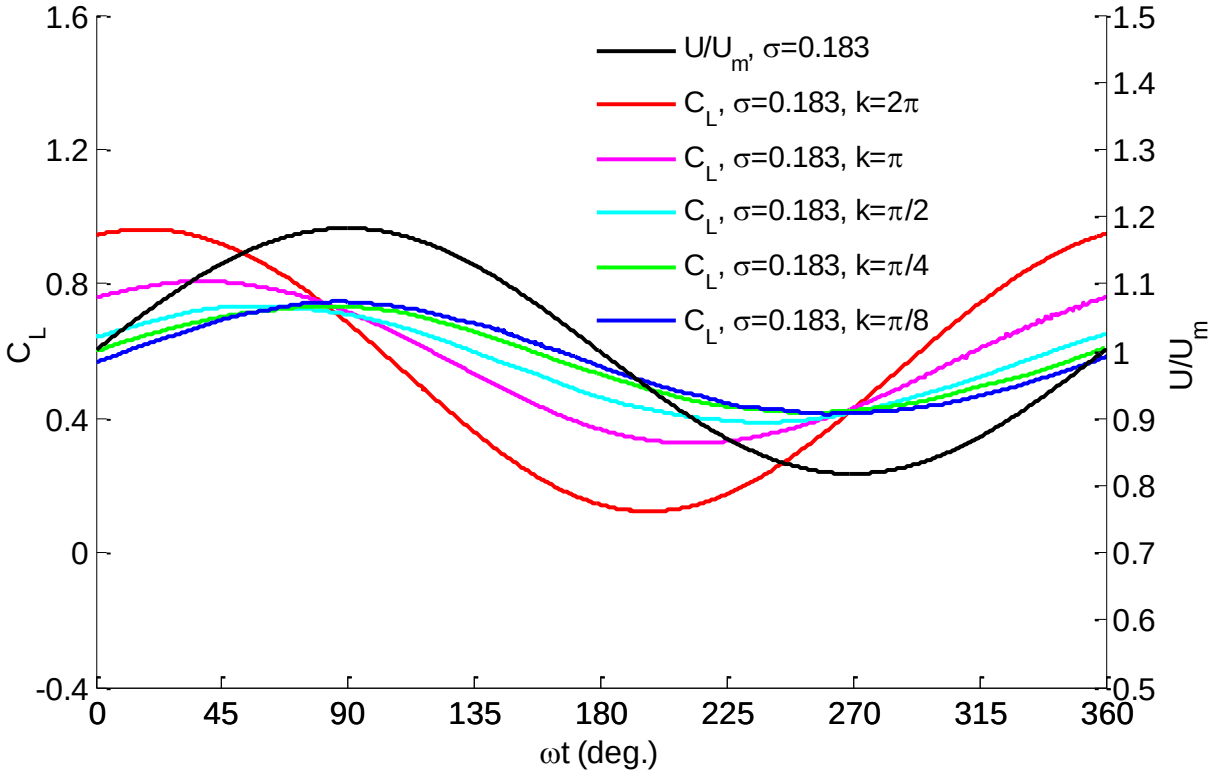

Figure 34: Time variations C_L for flows with oscillating freestream speed (cases U1-5).

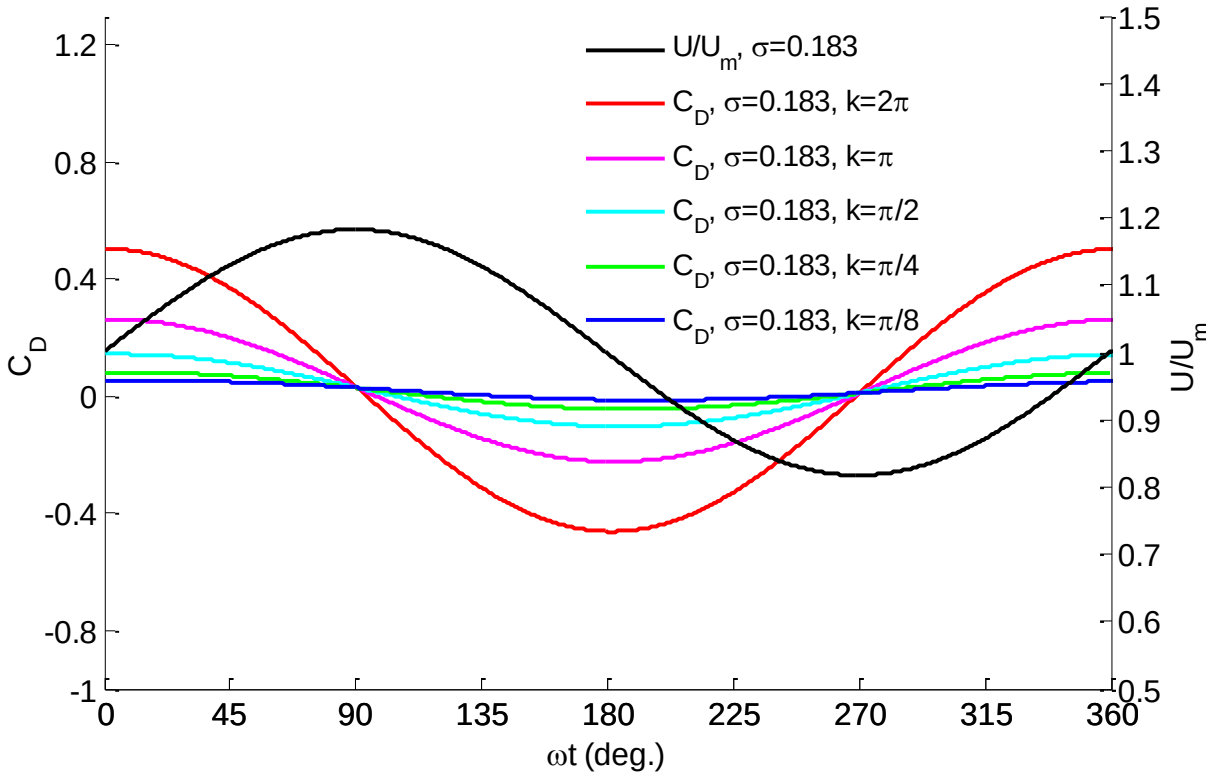

Figure 35: Time variations of C_D for flows with oscillating freestream speed (cases U1-5).

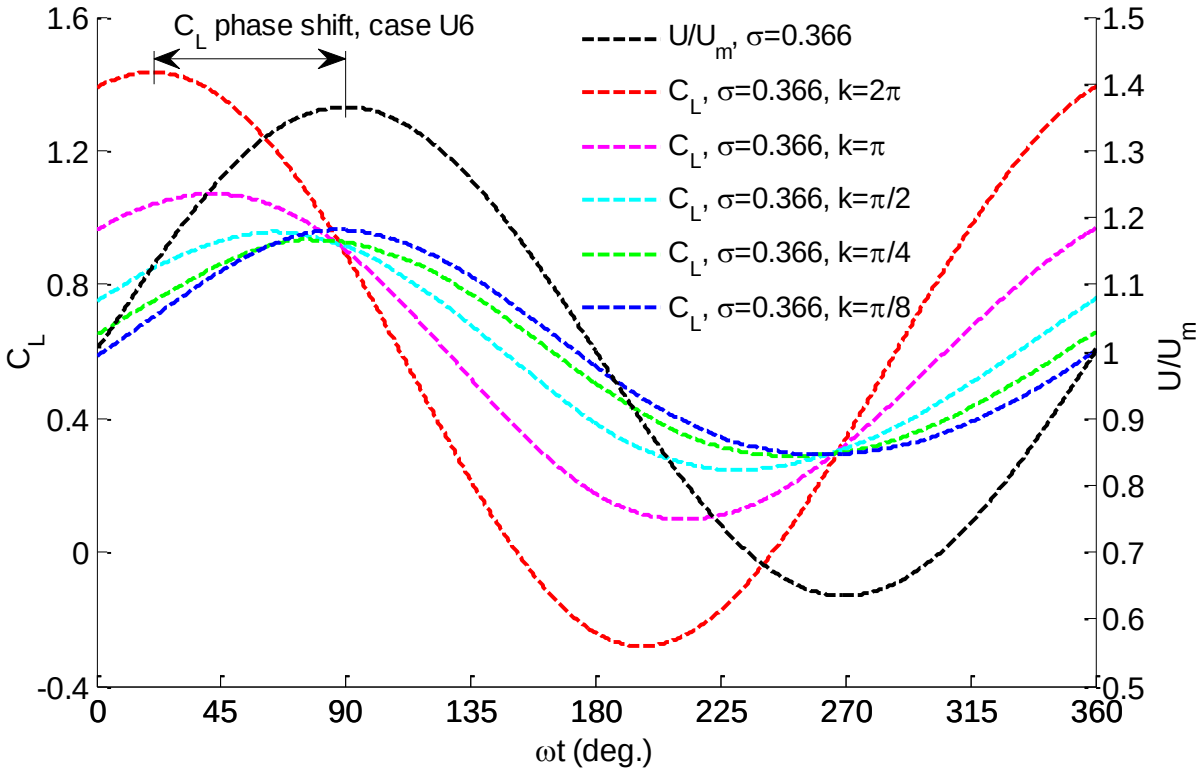

Figure 36: Time variations of C_L for flows with oscillating freestream speed (cases U6-10). The phase shift for one of the cases is shown as an example.

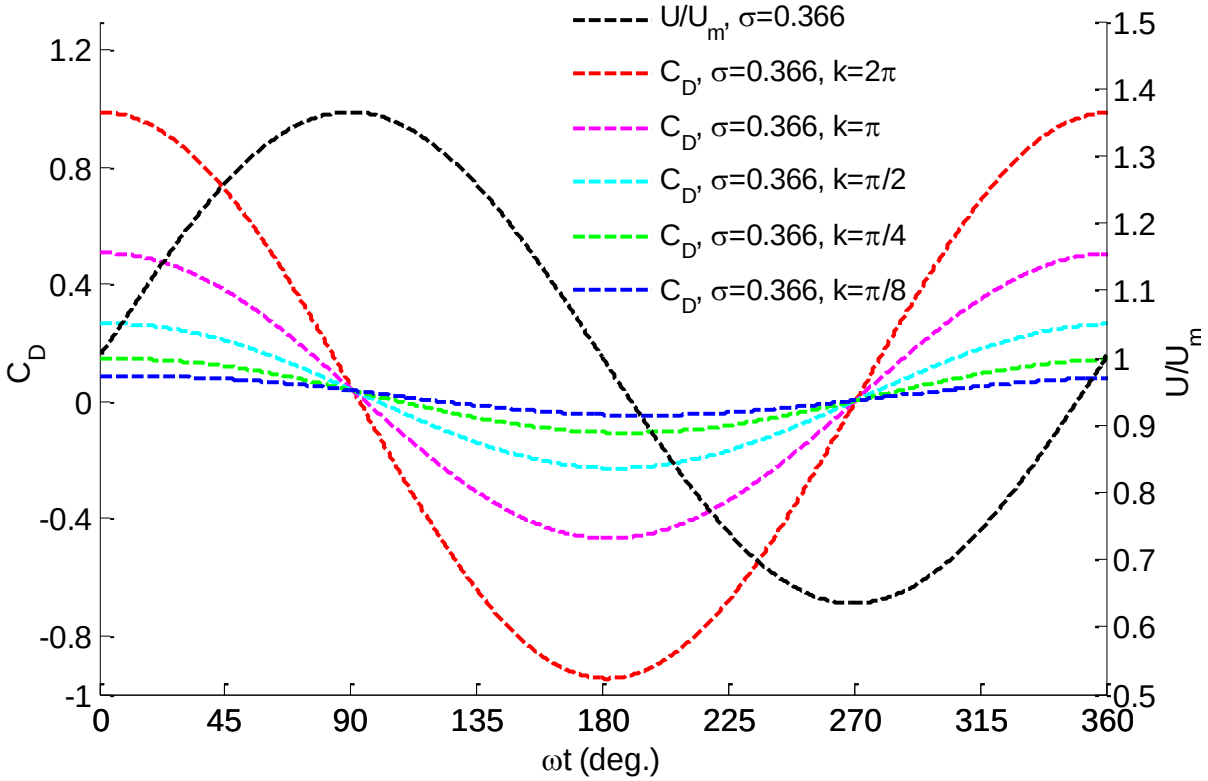

Figure 37: Time variations of C_D for flows with oscillating freestream speed (cases U6-10).

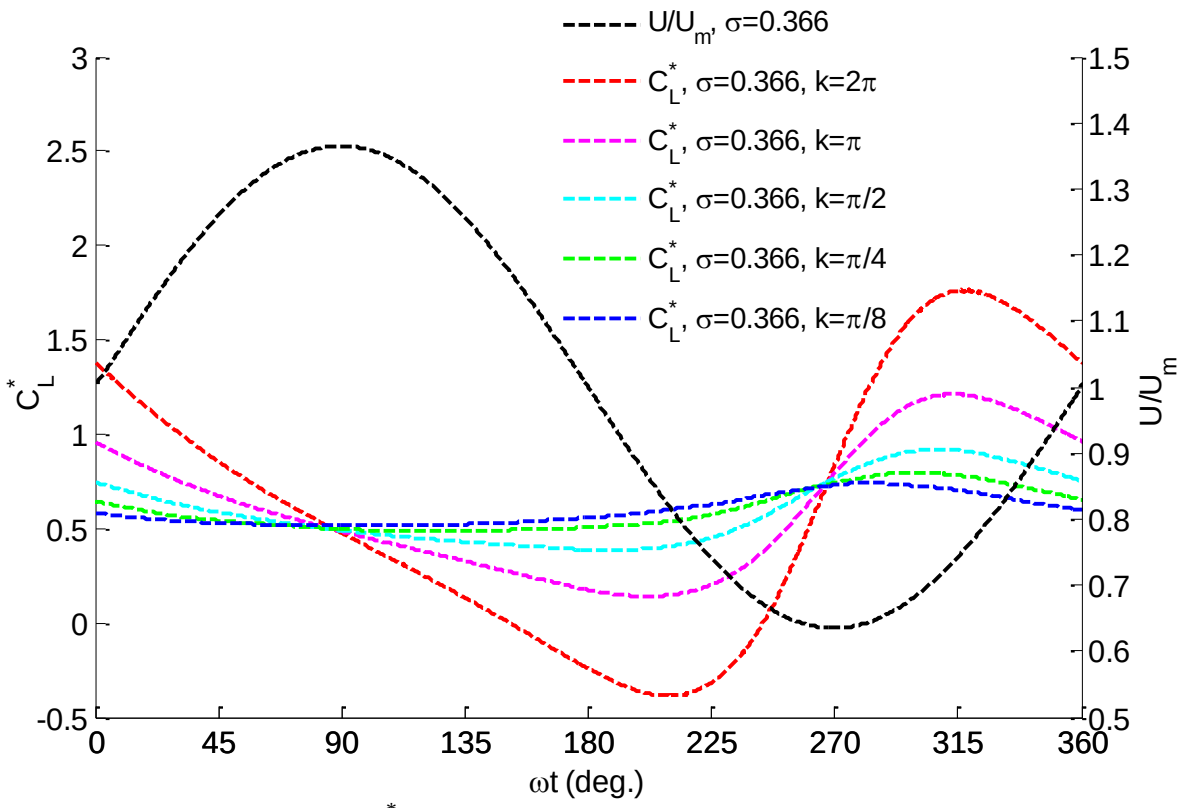

Figure 38: Time variations of C_L^* for flows with oscillating freestream speed (cases U6-10).

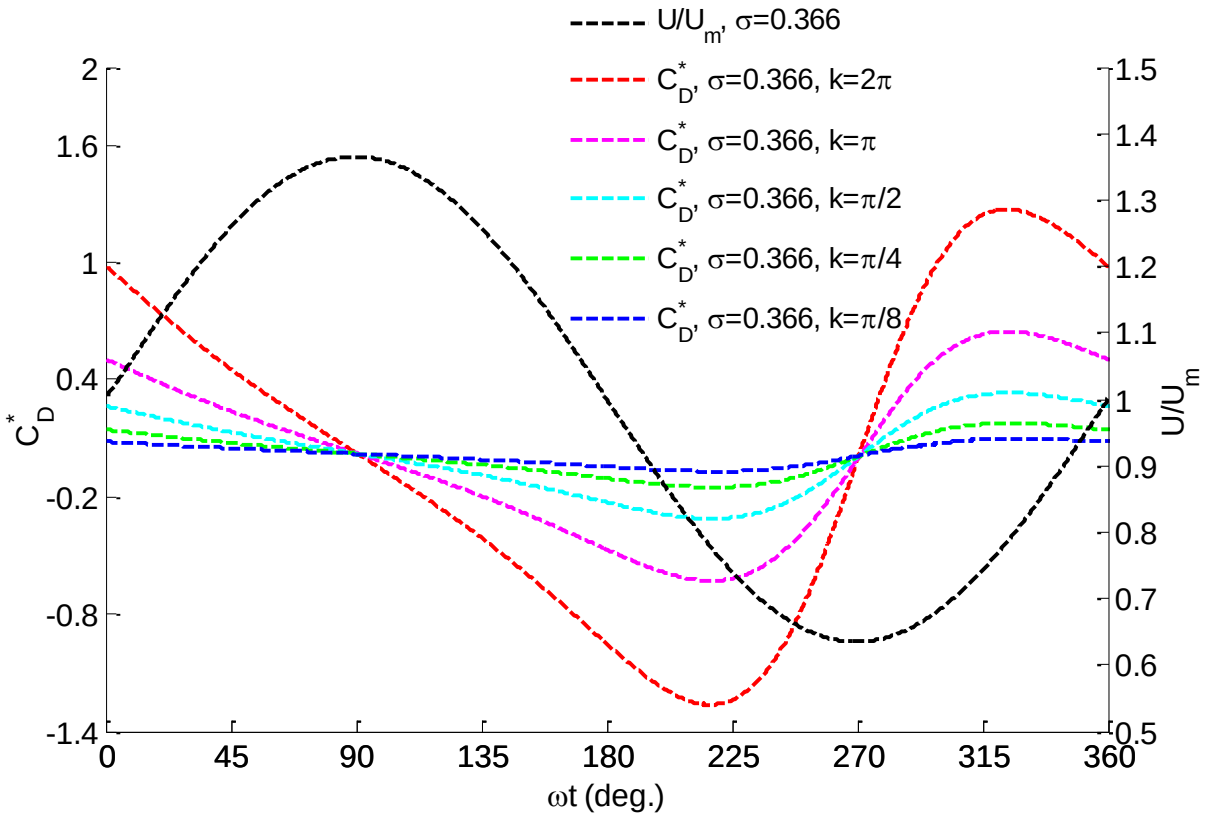

Figure 39: Time variations of C_D^* for flows with oscillating freestream speed (cases U6-10).

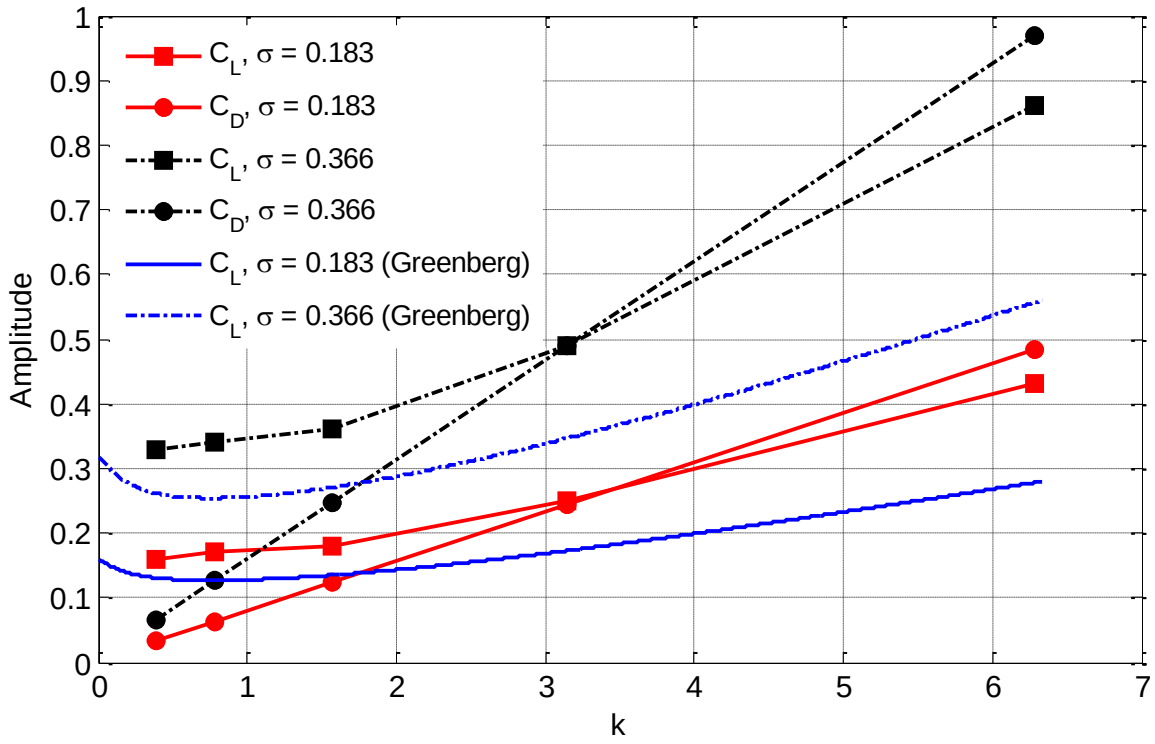

Figure 40: Amplitude of C_L and C_D for flows with oscillating freestream velocity magnitude.

Figures 34-37 show that the phase of aerodynamic forces leads those of the freestream velocity. This is shown better in Figure 41 which plots the phase shift between the freestream velocity oscillations and lift/drag oscillations for different reduced frequency and amplitude. The phase shift is defined as the phase difference between the maximum lift (or drag) and the maximum freestream velocity. Unlike amplitudes of C_L and C_D which are significantly affected by σ, Figure 41 shows that the phase shift is slightly affected by σ and is mainly dependent on the reduced frequency. For both lift and drag, the phase shift increases as reduced frequency increases, more so at lower frequencies. For the considered range of reduced frequency ($\pi/8$ ~ 2π), C_D phase shift with respect to freestream velocity varies between 70 and 90 degrees. At high reduced frequencies, C_D phase shift seems to asymptotically approach 90 degrees, indicating that the maximum drag coincides with the maximum acceleration of freestream velocity (instead of the maximum velocity magnitude). For the same range of reduced frequency, C_L phase shift has

a much wider range with the maximum value being around 70 degrees and a minimum close to zero. However, the rate of increase in phase shift decreases at higher reduced frequencies. At low freestream frequency, C_L phase shift quickly drops to zero.

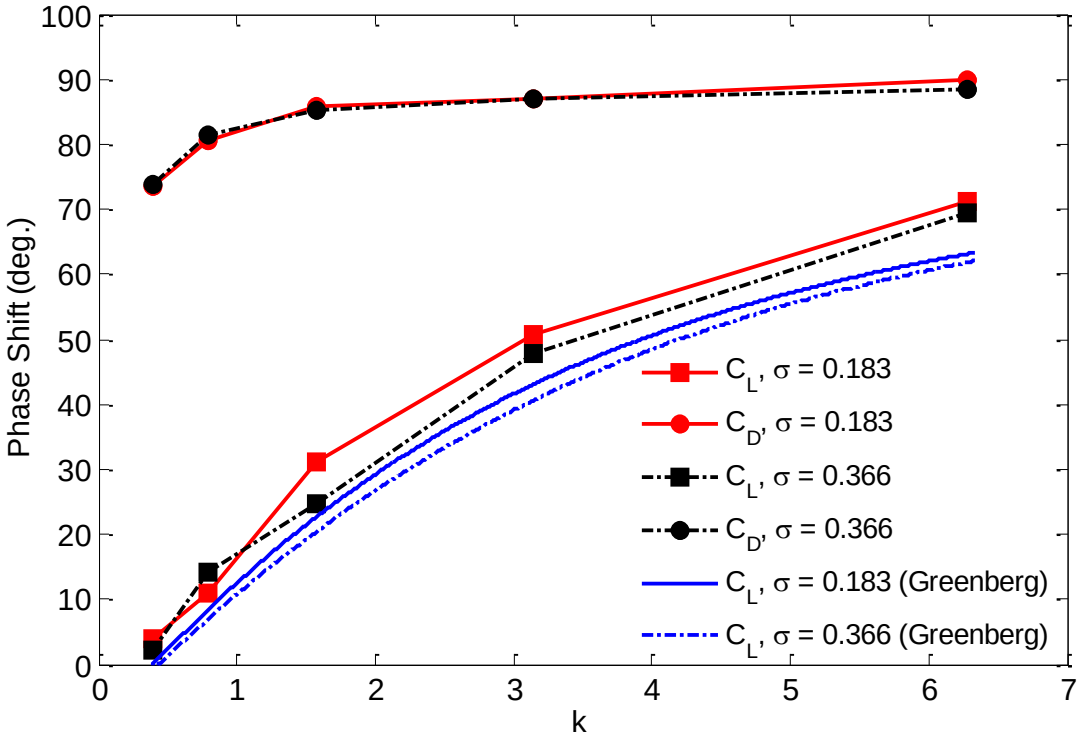

Figure 41: Phase shift between force coefficients and freestream velocity for flows with oscillating freestream velocity magnitude.

The LES predictions of the C_L amplitude and its phase shift are compared with the inviscid Greenberg's theory [53] in Figures 40 and 41. According to Greenberg's theory, the lift coefficient is obtained from Equation (38), where $C_{L,m}$ is the lift coefficient of the steady freestream flow obtained by the thin airfoil theory [54] as $C_{L,m} = 2\pi\alpha$.

$$\frac{C_L}{C_{L,m}} = \left(1+\frac{\sigma^2 F}{2}\right)+\sigma\left(\frac{k}{2}+G\right)\cos\omega t+\sigma\left(1+F\right)\sin\omega t - \frac{\sigma^2 F}{2}\cos 2\omega t+\frac{\sigma^2 G}{2}\sin 2\omega t \tag{38}$$

Variables F and G in Equation (38) are the real and imaginary parts of the Theodorsen's function [26] both functions of the reduced frequency k. In Figure 40, the two Greenberg C_L amplitude curves have different rates at the same reduced frequency since σ appears as an independent variable in Equation (38). For C_L amplitude, LES values are higher than those predicted by Greenberg's theory. However, the C_L phase shift obtained from LES data compares much more favorably with Greenberg's theory. The inviscid theory predicts that the harmonic freestream velocity oscillations do not affect the mean C_L which still takes the steady freestream flow value of 0.44. Indeed, the mean C_L computed by LES for all ten unsteady cases match the steady flow C_L, even though the LES values are generally higher than those of the inviscid theory. Greenberg's theory is based on the assumptions that the flow is two-dimensional, fully attached over the airfoil, and the wake is planar. These assumptions are not completely true for the 3D flows studied here, suggesting why the results predicted by the 3D LES do not match very well with the inviscid theory.

At high reduced frequencies, Figure 41 indicates that the maximum C_L values coincide with the maximum freestream velocity acceleration. To explain this behavior, the airfoil surface pressure coefficient C_P at the time of maximum acceleration of freestream velocity for two "high" frequency cases U6 and U7 is shown in Figure 42. The pressure component of the lift coefficient is obtained directly from the integral of C_P over the airfoil surface. For the two cases considered in Figure 42, the pressure component makes up almost the entire lift and the viscous component is negligible. Our LES results (Figure 43), as expected, indicate that the surface pressure is strongly affected by the freestream pressure. In the freestream, both the y- and z-velocities are zero and the x-velocity is spatially uniform. When gravity is further neglected, the momentum equations are reduced to Equation (39) and then Equation (40) for the x-velocity.

Equation (40) indicates that the freestream pressure gradient in x-direction is proportional to the freestream acceleration and at higher frequencies higher pressure gradient around the airfoil is expected to develop. This will lead to higher pressure difference between the lower and upper airfoil surfaces, and thus high amplitude of the lift coefficient.

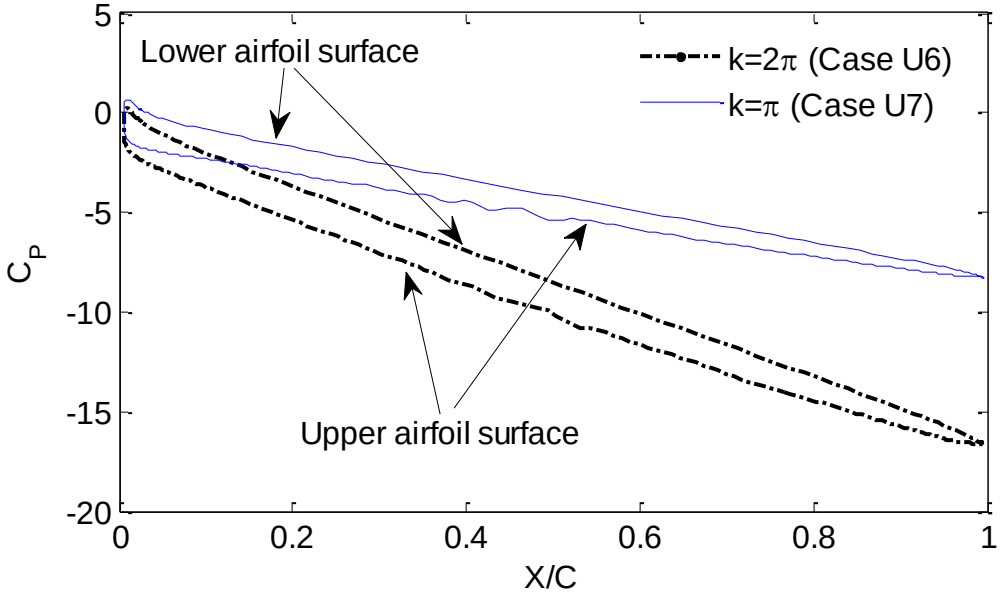

Figure 42: Pressure coefficient on the airfoil surface at the time of maximum acceleration of freestream velocity for case U6 with $k = 2\pi$ and $\sigma = 0.366$ and case U7 with $k = \pi$ and $\sigma = 0.366$.

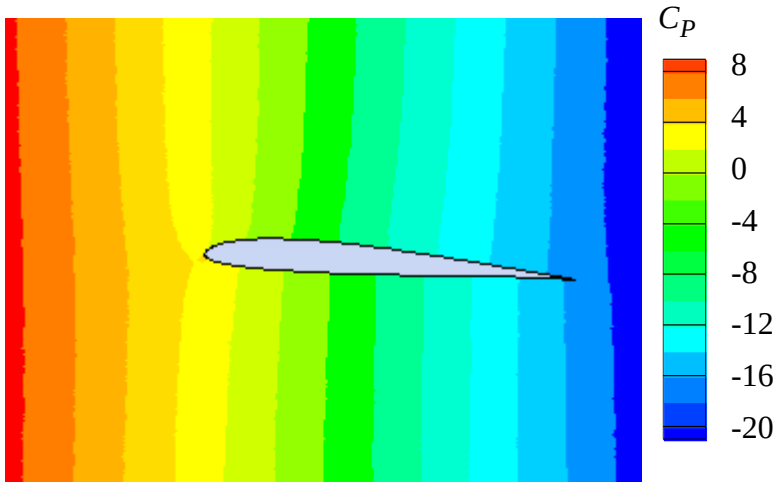

Figure 43: Pressure coefficient around the airfoil at the time of maximum acceleration of freestream velocity for case U6 with $k = 2\pi$ and $\sigma = 0.366$.

$$\rho\left(\frac{\partial u}{\partial t}+u\frac{\partial u}{\partial x}+v\frac{\partial u}{\partial y}+w\frac{\partial u}{\partial z}\right)=-\frac{\partial p}{\partial x}+\mu\left(\frac{\partial^2 u}{\partial x^2}+\frac{\partial^2 u}{\partial x^2}+\frac{\partial^2 u}{\partial x^2}\right)+\rho g_x \tag{39}$$

$$\frac{\partial p}{\partial x}=-\rho\frac{\partial u}{\partial t} \tag{40}$$

5.1.2 Vorticity field

The instantaneous vorticity fields for flows with oscillating freestream velocity magnitude are compared to those of the steady freestream flow in Figures 45-59. For each flow, the 3D iso-surfaces of the z-vorticity component, the 2D contours of spanwise-averaged z-vorticity component, and the line integrals of the spanwise-averaged vorticity magnitude are shown. All iso-surfaces are set to have the same normalized z-vorticity value of $\omega_z C/U_m=-10$. A line is drawn across the four snapshots for a better comparison. It should be noted that the vortices formed far beyond the trailing edge are not accurately computed because of the relatively coarse mesh used in regions away from the airfoil. To quantify the vorticity field, the normalized spanwise-averaged vorticity magnitude $|\Omega|=\frac{C}{U_m}\sqrt{\omega_x^2+\omega_y^2+\omega_z^2}$ is integrated along the airfoil surface normal and tangent direction (n and s axes in Figure 44, n and s are normalized by the airfoil chord C). The spanwise-averaged vorticity magnitude which is an indication of vorticity strength is integrated along the n axis from the airfoil surface to the far-field boundary of the computational domain, i.e. $\int|\Omega|dn$. The spike in $\int|\Omega|dn$ close to the trailing edge is due to rapid and local formation of the wake at the trailing edge. The profile of $\int|\Omega|dn$ oscillates considerably in the recirculation region, which makes it difficult to compare vorticity values at different times. To get a better picture of how vorticity magnitude changes over time, $\int|\Omega|dn$ is

further integrated along the s axis from the leading edge to the trailing edge on the upper surface as $\int\int|\Omega|dnds$.

Figures 45-47 show that the vorticity field over the airfoil does not significantly change in time in the steady freestream flow, despite significant variations of the vorticity and vorticity magnitude over the airfoil. Even though there are considerable fluctuations in vorticity magnitude in the recirculation region, the line integral of the spanwise-averaged vorticity magnitude stays almost constant in time. For the flows with oscillating freestream velocity magnitude, the vorticity field and magnitude vary much more significantly in time. It appears in the iso-surface plots of vorticity that the separation point moves back and forth during each cycle depending on the reduced frequency and amplitude of the freestream velocity oscillations. At high reduced frequencies (Figures 49 and 55), the fast oscillating freestream flow seems to promote the formation of distinct vortices which convect downstream and break down to smaller vortices near the trailing edge (as shown by arrows in Figure 55). This is not seen in flows with low reduced frequencies (Figures 52 and 58). The integrated vorticity magnitude ($\int|\Omega|dn$ or $\int\int|\Omega|dnds$) clearly vary in time much more than that observed for steady freestream flow. For all cases with oscillating freestream velocity magnitude, $\int\int|\Omega|dnds$ values correlate well with the freestream velocity magnitude, and for the time instants shown in Figures 50, 53, 56 and 59, the maximum (minimum) value of $\int\int|\Omega|dnds$ coincides with the maximum (minimum) freestream velocity magnitude. At t0 and t0+T/2, the freestream velocity magnitudes are the same, and values of the integral $\int\int|\Omega|dnds$ are relatively close; the small difference could be due to possible phase shift between the maximum $\int\int|\Omega|dnds$ and the maximum freestream velocity.

A direct comparison between unsteady cases (cases U1 U5, U6 and U10) in Figure 60 indicates that the integrated vorticity values ($\int |\Omega| dn$) on the airfoil upper surface for different k and σ start to show fluctuations around X/C=0.3. It will be shown in Section 5.1.4 that X/C=0.3 is close to the mean separation point for all unsteady cases listed in Table 7. Clearly and expectedly, the vorticity magnitude and the deviation between different unsteady flows are significant at or after the separation point. At later phases, e.g. at t0+3T/4, the vorticity magnitude for different cases with different k and σ start to deviate from each other much sooner at locations closer to the leading edge. This can be perhaps related to the shift of the separation point upstream toward the leading edge.

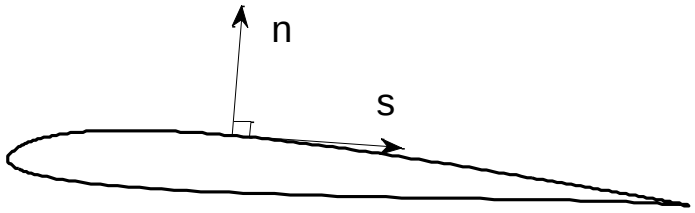

Figure 44: The n-s coordinate system around the airfoil surface.

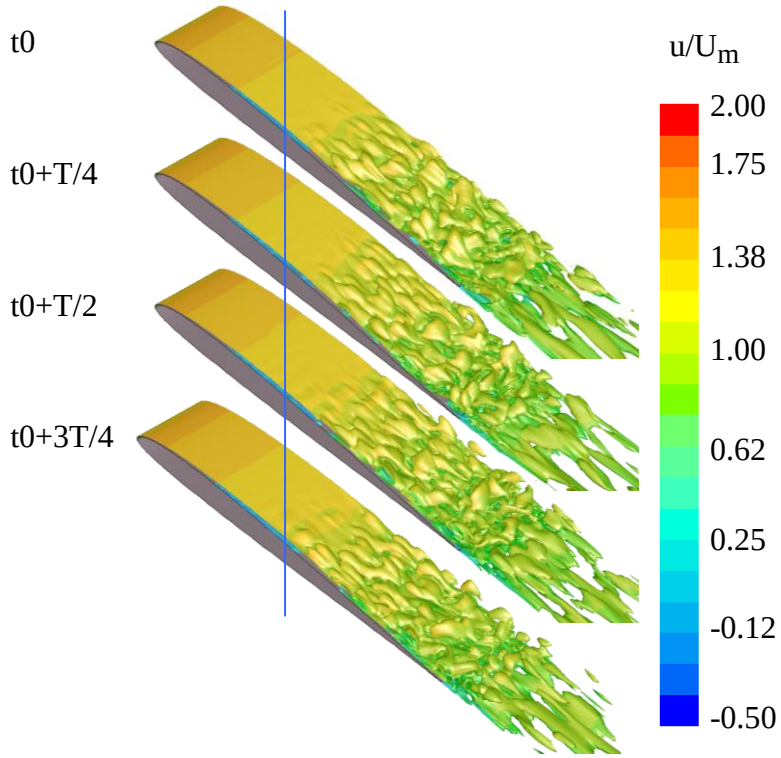

Figure 45: Instantaneous iso-surfaces of z-vorticity ($\omega_z C/U_m = -10$) during one residence time for the flow with steady freestream, Re=60,000, AoA=4°. (T is the residence time C/U_m , same for Figures 46-47).

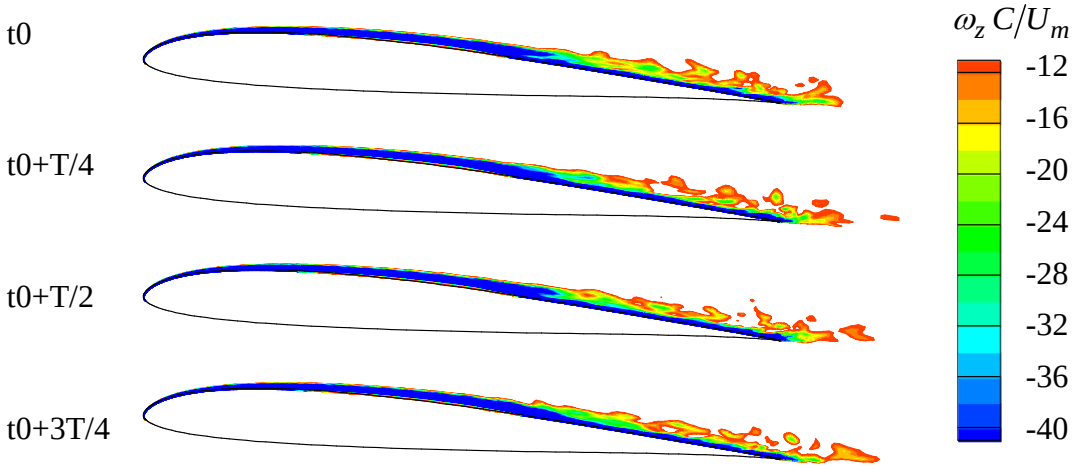

Figure 46: Instantaneous contours of spanwise-averaged z-vorticity ($\omega_z C/U_m$) during one residence time for the flow with steady freestream, Re=60,000, AoA=4°.

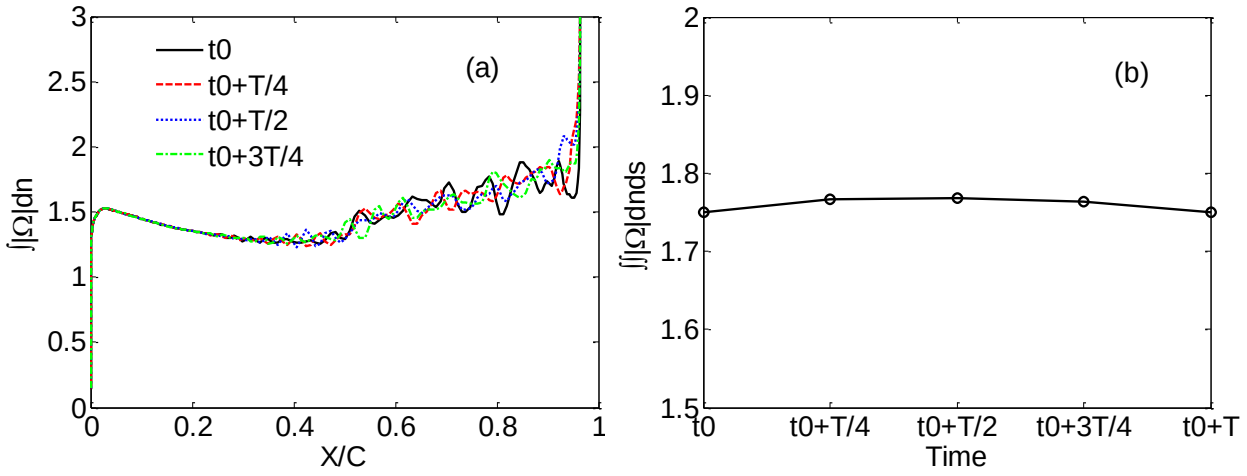

Figure 47: Integrals of spanwise-averaged vorticity magnitude |Ω| for the flow with steady freestream, Re=60,000, AoA=4°. (a) Integrated along n axis; (b) integrated along n and then s axes.

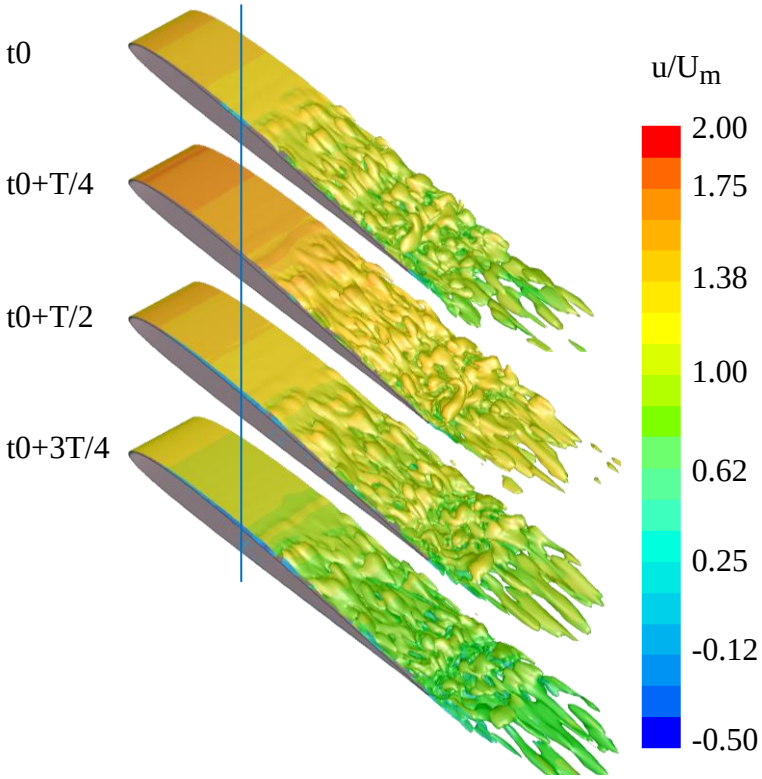

Figure 48: Instantaneous iso-surfaces of z-vorticity ($\omega_z C/U_m = -10$) during one cycle for case U1 with $k = 2\pi$ and $\sigma = 0.183$. (t0 is the beginning of the cycle when U equals Um and is increasing. T is the period. Same for Figures 49-60)

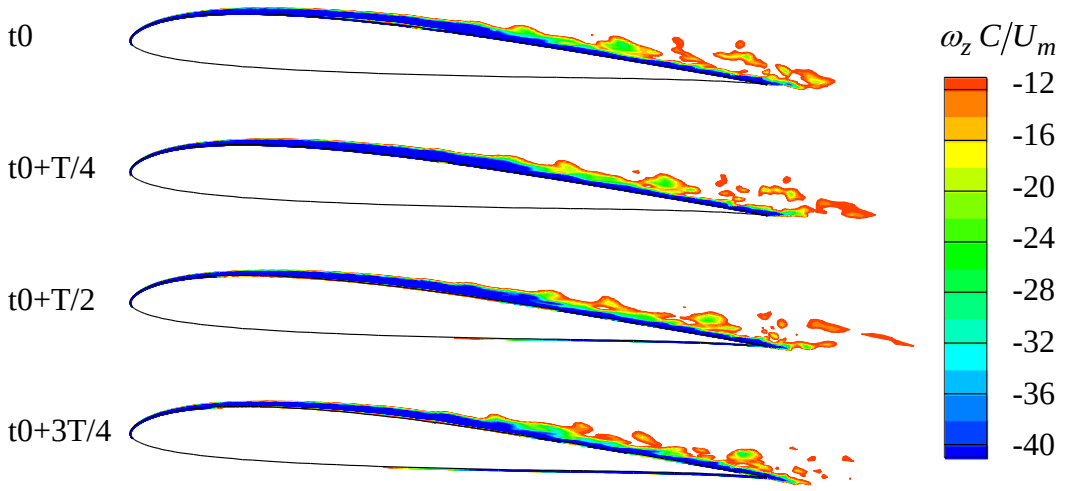

Figure 49: Instantaneous contours of spanwise-averaged z-vorticity ($\omega_z C/U_m$) during one cycle for case U1 with $k = 2\pi$ and $\sigma = 0.183$.

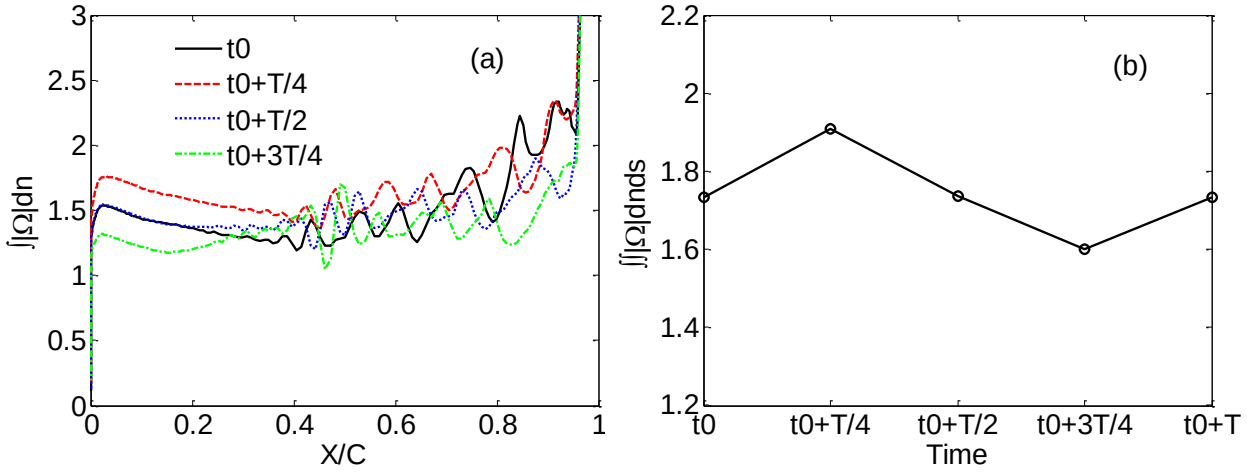

Figure 50: Integrals of spanwise-averaged vorticity magnitude |Ω| for case U1 with $k = 2\pi$ and $\sigma = 0.183$. (a) Integrated along n axis; (b) integrated along n and then s axes.

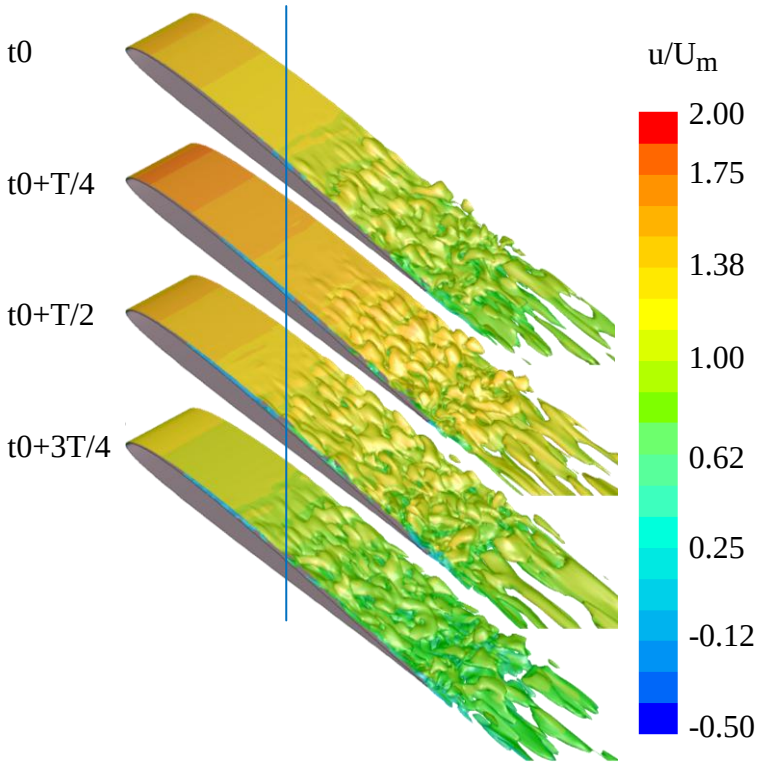

Figure 51: Instantaneous iso-surfaces of z-vorticity ($\omega_z C/U_m = -10$) during one cycle for case U5 with $k = \pi/8$ and $\sigma = 0.183$.

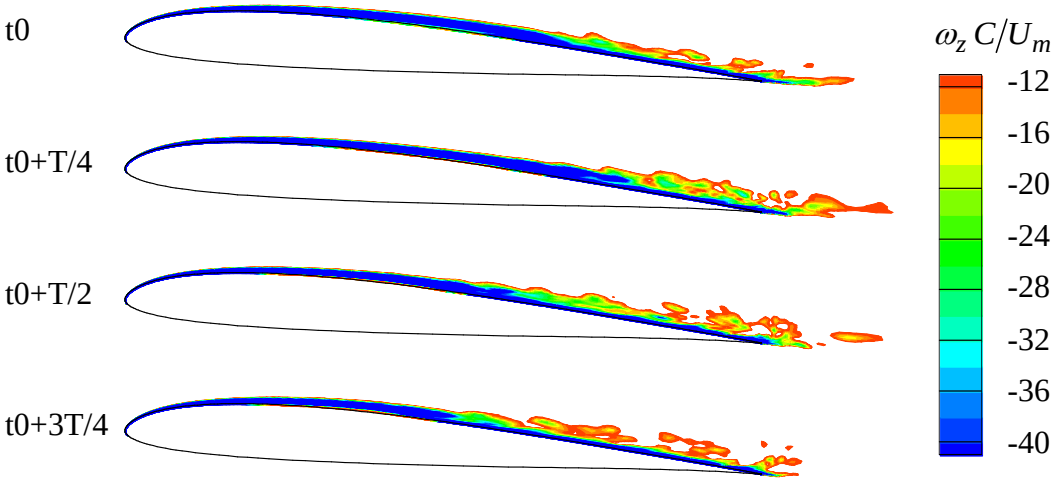

Figure 52: Instantaneous contours of spanwise-averaged z-vorticity ($\omega_z C/U_m$) during one cycle for case U5 with $k = \pi/8$ and $\sigma = 0.183$.

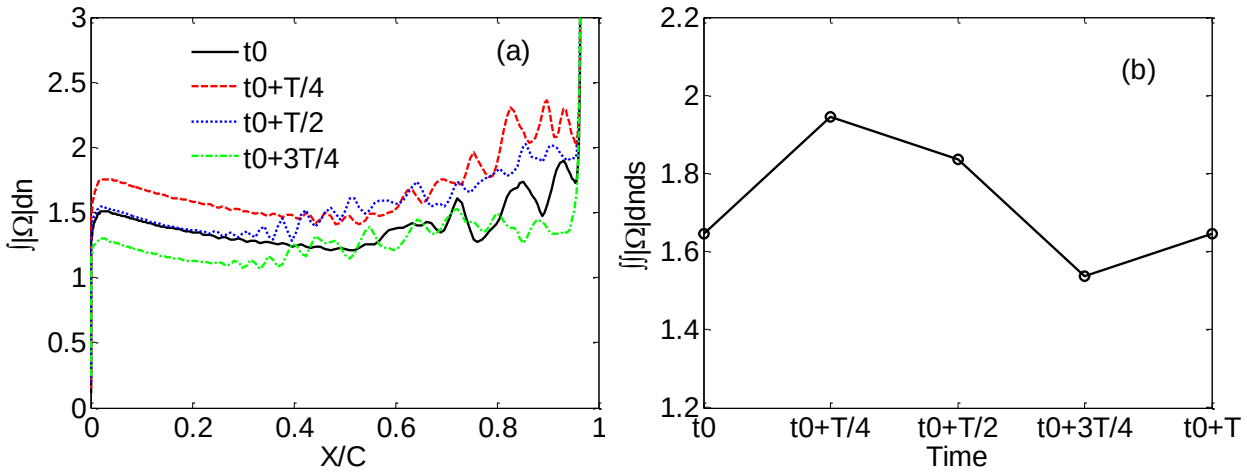

Figure 53: Integrals of spanwise-averaged vorticity magnitude |Ω| for case U5 with $k = \pi/8$ and $\sigma = 0.183$. (a) Integrated along n axis; (b) integrated along n and then s axes.

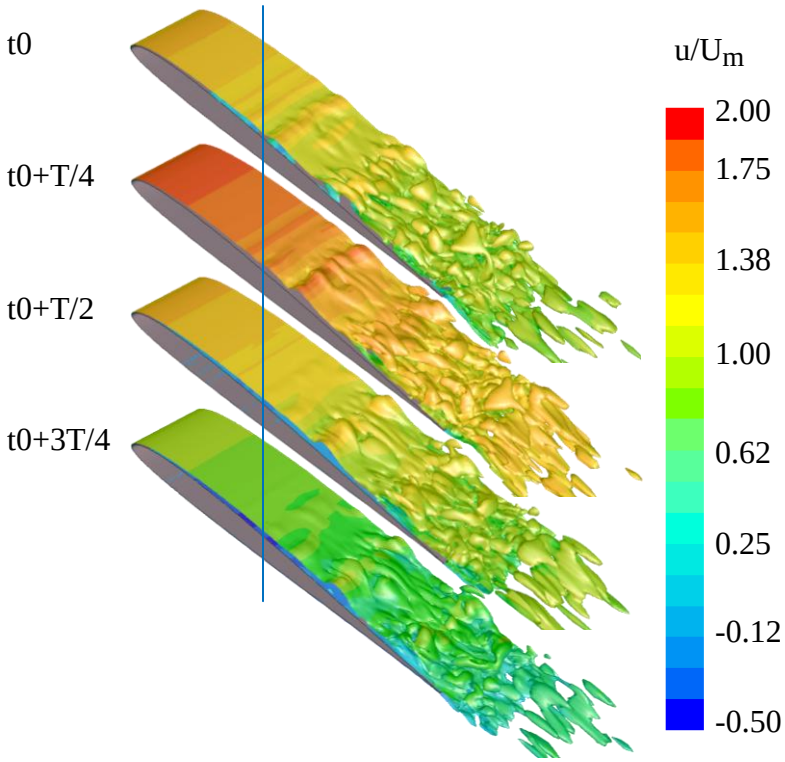

Figure 54: Instantaneous iso-surfaces of z-vorticity ($\omega_z C/U_m = -10$) during one cycle for case U6 with $k = 2\pi$ and $\sigma = 0.366$.

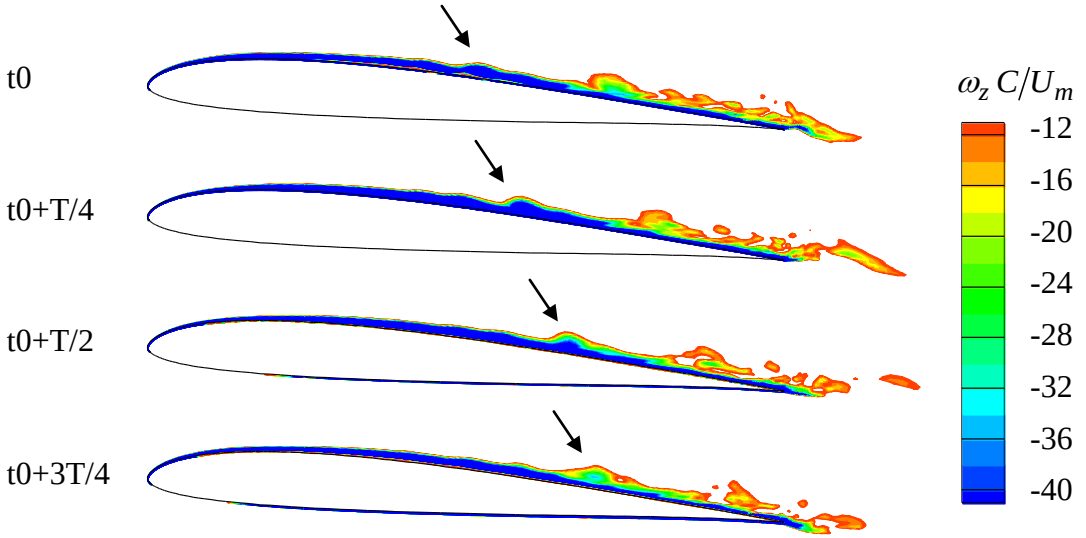

Figure 55: Instantaneous contours of spanwise-averaged z-vorticity ($\omega_z C/U_m$) during one cycle for case U6 with $k = 2\pi$ and $\sigma = 0.366$.

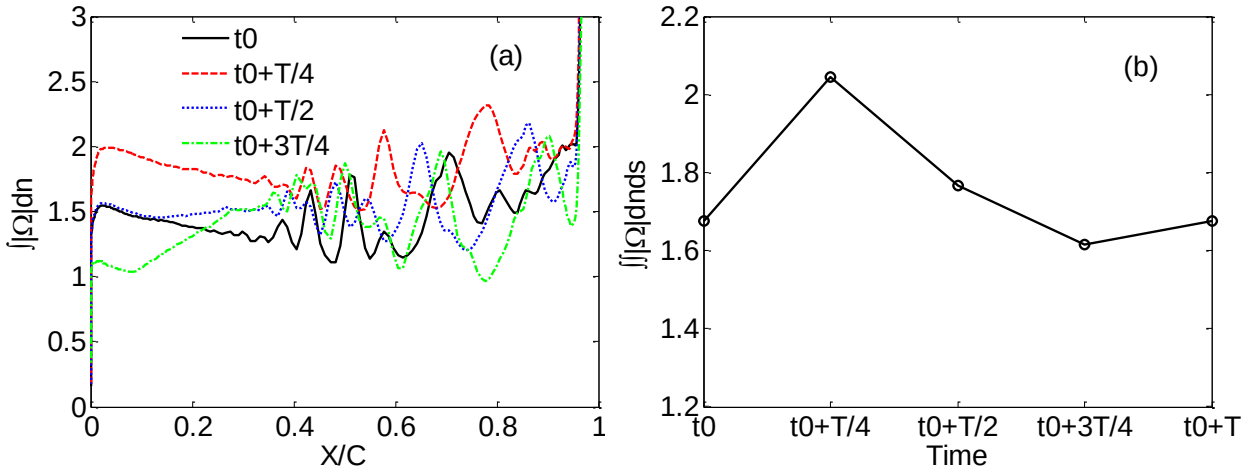

Figure 56: Integrals of spanwise-averaged vorticity magnitude |Ω| for case U6 with $k = 2\pi$ and $\sigma = 0.366$. (a) Integrated along n axis; (b) integrated along n and then s axes.

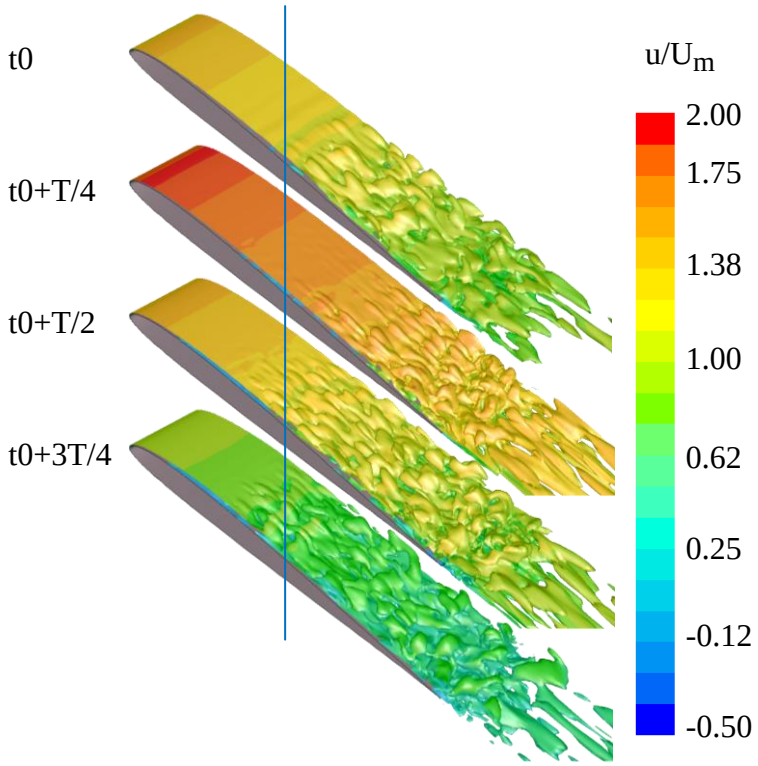

Figure 57: Instantaneous iso-surfaces of z-vorticity ($\omega_z C/U_m = -10$) during one cycle for case U10 with $k = \pi/8$ and $\sigma = 0.366$.

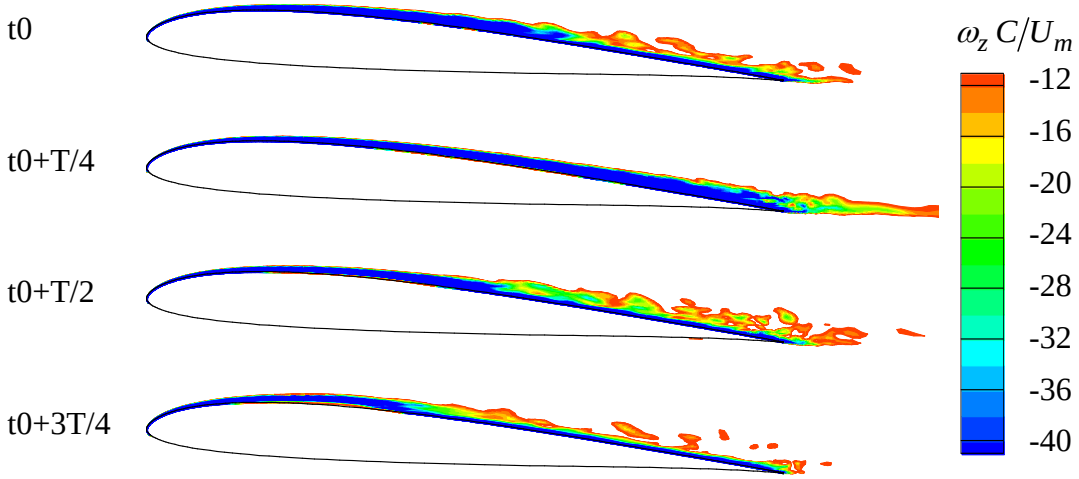

Figure 58: Instantaneous contours of spanwise-averaged z-vorticity ($\omega_z C/U_m$) during one cycle for case U10 with $k = \pi/8$ and $\sigma = 0.366$.

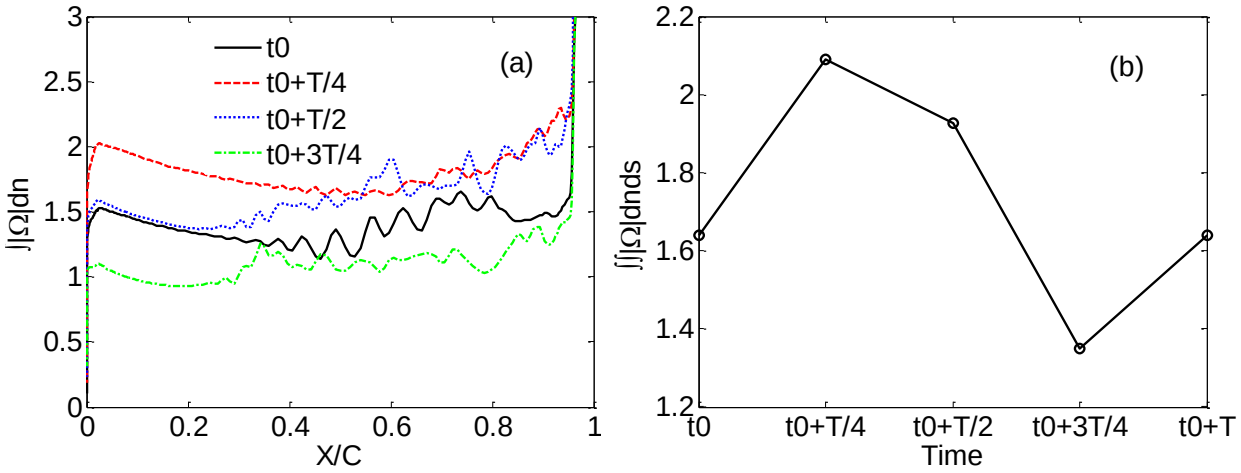

Figure 59: Integrals of spanwise-averaged vorticity magnitude |Ω| for case U10 with $k = \pi/8$ and $\sigma = 0.366$. (a) Integrated along n axis; (b) integrated along n and then s axes.

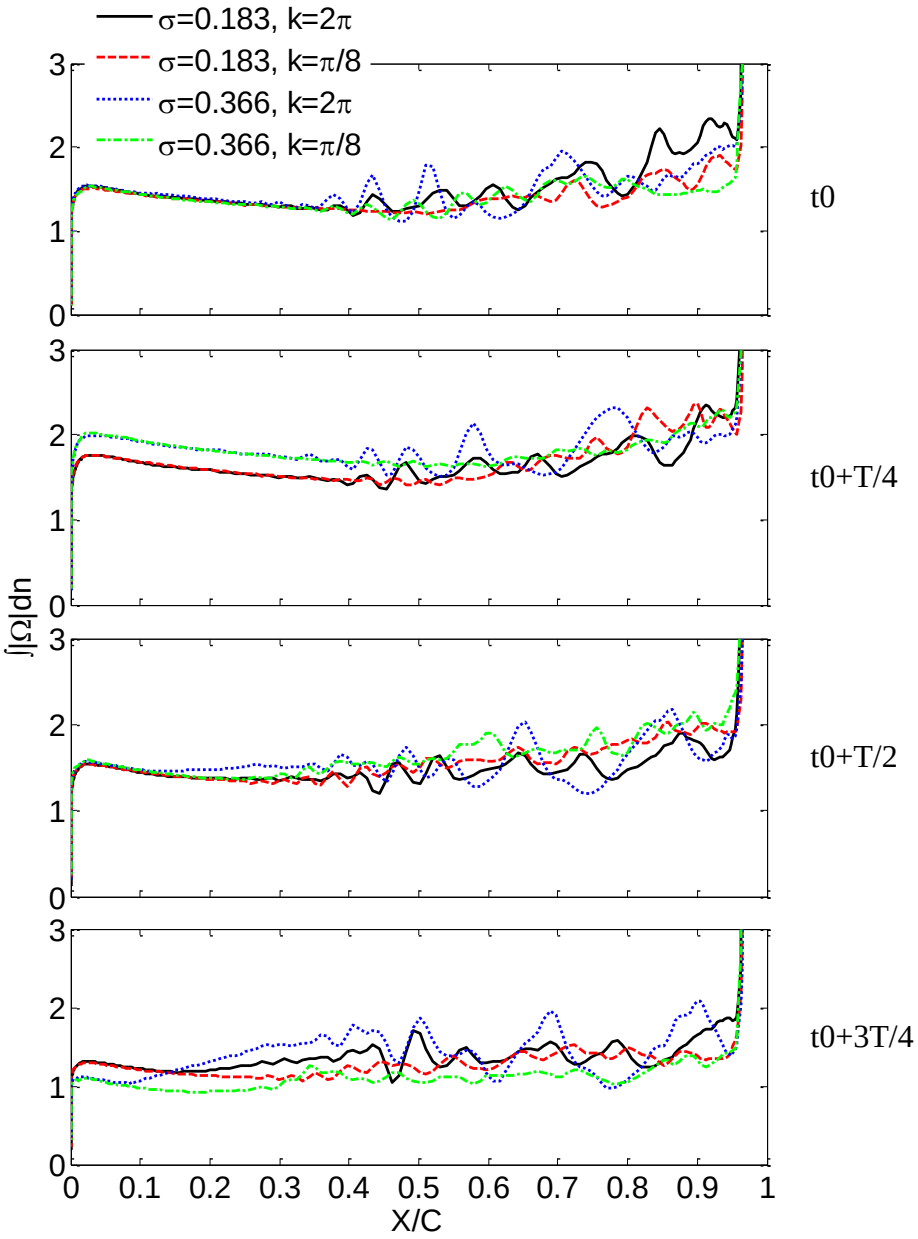

Figure 60: Integral of spanwise-averaged vorticity magnitude |Ω| along n axis for cases U1, U5, U6, and U10.

5.1.3 Velocity fluctuations

The effect of freestream velocity unsteadiness on the velocity fluctuations over the airfoil is studied in this section by comparing the root mean square (RMS) values of three velocity components and turbulent kinetic energy (TKE) of steady and unsteady cases.

Velocity RMS is calculated for unsteady case U6 with σ=0.366 and k=2π, using LES data for five freestream cycles. This case is chosen due to its short period and large amplitude of oscillation in freestream velocity magnitude. The larger amplitude of σ=0.366 is chosen because it is expected that larger amplitude of oscillation in freestream velocity causes larger variation in velocity RMS. During each cycle, the velocity data are recorded at four different times or phases. The 3D computational domain has 101 grids in the spanwise (z) direction. Therefore, for a given point on the x-y plane and five available cycles, there are 505 (=101×5) instantaneous velocity samples for spanwise and phase averaging, from which the velocity RMS and the turbulence kinetic energy (TKE) are calculated. The velocity RMS of the steady freestream flow with Re=60,000 and AoA=4° is also calculated for comparison, using velocity data for five flow residence times. Figure 61 shows the integrated values of the RMS of three velocity components for the steady case. These integrated values are easier to interpret and are obtained by integrating the velocity RMS and TKE values along the n or n and s directions (Figure 44). These integrated values are represented by $\int (RMS) dn$, $\int\int (RMS) dnds$, and $\int\int (TKE) dnds$. The integrated values of RMS of u, v, w, and TKE along airfoil surface normal and tangent directions (n and s), i.e. $\int\int (RMS) dnds$, $\int\int (TKE) dnds$, are 0.0237, 0.0209, 0.0024 and 0.0004, respectively for the steady case. Figure 61 shows that, for the steady freestream flow, $\int (RMS) dn$ increases along the airfoil surface and peaks around the trailing edge.

The integrated values of velocity RMS and TKE for the unsteady case U6 are plotted in Figures 62-64. Similar to steady case, Figure 62 shows that the integrated RMS values of all three velocity components are essentially zero at X/C=0, but gradually increases till trailing edge, where it suddenly increases. Figures 62-63 show that the RMS of velocity fluctuations changes only slightly with the phase and are similar to those shown in Figure 61 for steady flow. Figure

64 shows that the TKE values are slightly higher at time t0+T/4 compared to other times or phases, suggesting that higher freestream velocity induces stronger "turbulence" and higher velocity fluctuations. Also similar to steady flow, it is shown that the fluctuations or RMS of x- and y-velocities are comparable, but much bigger than that of z-velocity. Naturally, the TKE is dominated by the x- and y-velocity fluctuations and behaves similar to RMS of these velocity components.

By comparing the integrals of velocity RMS and TKE along n and s axes, i.e. $\int\int(RMS)dnds$ and $\int\int(TKE)dnds$ in Figures 63 and 64, it is found that the x- and y-velocity fluctuations of the unsteady case U6 with k = 2π and σ = 0.366 are generally lower than those of the steady freestream flow while the z-velocity fluctuations are close for these two flows. This is also shown in Figure 65 for $\int(RMS)dn$. It seems that the oscillation in freestream velocity magnitude suppresses the fluctuations of the x- and y-velocities but does not noticeably affect the spanwise velocity fluctuations.

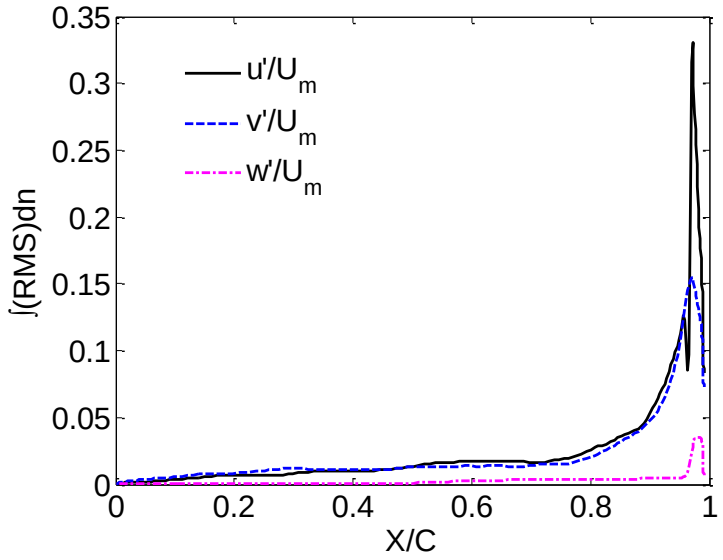

Figure 61: Integrated values of velocity RMS along n axis for the flow with steady freestream, Re=60,000 and AoA=4°.

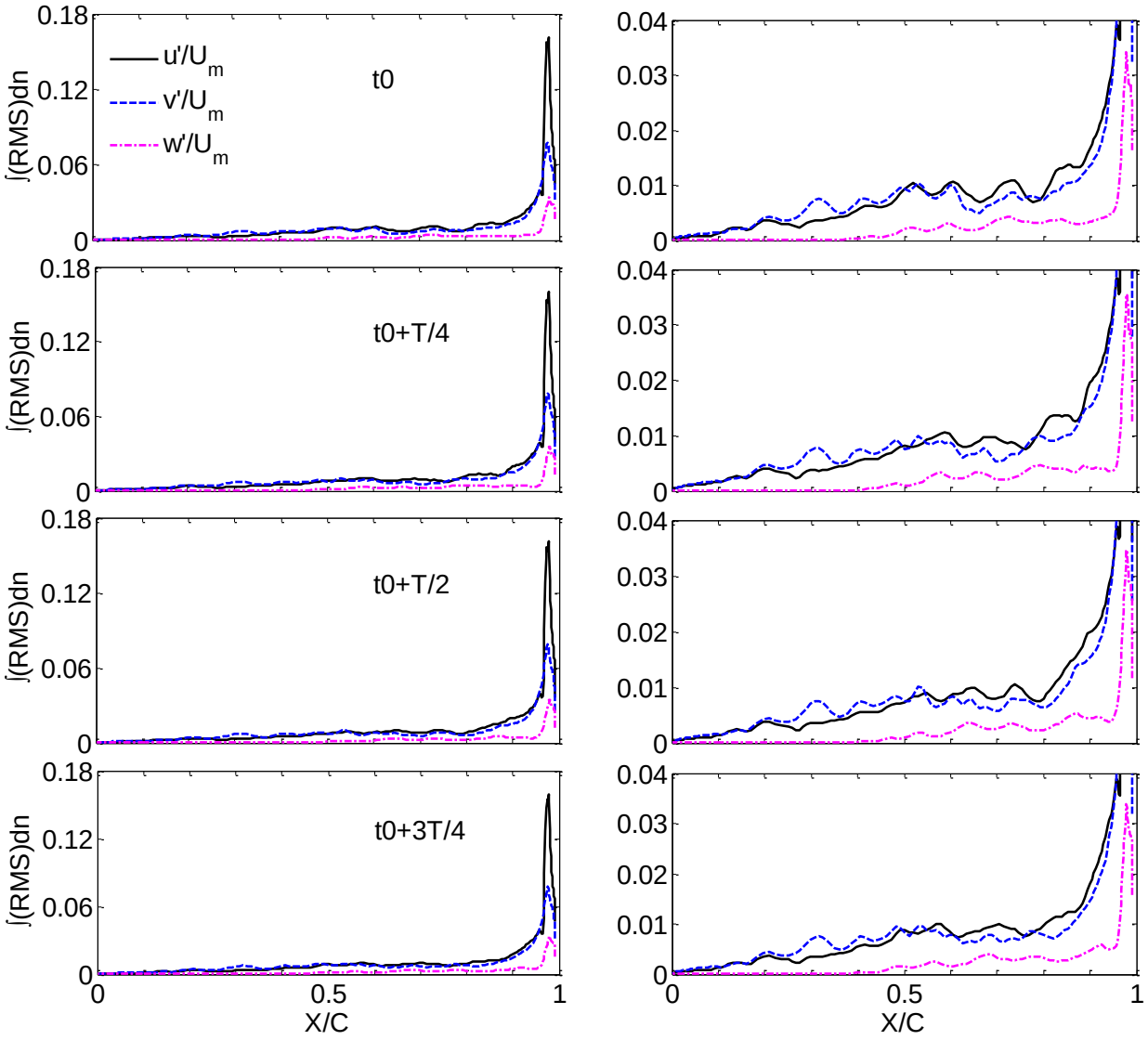

Figure 62: Integrated values of velocity RMS along n axis for case U6 with $k = 2\pi$ and $\sigma = 0.366$.

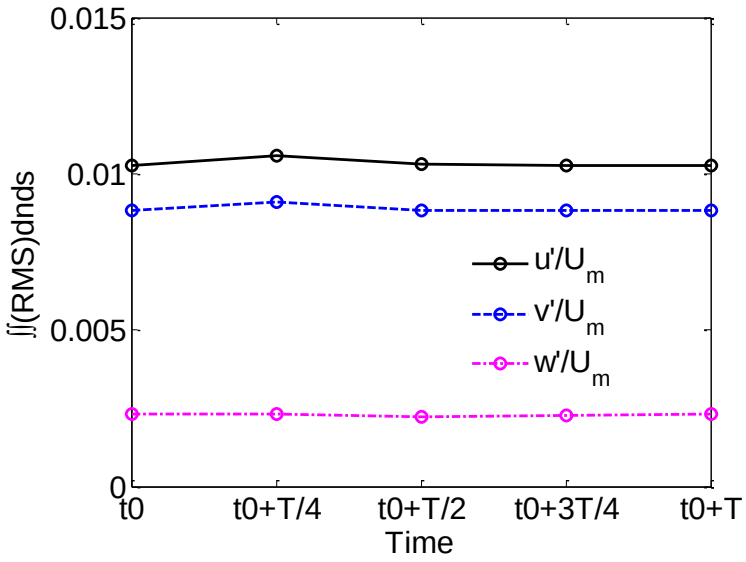

Figure 63: Integrated values of velocity RMS along n and s axes for case U6 with $k = 2\pi$ and $\sigma = 0.366$.

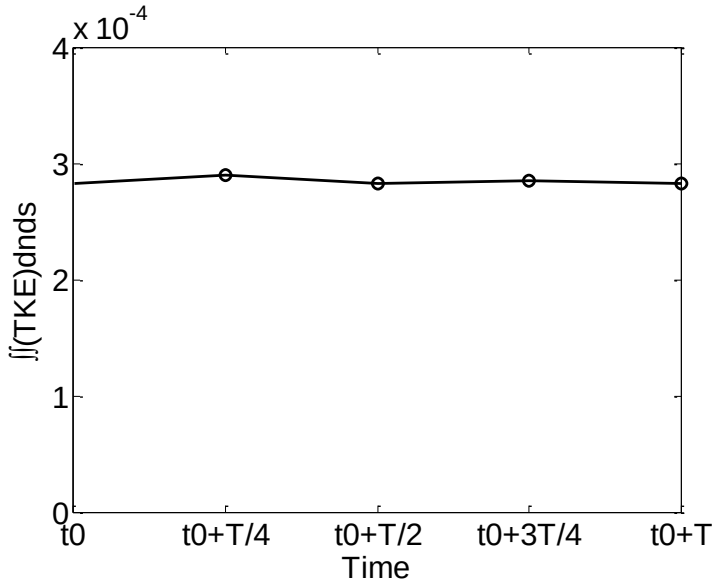

Figure 64: Integrated values of turbulence kinetic energy (TKE) along n and s axes for case U6 with $k = 2\pi$ and $\sigma = 0.366$.

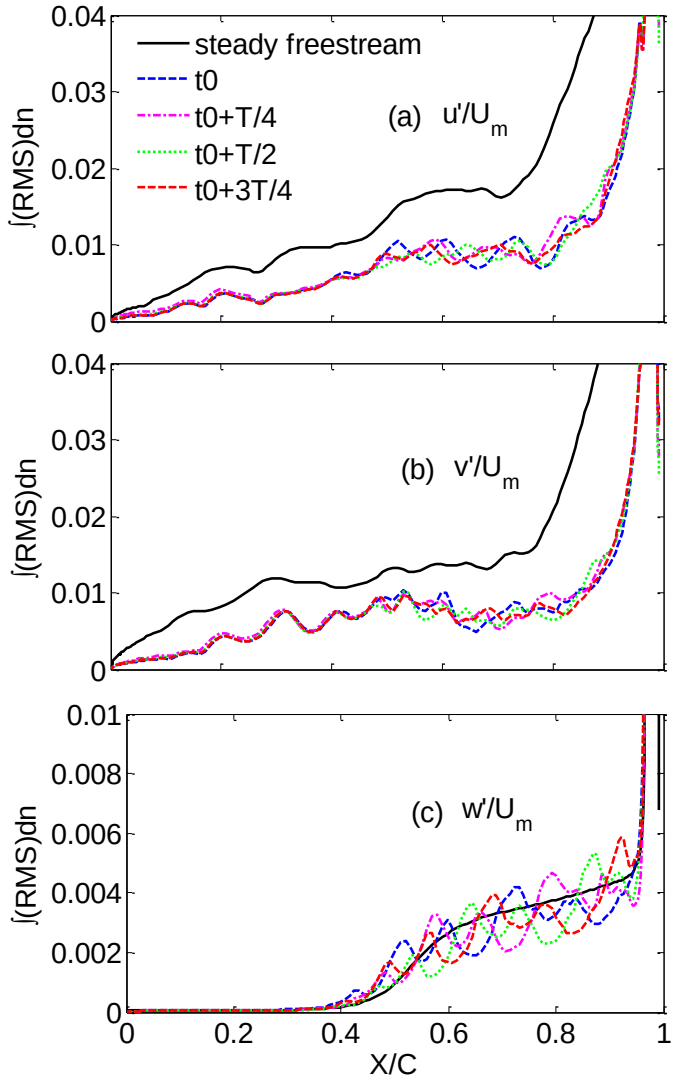

Figure 65: Comparison of integrated values of velocity RMS along n axis between case U6 with $k = 2\pi$ and $\sigma = 0.366$ and the flow with steady freestream with Re=60,000 and AoA=4°. (a) u RMS; (b) v RMS; (c) w RMS.

5.1.4 Boundary layer separation and reattachment

Effect of oscillating freestream velocity on the flow over airfoil is further examined in this section by comparing the separation and reattachment points for various unsteady and steady cases. Similar to the separation and reattachment points obtained from the mean flow field, the instantaneous separation point can be calculated to be the location where the instantaneous skin friction coefficient C_F first goes from positive to negative, and the instantaneous reattachment

point is defined as the location where C_F last goes from negative to positive. The mean C_F is calculated from the time- and spanwise-averaged velocity, and the instantaneous C_F is based on the instantaneous spanwise-averaged velocity. For the steady freestream flow, Figure 66 clearly shows that the instantaneous C_F profiles at different times closely follow the mean profile. The instantaneous profiles are identical to the mean profile before the separation point, and consequently, the instantaneous separation and reattachment points oscillate around the mean values with small amplitude. The small oscillations in the C_F are due to small perturbations in the vortical flow over the airfoil and are not due to any freestream turbulence in the flow which is negligible. When the freestream velocity magnitude oscillates at low reduced frequency of $\pi/8$ (Figure 67), the instantaneous separation and reattachment points fluctuate with amplitudes larger than those of the steady freestream flow. At higher reduced frequency of 2π (Figure 68), the four instantaneous C_F profiles deviate further from the mean profile, so much so that the flow at time t0 and t0+T/4 becomes almost fully attached. Compared to Figure 68, Figure 69 shows that higher freestream velocity amplitude causes even wider oscillation in the skin friction coefficient profile. The C_F profile at t0+T/4 in Figure 69 suggests that the flow is fully attached, while the C_F profiles at t0+T/2 and t0+3T/4 show the flow, after early separation, to reattach as late as the trailing edge. Figures 67-69 generally show that the separation will be delayed or completely eliminated as freestream velocity is accelerating, and it will happen earlier and closer to the leading edge when the freestream velocity is decelerating. This is related to the freestream pressure gradient as Equation (40) suggests. As the freestream velocity is accelerating, the strong negative pressure gradient in the freestream flow will alleviate or completely eliminate the positive pressure gradient induced by the airfoil curvature which causes the separation.

The mean separation and reattachment points computed based on the mean C_F curves for steady and unsteady cases are listed in Table 7. The mean separation points for all ten unsteady cases are shown to be quite similar, while the mean reattachment points vary between 0.35 and 0.53 without a clear trend. Compared to the flow with steady freestream velocity, each of unsteady cases has a delayed mean separation point and an earlier mean reattachment point closer to the airfoil leading edge.

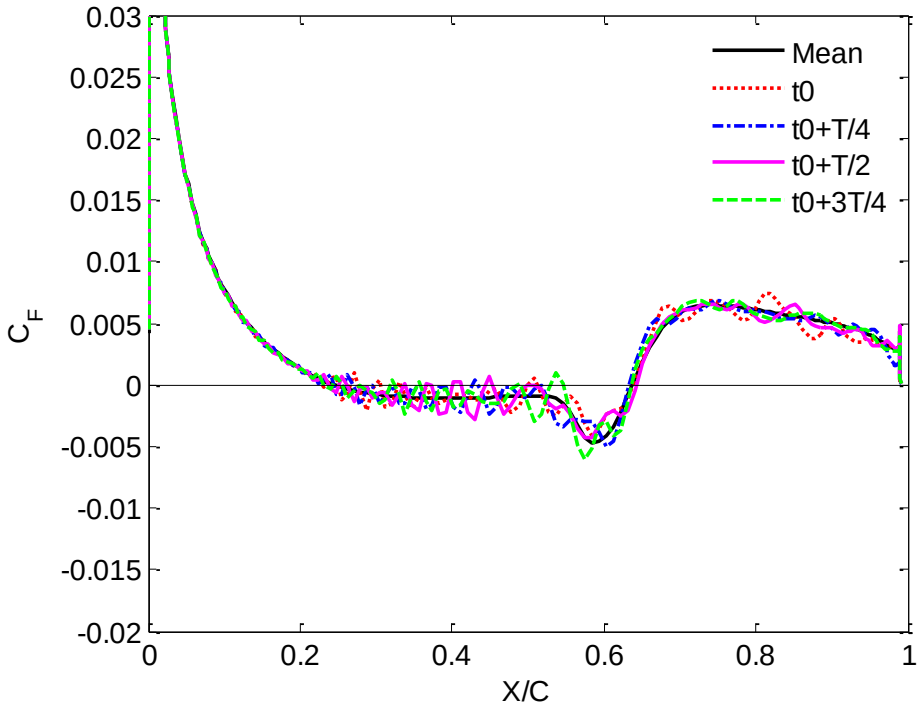

Figure 66: Time-averaged and instantaneous skin friction coefficient on the airfoil upper surface for the flow with steady freestream, Re=60,000 and AoA=4 °.

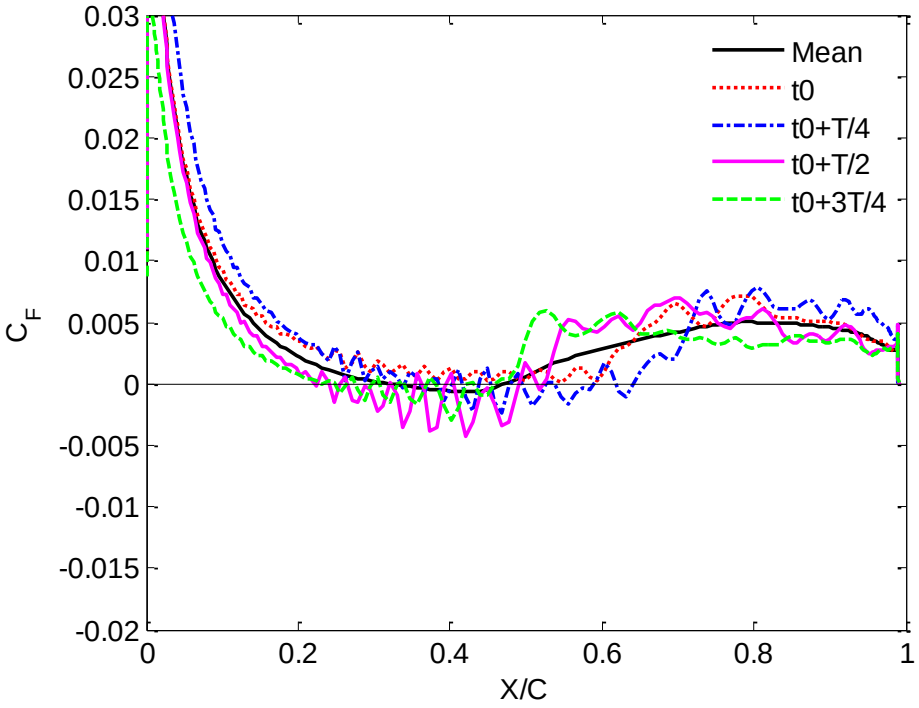

Figure 67: Time-averaged and instantaneous skin friction coefficient on the airfoil upper surface for case U5 with $k = \pi/8$ and $\sigma = 0.183$.

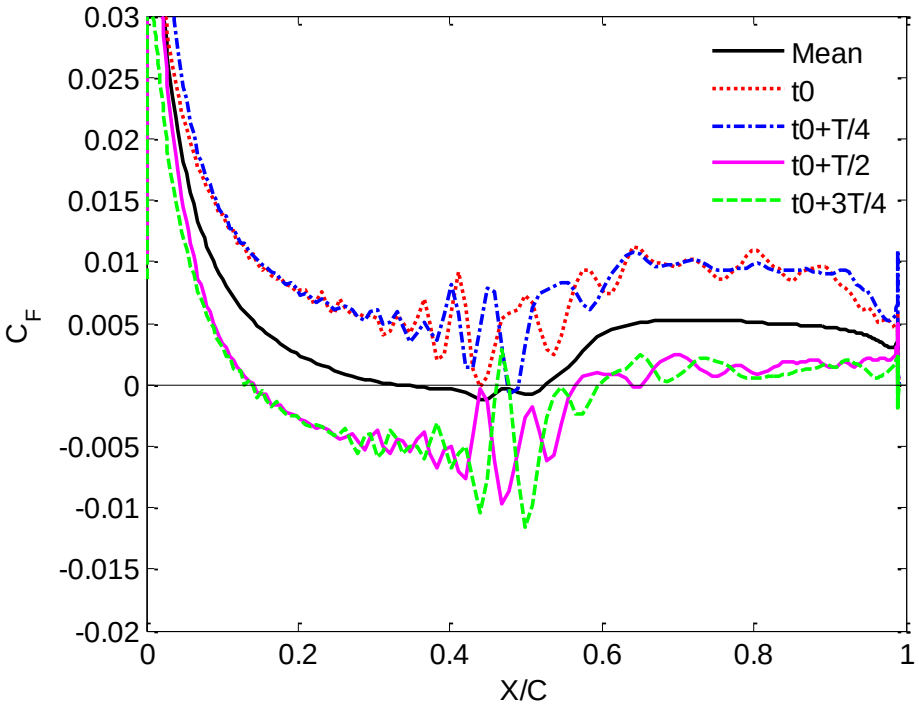

Figure 68: Time-averaged and instantaneous skin friction coefficient on the airfoil upper surface for case U1 with $k = 2\pi$ and $\sigma = 0.183$.

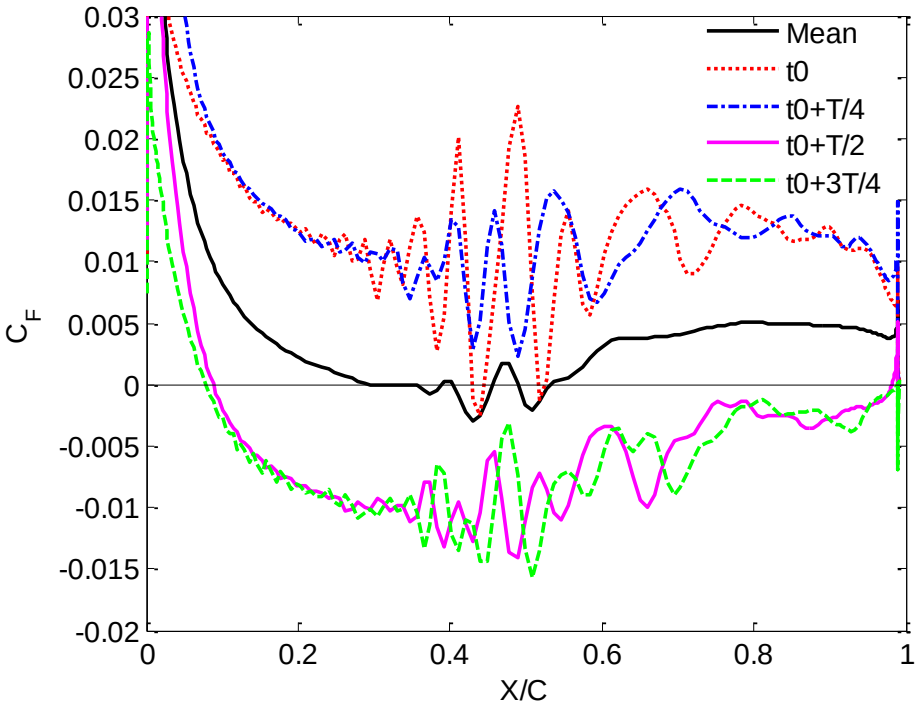

Figure 69: Time-averaged and instantaneous skin friction coefficient on the airfoil upper surface for case U6 with $k = 2\pi$ and $\sigma = 0.366$.

5.2 Flows with Oscillating Angle of Attack (AoA)

In this section we discuss the results for a set of simulations with variable AoA. The airfoil is assumed to be fixed but the direction of freestream flow is periodically changed according to Equation (41) below. The freestream velocity has a constant magnitude of U_m with a mean Reynolds number of 60,000. The mean AoA is fixed at $\alpha_m = 4°$, while the amplitude and reduced frequency, α_f and k, are changed within a range similar to that used for velocity magnitude oscillations in Section 5.1. The ten cases with unsteady AoA considered in this section are listed in Table 8. The range of variation in the reduced frequency, k, is chosen again to be the same as that in Table 7. The amplitude of AoA oscillations is $4°$ for cases A1 through A5 and $8°$ for cases A6 through A10.

$$\begin{cases} \alpha(t) = \alpha_m + \alpha_f \sin(\omega t) \\ U(t) = U_m \cos(\alpha - \alpha_m) \\ V(t) = U_m \sin(\alpha - \alpha_m) \\ W = 0 \end{cases} \tag{41}$$

Case	α_f (deg.)	k	C_L Mean	C_L Amplitude	C_D Mean	C_D Amplitude	X_S/C Mean	X_R/C Mean
Steady mean freestream	0	-	0.59	2.6×10^{-3} (standard deviation)	0.020	2.5×10^{-4} (standard deviation)	0.25	0.64
A1	4	2π	0.57	2.30	0.018	0.158	-	-
A2	4	π	0.56	1.13	0.017	0.080	0.35	0.42
A3	4	$\pi/2$	0.56	0.57	0.017	0.044	0.33	0.46
A4	4	$\pi/4$	0.56	0.31	0.016	0.030	0.30	0.42
A5	4	$\pi/8$	0.56	0.25	0.015	0.024	0.29	0.37
A6	8	2π	0.60	4.62	0.011	0.322	-	-
A7	8	π	0.58	2.29	0.008	0.160	-	-
A8	8	$\pi/2$	0.57	1.15	0.007	0.089	-	-
A9	8	$\pi/4$	0.56	0.62	0.006	0.062	-	-
A10	8	$\pi/8$	0.56	0.50	0.003	0.051	-	-

Table 8: Time-averaged data for cases with oscillating AoA.

Lift coefficient, drag coefficient, pressure coefficient, and skin friction coefficient are defined in Section 3.5. As the AoA oscillates in these flows, it should be noted that the lift and drag forces can be computed by decomposing the aerodynamic force vector along the coordinate directions or axes constructed based on fixed mean AoA of α_m or they can be obtained by decomposing the force along coordinate directions constructed based on instantaneous AoA or $\alpha(t)$ (Figure 13). Both of these will be considered below.

5.2.1 Aerodynamic forces

Figures 70-73 show the variations of lift and drag coefficients (C_L and C_D) for one cycle after the flows have fully developed under the periodically variable freestream flow AoA condition. Lift and drag forces and C_L and C_D in these figures are calculated over the fixed (mean) flow axial and normal directions. Similar to what was observed in flows with oscillating freestream velocity magnitude, C_L and C_D oscillate in time with the freestream frequency, and C_L and C_D profiles are generally "sinusoidal-like".

The lift and drag forces can also be computed by decomposing the aerodynamic force vector along the coordinate directions constructed based on instantaneous AoA or $\alpha(t)$. The new lift and drag coefficients, denoted as C_L^*, C_D^*, can be calculated by a simple conversion from C_L and C_D as shown in Equation (42), and the results for cases A6-10 are shown in Figures 74 and 75. Clearly, C_L^* is similar to C_L, but C_D^* is significantly different from C_D, simply because the conversion affects the smaller drag coefficient much more than it does the lift coefficient. As shown in Figure 75, C_D^* profiles are no longer "sinusoidal-like".

$$\begin{cases} C_L^* = C_L \cos\left(\alpha(t) - \alpha_m\right) - C_D \sin\left(\alpha(t) - \alpha_m\right) \\ C_D^* = C_D \cos\left(\alpha(t) - \alpha_m\right) + C_L \sin\left(\alpha(t) - \alpha_m\right) \end{cases} \tag{42}$$

The mean and amplitude of C_L and C_D are listed in Table 8 along with the data for the steady freestream flow with Re=60,000 and AoA=4°. It is clear that reduced frequency and amplitude of AoA oscillation have only slight effect on the mean lift coefficient which stays close to its steady freestream flow value of 0.59. However, in all cases, the mean drag coefficient is lower than its steady freestream flow value of 0.020. The reduction in drag of an airfoil when the freestream direction is oscillating is referred to as the Katzmayr effect [33]. Toussaint et al.

[34] verified the existence of Katzmayr effect in a set of wind tunnel experiments with oscillating freestream flow direction with respect to an airfoil, induced by pitching blades. Based on these experiments, Ober [55] provided an explanation for the Katzmayr effect, showing that, on average, the rotated lift vector has a bigger component in negative drag (thrust) than in positive drag. In the experiments by Toussaint et al., the reduced frequencies are lower than 0.5, and effects of reduced frequency and amplitude of the AoA oscillation cannot be separated because these two parameters could not be changed independently in the experiments. The LES results here confirm the Katzmayr effect to a much bigger range of reduced frequency and also show that the drag reduction is increased at lower reduced frequency and higher amplitude of AoA oscillation. For example, C_D drops as much as 83% from case A1 to case A10 because α_f is doubled and k is reduced to 1/16 of its value in case A1. The effect of AoA oscillation amplitude on drag reduction may be examined by considering case A10. In case A10, the amplitude of oscillation in AoA is 8°, allowing the flow AoA to vary between -4° and 12° during one cycle. For this case, the time interval with negative AoA is 1/3 of the cycle. At a negative AoA, the freestream velocity has a component in the negative y-direction (Figure 13), resulting in a thrust on the airfoil. By comparing C_D profiles of cases A5 (Figure 71) and A10 (Figure 73), it is clear that the airfoil spends a bigger portion of each period of C_D oscillations with negative drag (thrust) when the freestream AoA amplitude is higher.

The amplitudes of oscillations in C_L and C_D for the unsteady AoA cases are listed in Table 8 and are also plotted in Figure 76 against the reduced frequency and freestream AoA amplitude. Both C_L and C_D amplitudes seem to increase linearly with the freestream AoA amplitude or α_f, meaning that if AoA amplitude is doubled while keeping the reduced frequency the same, C_L and C_D will also double in amplitudes. C_L and C_D amplitudes seem to be almost linear to reduced

frequency too when the reduced frequency is higher than $\pi/2$. At low reduced frequencies, C_L and C_D amplitudes change much less with the reduced frequency. Understandably, the flow varies more slowly and becomes quasi-steady as the reduced frequency gets close to zero. In a quasi-steady flow, enough time is given to the flow to adjust to changes in AoA, and C_L and C_D values become close to those of the corresponding steady freestream flow.

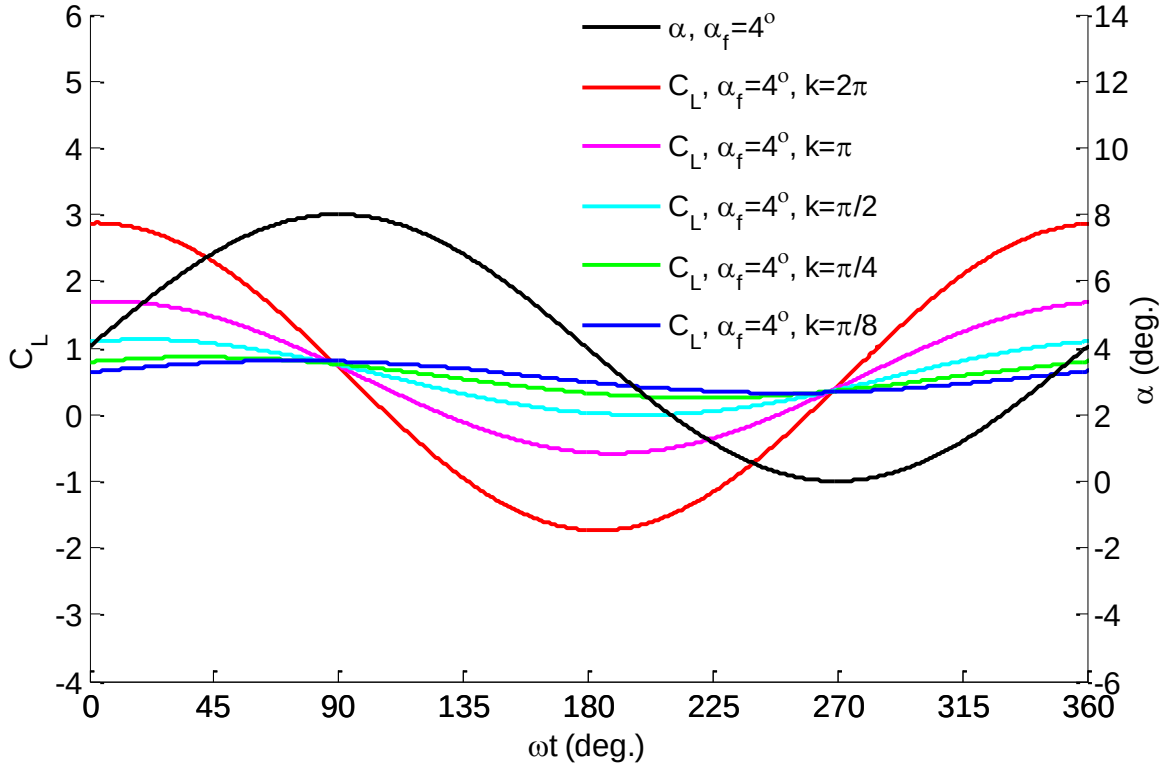

Figure 70: Time variations of C_L for flows with oscillating AoA, cases A1-5.

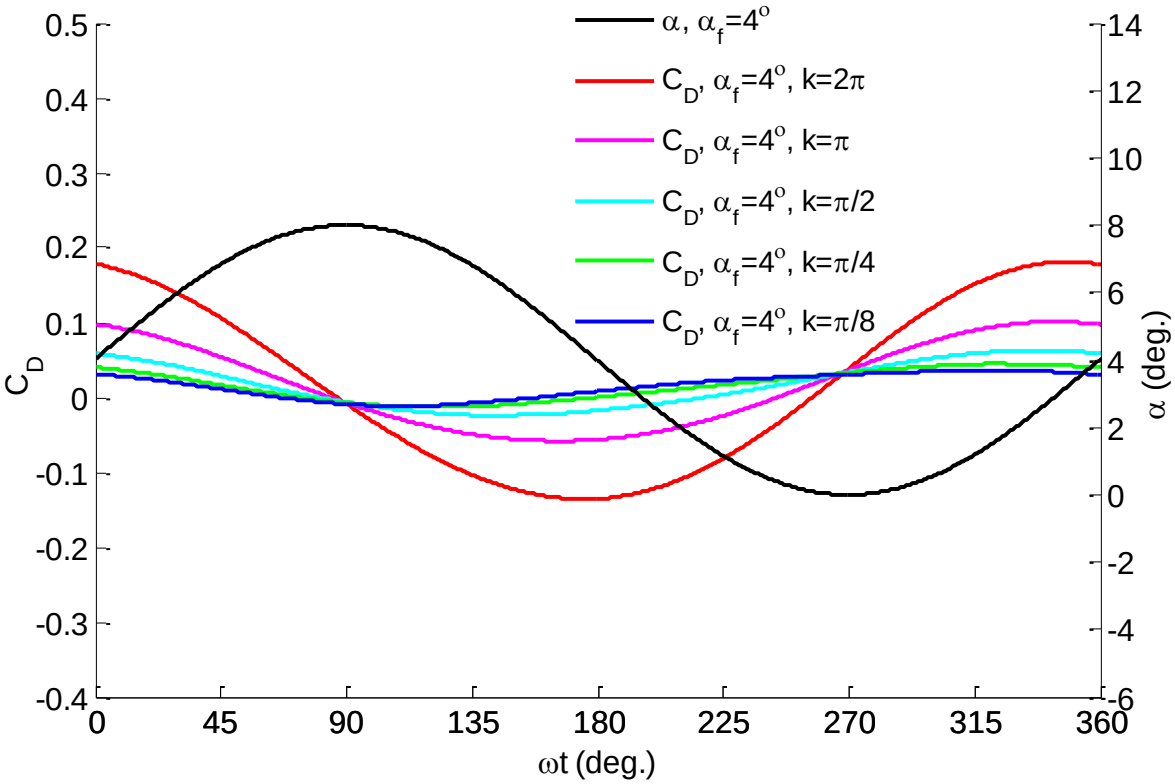

Figure 71: Time variations of C_D for flows with oscillating AoA, cases A1-5.

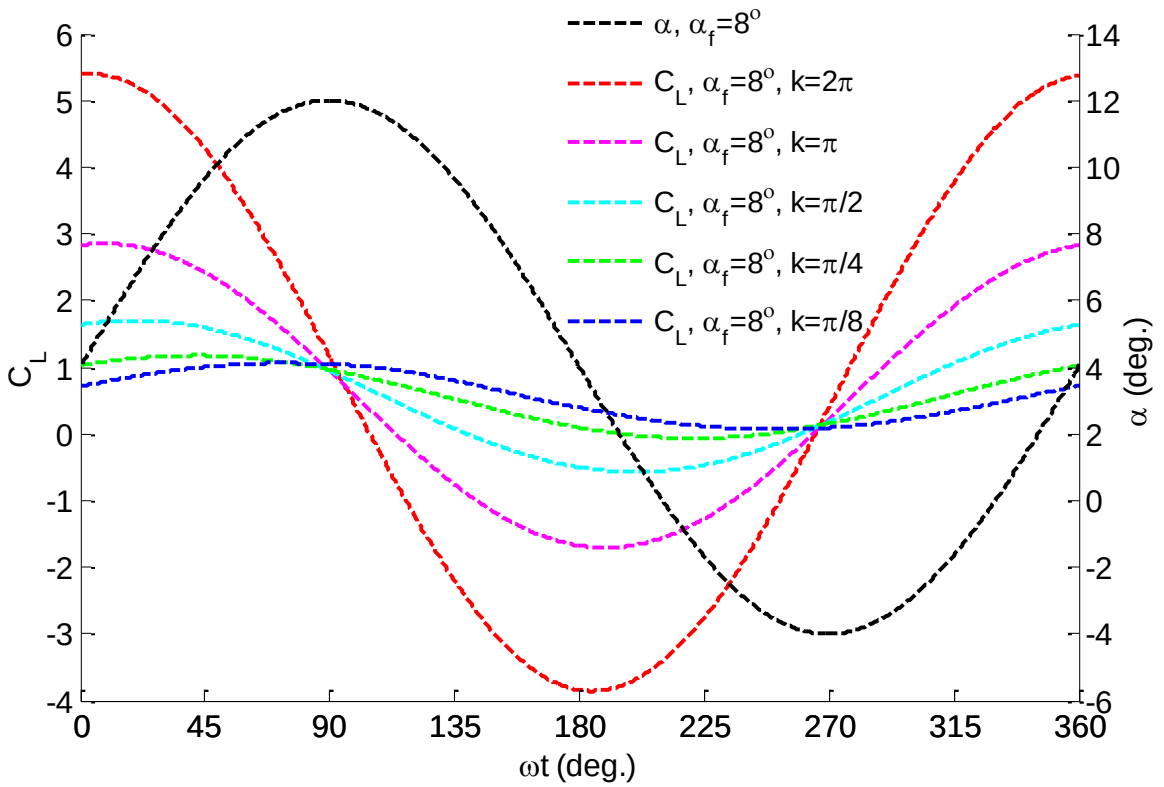

Figure 72: Time variations of C_L for flows with oscillating AoA, cases A6-10.

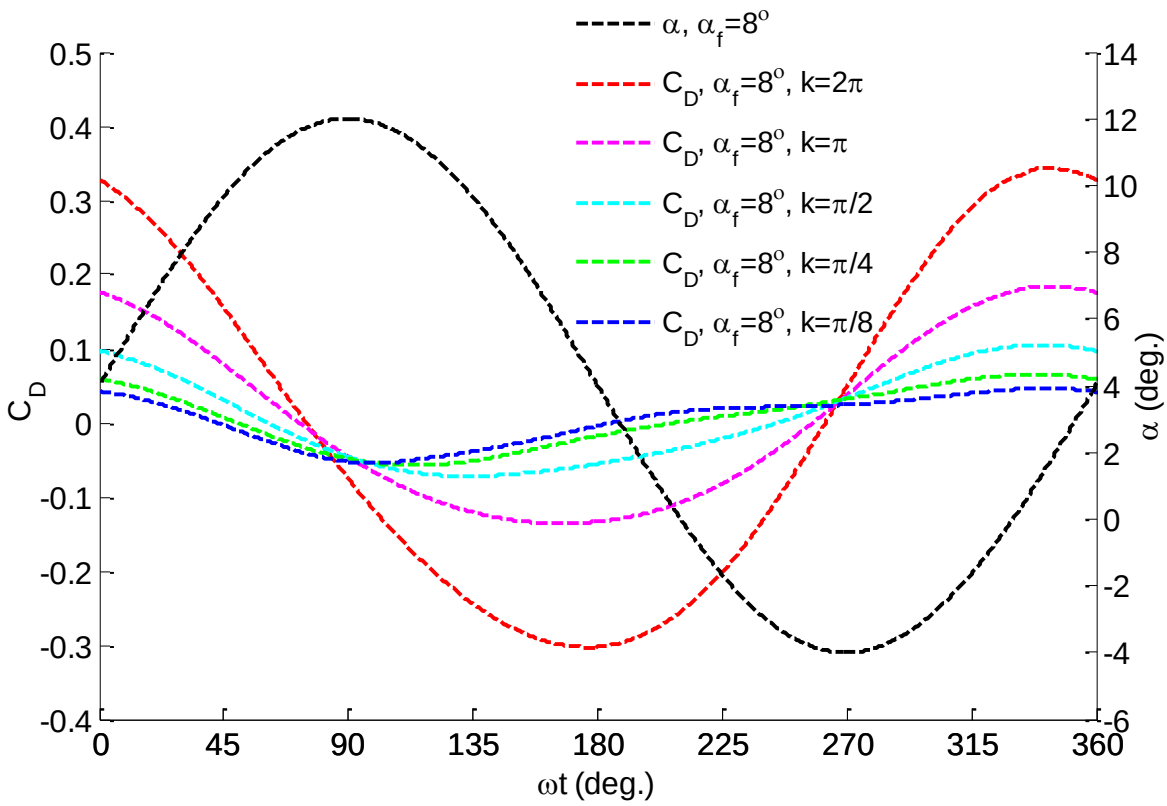

Figure 73: Time variations of C_D for flows with oscillating AoA, cases A6-10.

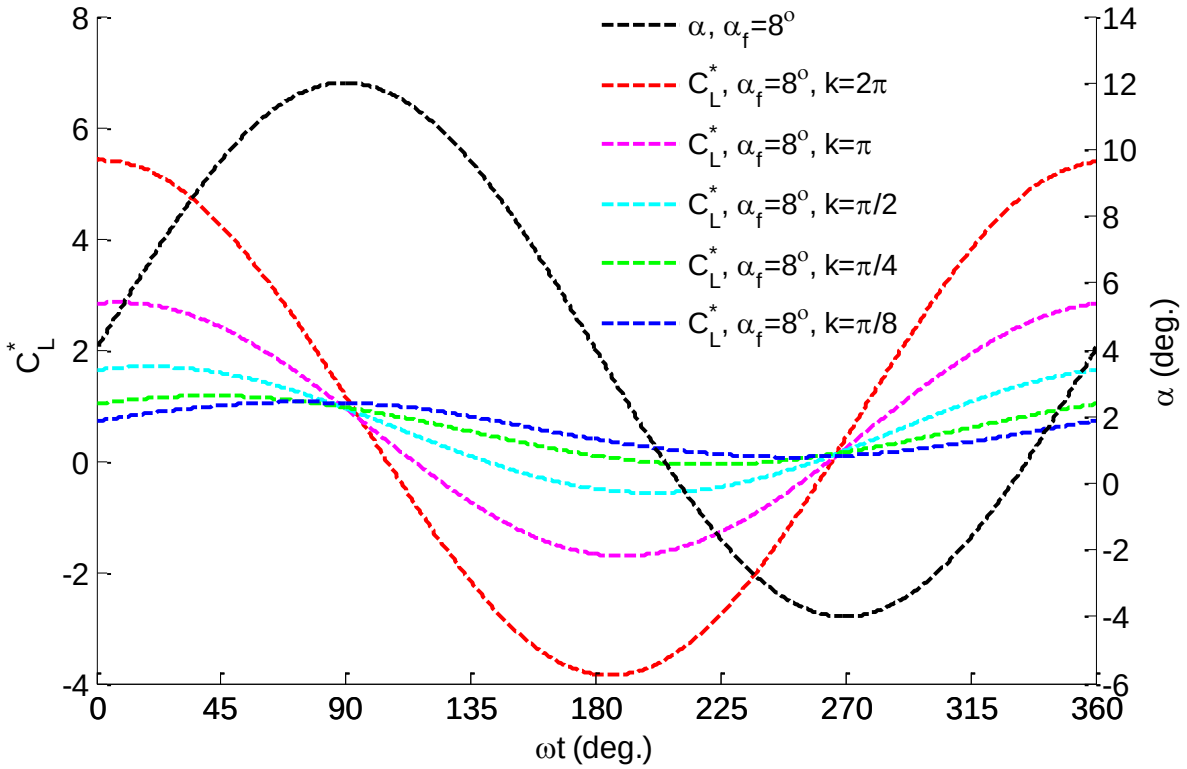

Figure 74: Time variations of C_L^* for flows with oscillating AoA, cases A6-10.

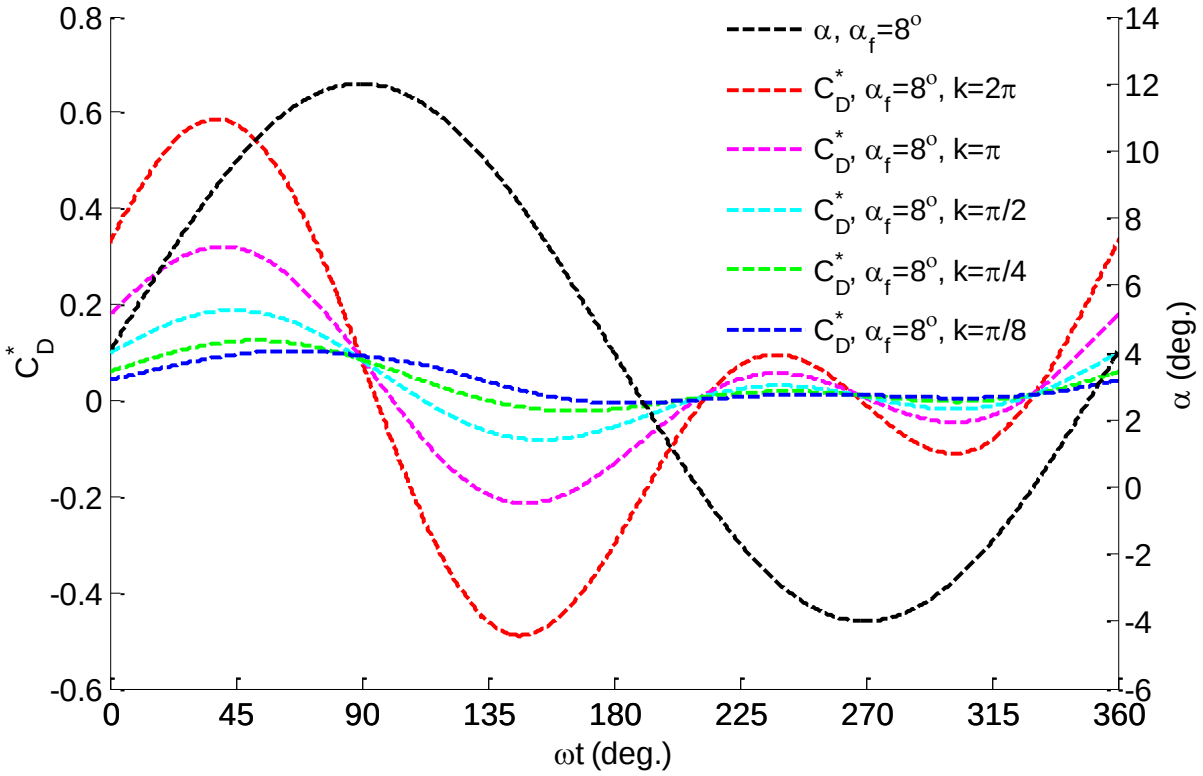

Figure 75: Time variations of C_D^* for flows with oscillating AoA, cases A6-10.

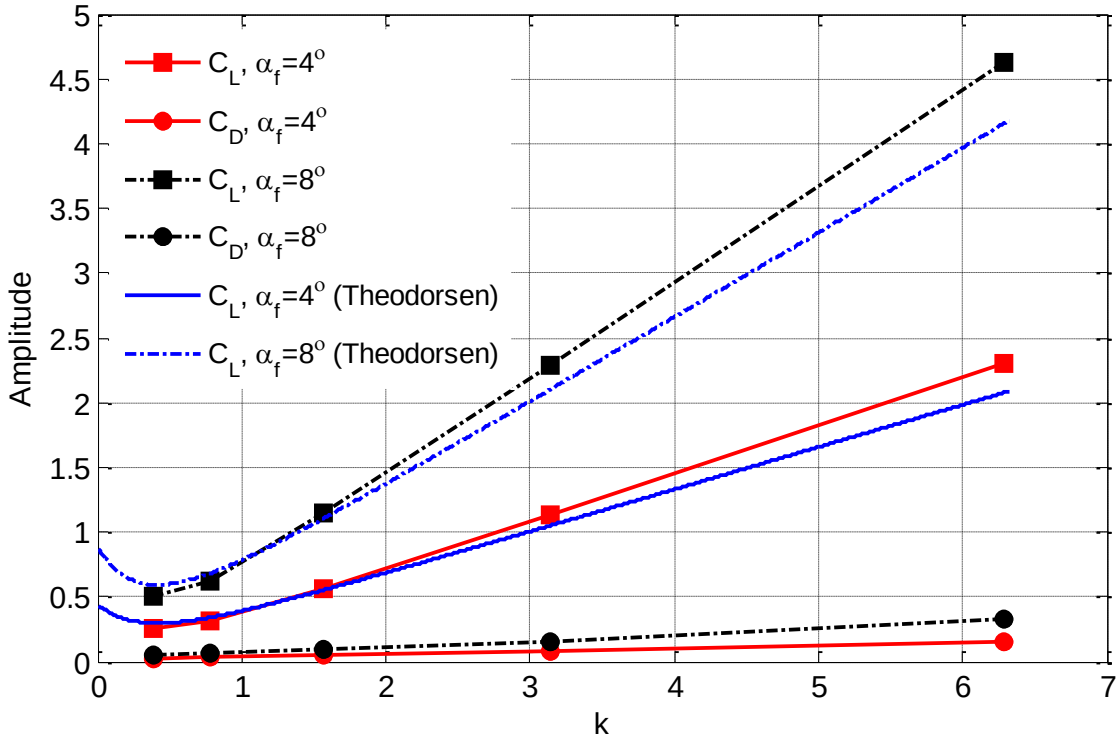

Figure 76: Amplitude of oscillations in C_L and C_D for flows with oscillating freestream AoA and the prediction by Theodorsen's theory for a pitching airfoil in the steady mean freestream.

A notable difference between the results presented in Section 5.1.1 with those shown in this section is magnitude of C_L and C_D amplitudes. For flows with oscillating freestream velocity magnitude, the oscillation amplitudes in C_L and C_D are comparable to each other. However, for flows with oscillating freestream AoA, the C_L amplitude is one order of magnitude larger than the C_D amplitude. As explained in Section 5.1.1, when the freestream has constant AoA and oscillating velocity magnitude, the acceleration and deceleration in freestream velocity induce pressure gradients in the flow direction. However, when the AoA oscillates, the direction of pressure gradient vector will also change in time with change in AoA. Figure 77 shows contours of pressure coefficient around the airfoil at the time of maximum acceleration of freestream AoA. As expected, the direction of pressure gradient in freestream, induced by changes in velocity vector is not parallel to the mean flow direction and has a significant component perpendicular to the mean flow direction, and therefore the pressure difference helps to significantly increase the lift. The pressure coefficient on the airfoil surface is shown in Figure 78. The large magnitudes of C_P in Figures 77 and 78 are mainly due to large pressure gradient in the freestream flow.

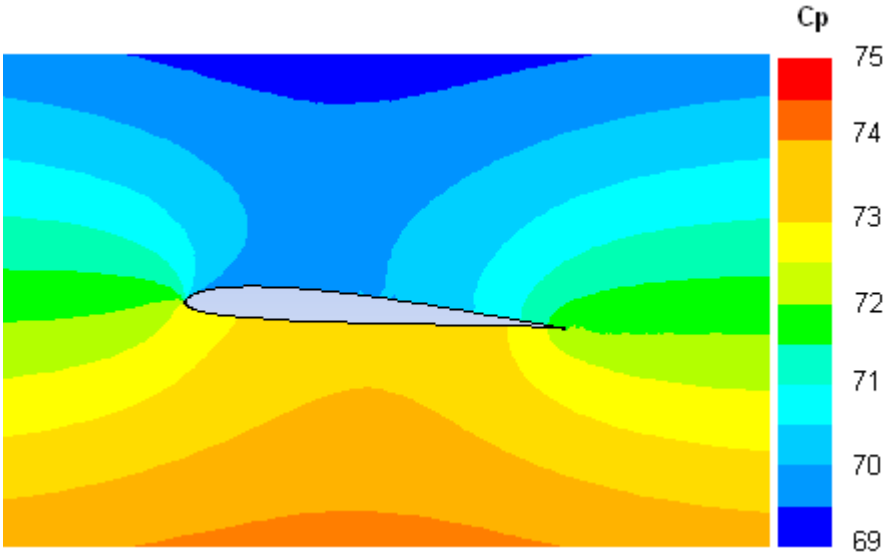

Figure 77: Contours of pressure coefficient around the airfoil at the time of maximum acceleration of freestream AoA for case A1 with $k = 2\pi$ and $\alpha_f = 4^\circ$.

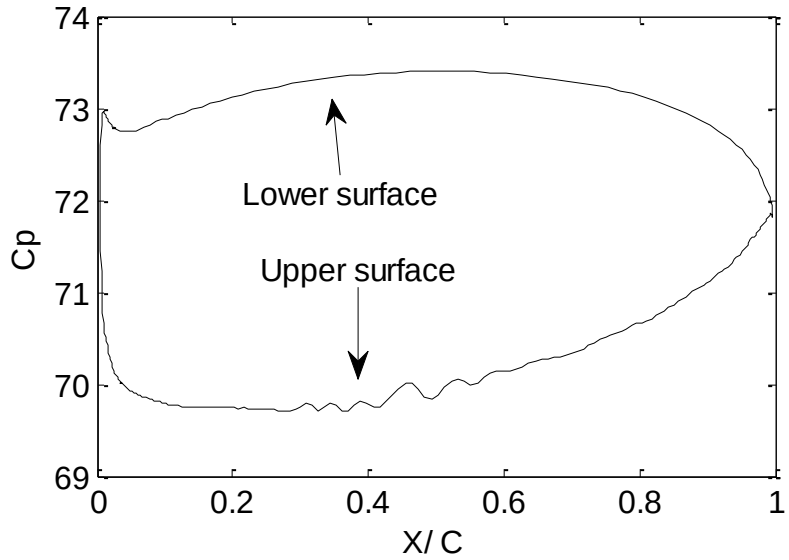

Figure 78: Pressure coefficient on the airfoil surface at the time of maximum acceleration of freestream AoA for case A1 with $k = 2\pi$ and $\alpha_f = 4^\circ$.

Figure 79 shows that the lift and drag forces lead the freestream AoA in phase. Similar to the phase shift described in Section 5.1.1, the phase shift here is calculated as the phase difference between the peak of C_L (and C_D) and the peak of freestream AoA. Similar to flows with oscillating freestream velocity magnitude, the phase shift is almost not affected by the amplitude of oscillations in AoA. However, the C_D phase shift increases as the reduced frequency decreases, which is opposite to the flows with oscillating freestream velocity magnitude. The minor decrease in C_D phase shift at low reduced frequencies (compare case A5 to case A4 for example) is due to the C_D profiles being distorted from the "sinusoidal" shape. At low reduced frequency, the C_D profile is "flattened" at high values and the peak values are delayed, and therefore the phase shift is reduced. Similar to flows with oscillating freestream velocity magnitude, the reduced frequency affects C_L phase shift more than C_D phase shift. Phase shifts in C_L and C_D seem to converge to 90 degrees at high reduced frequencies, indicating that the maximum values of the aerodynamic forces coincide with the maximum acceleration of the

freestream AoA. This is due to the fact that, at high values of reduced frequency, the non-circulatory or apparent mass terms dominate the solution [54].

Like Figure 76, Figures 79 and 80 compare the lift and drag coefficients of an airfoil pitching around the chord mid-point given by Theodorsen's theory [26] with those obtained by LES here for the fixed SD7003 airfoil in flows with oscillatory direction or AoA. Gharali and Johnson [36] compared CFD results for flows with oscillating freestream direction around a S809 airfoil to experimental results of a pitching airfoil, and found some level of agreement between them. Since the computational domain used in this study has a far-field boundary that is close to a perfect circle centered at the chord mid-point, it is speculated that flow configuration of these simulations might be equivalent, in terms of force acting on the airfoil, to the flow with steady freestream velocity U_m and the airfoil pitching around its chord mid-point with mean AoA $\alpha_m = 4°$ and AoA amplitude α_f. For a pitching airfoil, Theodorsen's theory gives the lift coefficient in Equation (43) where F and G are Theodorsen's function as described in Section 5.1.1. For C_L, Figures 76 and 79 show that the predictions of Theodorsen's theory for the phase shift and amplitude agree with the LES results quite well with only a slight discrepancy in C_L amplitude at high values of reduced frequency, even though some of the assumptions made in the theory are not necessarily satisfied for the simulated flow. However, Figure 80 shows that there is a significant discrepancy in mean C_L values obtained by LES for flows with oscillatory freestream AoA with the predictions of Theodorsen's theory for a pitching airfoil in a steady mean freestream.

$$C_L = \pi\alpha_f\left(k\cos\omega t - k^2\sin\omega t\right) + 2\pi\left[F\alpha_m + \alpha_f\left(F - \frac{kG}{2}\right)\sin\omega t + \alpha_f\left(\frac{kF}{2} + G\right)\cos\omega t\right] \tag{43}$$

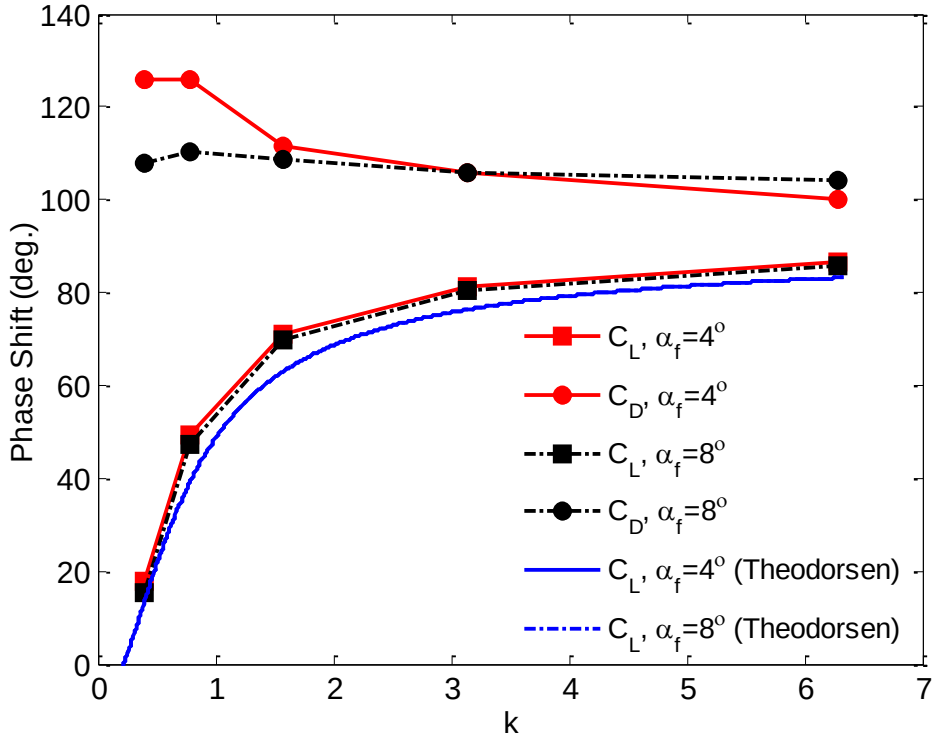

Figure 79: Phase shift of C_L and C_D for flows with oscillating AoA and the prediction by Theodorsen's theory for a pitching airfoil in the steady mean freestream. The two Theodorsen curves overlay each other.

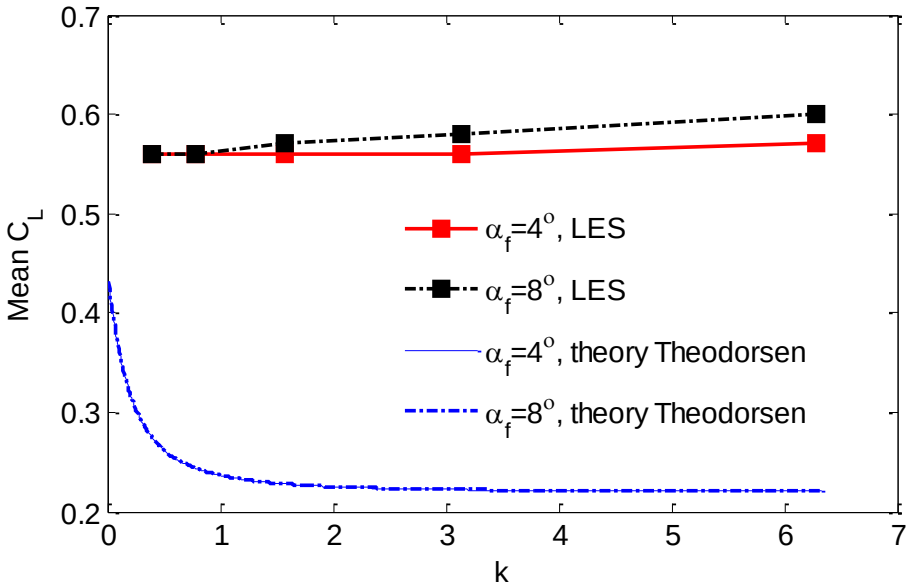

Figure 80: Computed time-averaged lift coefficient for flows with oscillating freestream AoA and the prediction by Theodorsen's theory for a pitching airfoil in the steady mean freestream. The two Theodorsen curves overlay each other.

For flows with steady freestream, both C_L and C_D increase monotonically with AoA until AoA reaches the stall angle of about 11 ° for Re=60,000 [20]. The maximum AoA considered in this section is 12 °, slightly above the stall angle. Therefore, when the reduced frequency is very low and the flow has a quasi-steady freestream condition, the maximum C_L and C_D should coincide with the maximum AoA, i.e. the phase shift between the aerodynamic force and the freestream AoA should be nearly zero. The profiles of C_L phase shift in Figure 79 clearly show that the lift coefficient is nearly in phase with the AoA at low frequencies. However, the profiles of C_D phase shift seem to follow a different trend and still show phase shifts higher than 100 degrees at low frequencies. This indicates that the minimum reduced frequency considered in this study might still be high enough to induce significant phase shift in the C_D.

5.2.2 Vorticity field

A comparison of vorticity iso-surfaces/contours made between flows with steady freestream flows at Re=60,000 and AoA=4 °, 8 °, 12 ° (Figures 81 and 82) indicates typical effects of AoA on vorticity field. For example, as the AoA increases, the separation point moves towards the leading edge and the recirculation region grows in size. However, the trends are very different when the AoA oscillates. This is illustrated in Figures 83-94, where the z-vorticity iso-surfaces/contours, and the line integrals of spanwise-averaged vorticity magnitude $\int |\Omega| dn$, $\int\int |\Omega| dnds$ for cases A1, A5, A6, and A10 are shown. The z-vorticity iso-surfaces and contours show that lower reduced frequency and higher amplitude in the AoA oscillation lead to wider variations in the vorticity field in terms of vortex size and the starting point of the recirculation region. This is consistent with $\int |\Omega| dn$ and $\int\int |\Omega| dnds$ plots in Figures 85, 88, 91, and 94. For example, in case A6 with k=2π the $\int |\Omega| dn$ profiles at four different times as shown in Figure 91

are very similar and the difference between the maximum and the minimum $\int\int|\Omega|dnds$ values is about 0.2, while in case A10 with k=π/8 the $\int|\Omega|dn$ profile varies significantly over time and the difference between the maximum and the minimum $\int\int|\Omega|dnds$ values is about 0.7. A comparison between a flow with oscillating freestream AoA and a steady freestream flow with the same maximum AoA shows that the unsteady flow has a smaller recirculation region. For example, in the extreme case A10 with k=π/8 and $\alpha_f = 8°$ (Figures 92 and 93) the freestream AoA varies from -4 ° to 12 ° during one freestream cycle, but the maximum size of the recirculation region is similar to that of the steady freestream flow with AoA=8 °, which is much smaller than that of the steady freestream flow with AoA=12 °(Figures 81 and 82).

By relating the C_D values of case A10 ($\alpha_f = 8°$, k=π/8) in Figure 73 with the z-vorticity iso-surfaces in Figure 92, it can be seen that the boundary layer separation occurs around the same time (t0+T/2) when the C_D value starts to flatten out. Compared to flows oscillating with high reduced frequency, those with low reduced frequency have more time to develop and thus cannot sustain the adverse pressure gradient and experience separation near the leading edge. After the separation, the static pressure in the recirculation region recovers from its low values, keeping the drag coefficient low and the C_D profile flattened.

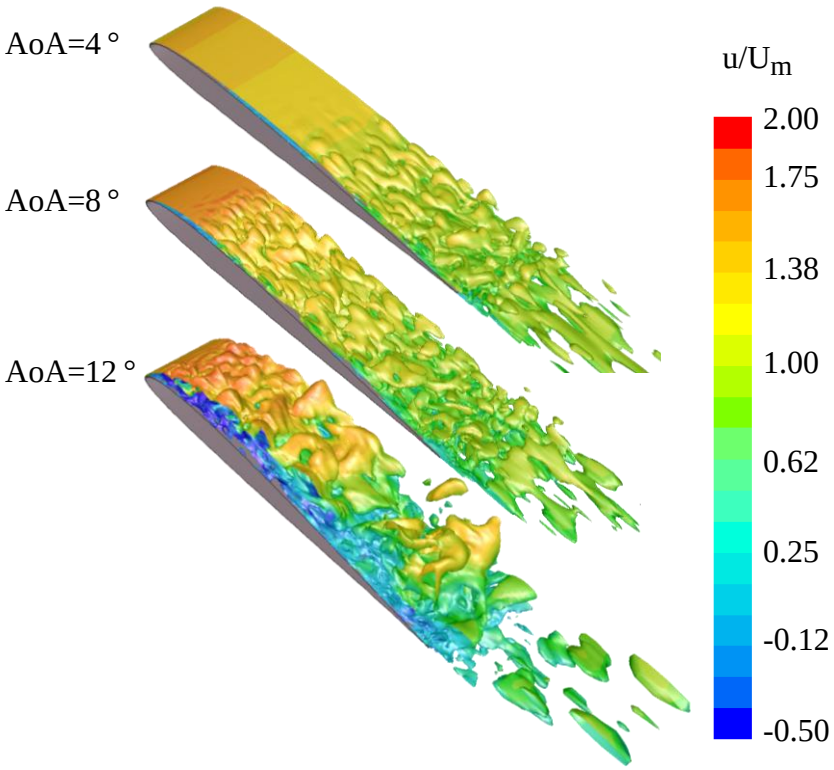

Figure 81: Instantaneous iso-surfaces of z-vorticity ($\omega_z C/U_m = -10$) for flows with steady freestream, Re=60,000 and AoA=4 °, 8 °and 12 °.

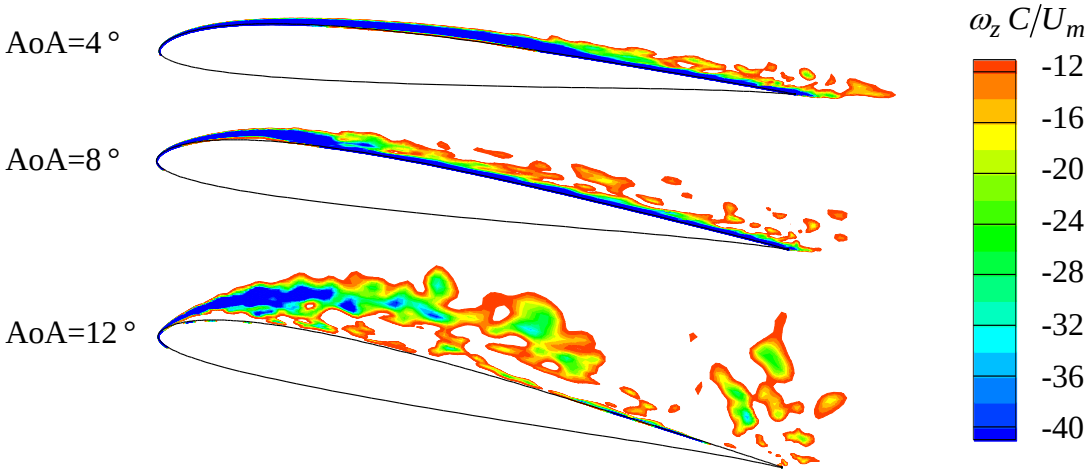

Figure 82: Instantaneous contours of spanwise-averaged z-vorticity ($\omega_z C/U_m$) for flows with steady freestream, Re=60,000 and AoA=4 °, 8 °and 12 °.

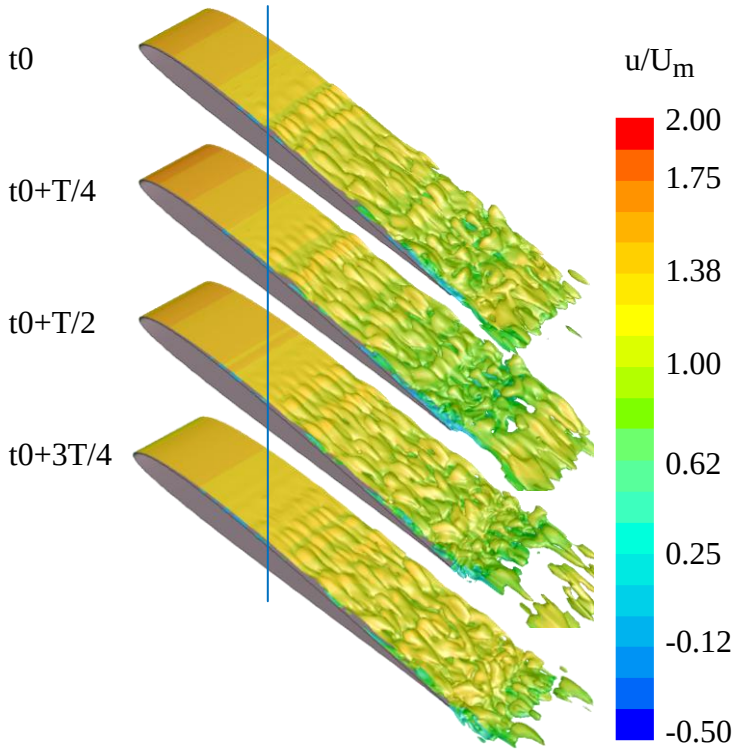

Figure 83: Instantaneous iso-surfaces of z-vorticity ($\omega_z C/U_m = -10$) for case A1 with $k = 2\pi$ and $\alpha_f = 4^\circ$. At t0, α(t) = 4 °; at t0+T/4, α(t) = 8 °; at t0+T/2, α(t) = 4 °; at t0+3T/4, α(t) = 0 °.

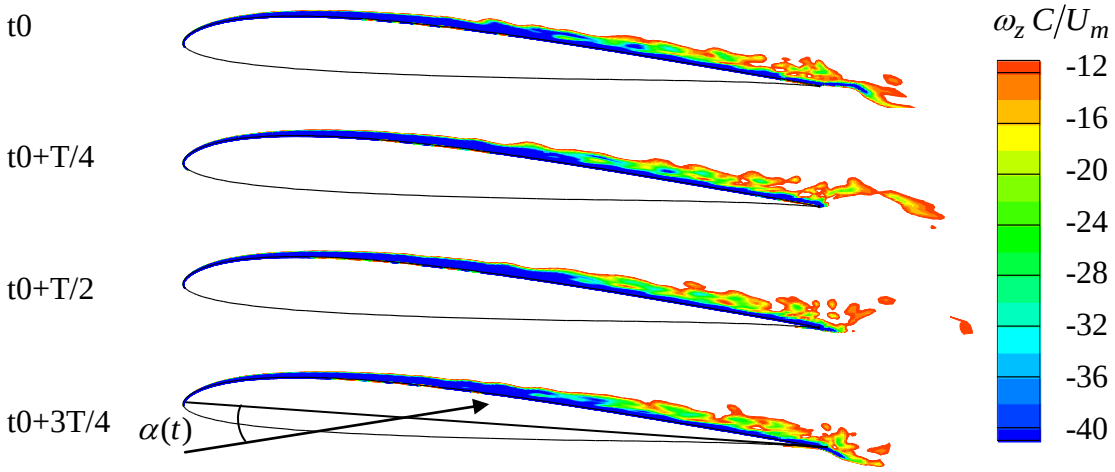

Figure 84: Instantaneous contours of spanwise-averaged z-vorticity ($\omega_z C/U_m$) for case A1 with $k = 2\pi$ and $\alpha_f = 4^\circ$. At t0, α(t) = 4 °; at t0+T/4, α(t) = 8 °; at t0+T/2, α(t) = 4 °; at t0+3T/4, α(t) = 0 °.

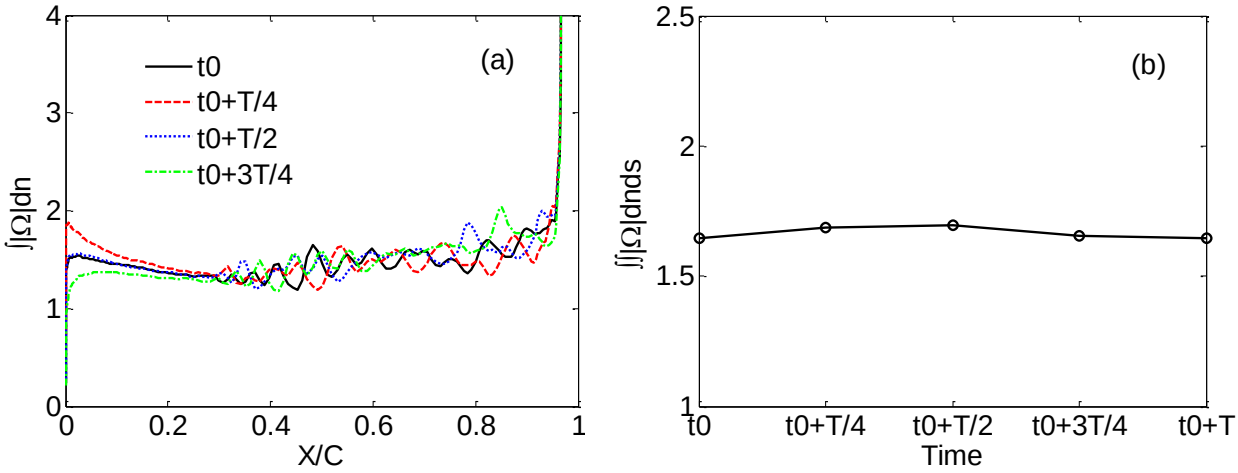

Figure 85: Integrals of spanwise-averaged vorticity magnitude |Ω| for case A1 with $k = 2\pi$ and $\alpha_f = 4^\circ$. (a) Integrated along n axis; (b) integrated along n and then s axes.

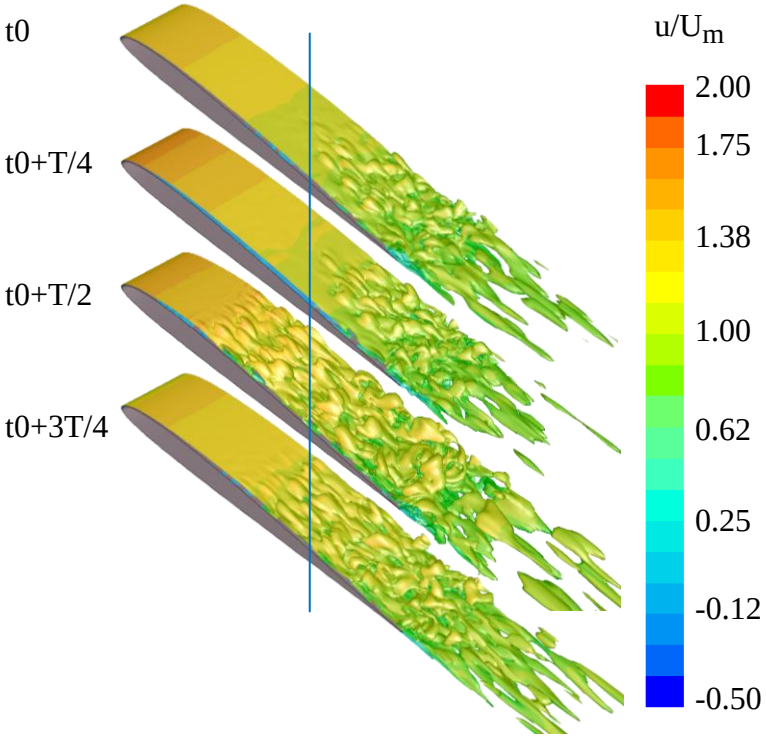

Figure 86: Instantaneous iso-surfaces of z-vorticity ($\omega_z C/U_m = -10$) for case A5 with $k = \pi/8$ and $\alpha_f = 4^\circ$. At t0, α(t) = 4 °; at t0+T/4, α(t) = 8 °; at t0+T/2, α(t) = 4 °; at t0+3T/4, α(t) = 0 °.

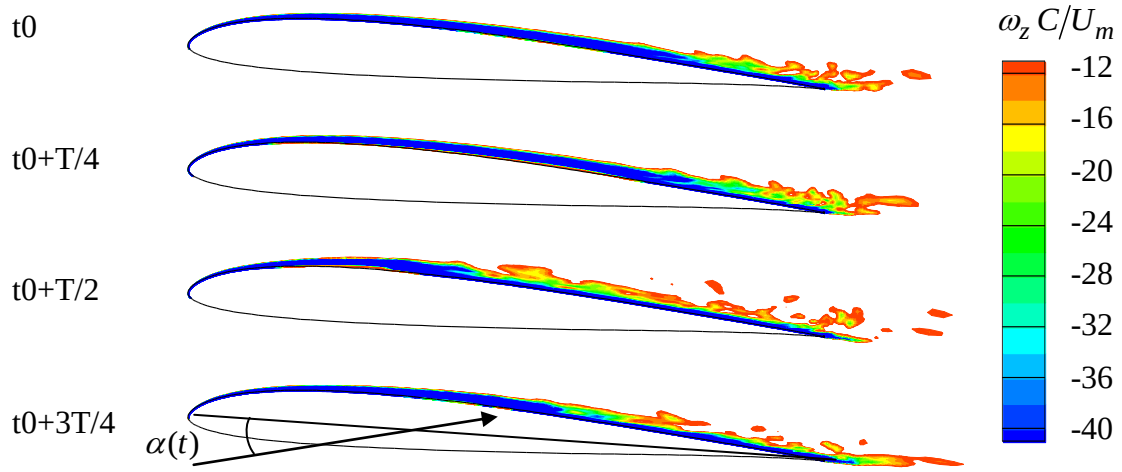

Figure 87: Instantaneous contours of spanwise-averaged z-vorticity ($\omega_z C/U_m$) for case A5 with $k=\pi/8$ and $\alpha_f = 4^\circ$. At t0, α(t) = 4 °; at t0+T/4, α(t) = 8 °; at t0+T/2, α(t) = 4 °; at t0+3T/4, α(t) = 0 °.

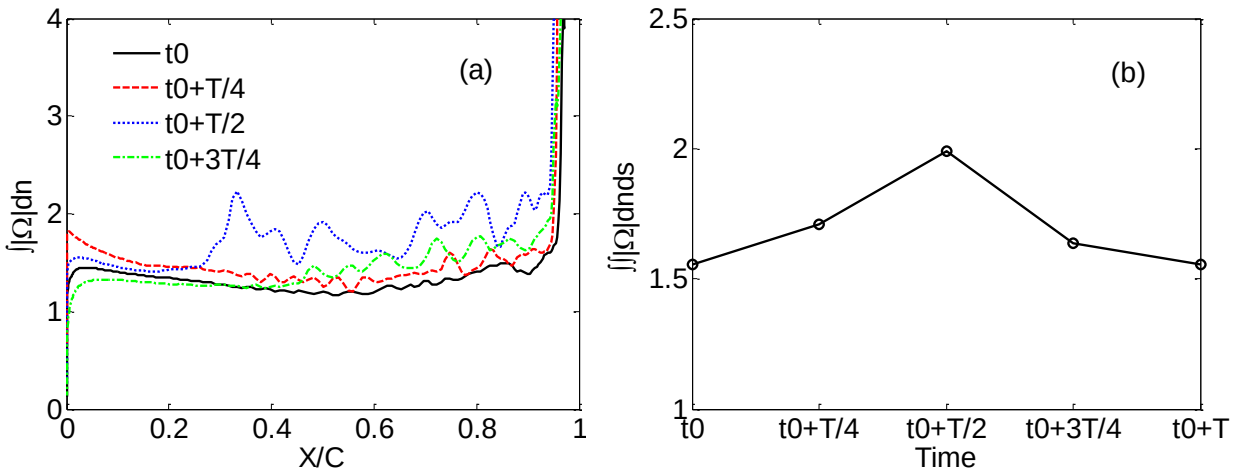

Figure 88: Integrals of spanwise-averaged vorticity magnitude |Ω| for case A5 with $k=\pi/8$ and $\alpha_f = 4^\circ$. (a) Integrated along n axis; (b) integrated along n and then s axes.

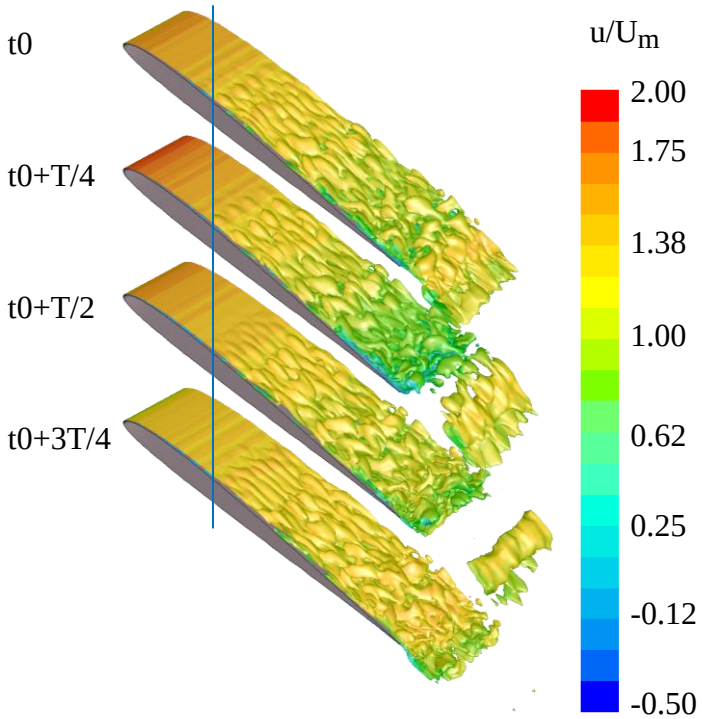

Figure 89: Instantaneous iso-surfaces of z-vorticity ($\omega_z C/U_m = -10$) for case A6 with $k = 2\pi$ and $\alpha_f = 8^\circ$. At t0, α(t) = 4 °; at t0+T/4, α(t) = 12 °; at t0+T/2, α(t) = 4 °; at t0+3T/4, α(t) = -4 °.

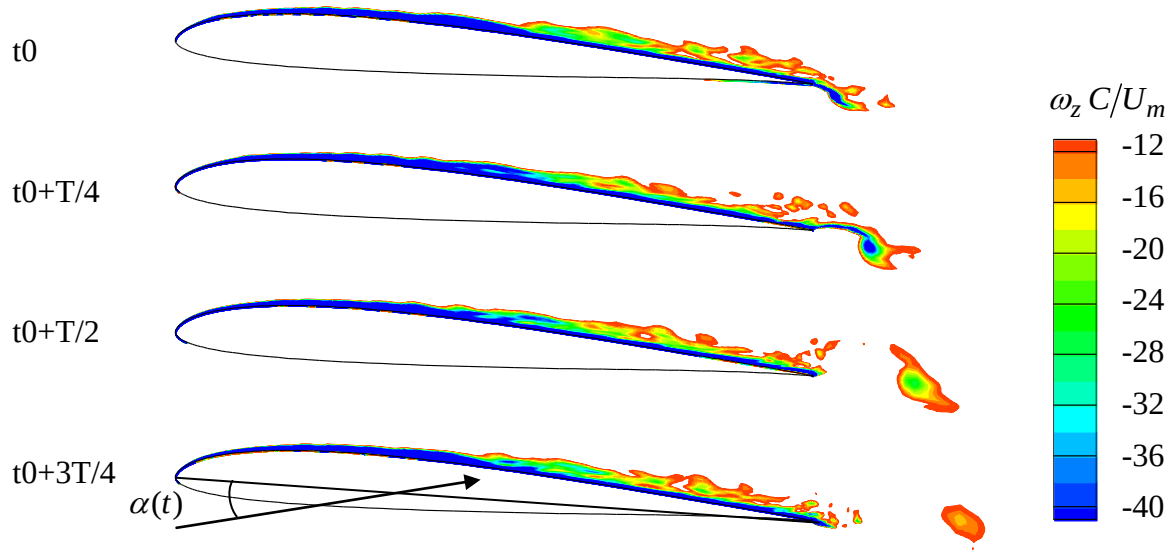

Figure 90: Instantaneous contours of spanwise-averaged z-vorticity ($\omega_z C/U_m$) for case A6 with $k = 2\pi$ and $\alpha_f = 8^\circ$. At t0, α(t) = 4 °; at t0+T/4, α(t) = 12 °; at t0+T/2, α(t) = 4 °; at t0+3T/4, α(t) = -4 °.

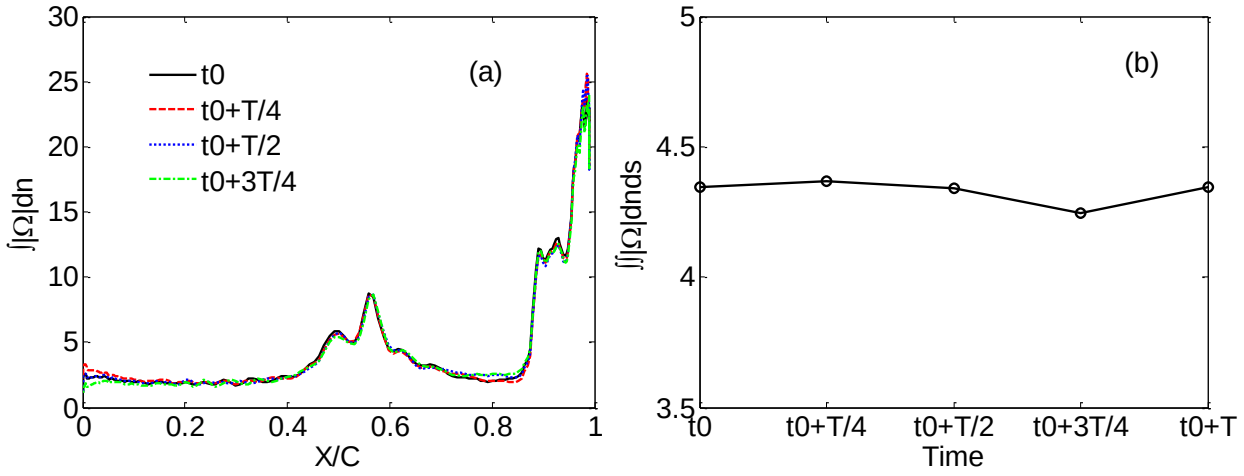

Figure 91: Integrals of spanwise-averaged vorticity magnitude |Ω| for case A6 with $k = 2\pi$ and $\alpha_f = 8^\circ$. (a) Integrated along n axis; (b) integrated along n and then s axes.

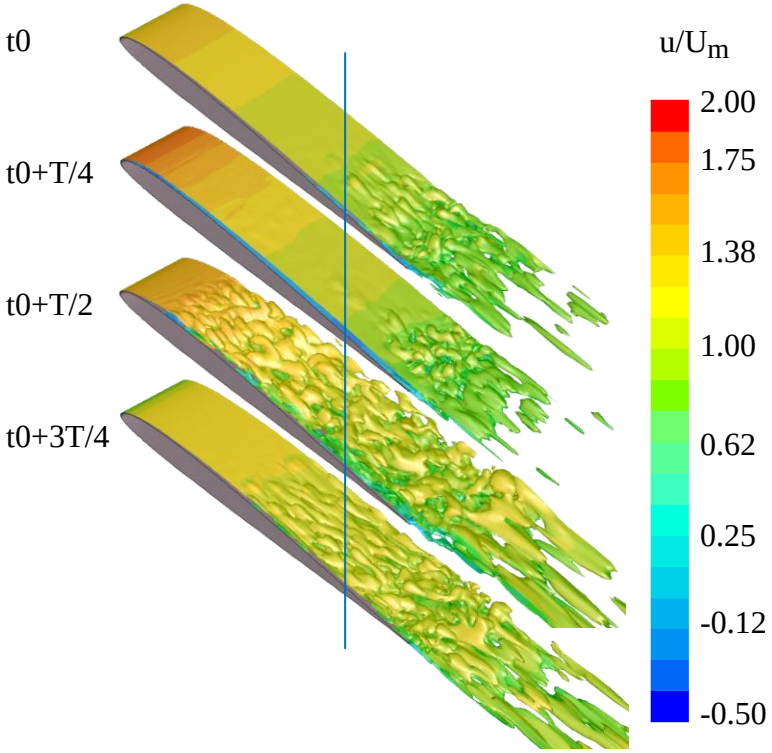

Figure 92: Instantaneous iso-surfaces of z-vorticity ($\omega_z C/U_m = -10$) for case A10 with $k = \pi/8$ and $\alpha_f = 8^\circ$. At t0, α(t) = 4 °; at t0+T/4, α(t) = 12 °; at t0+T/2, α(t) = 4 °; at t0+3T/4, α(t) = -4 °.

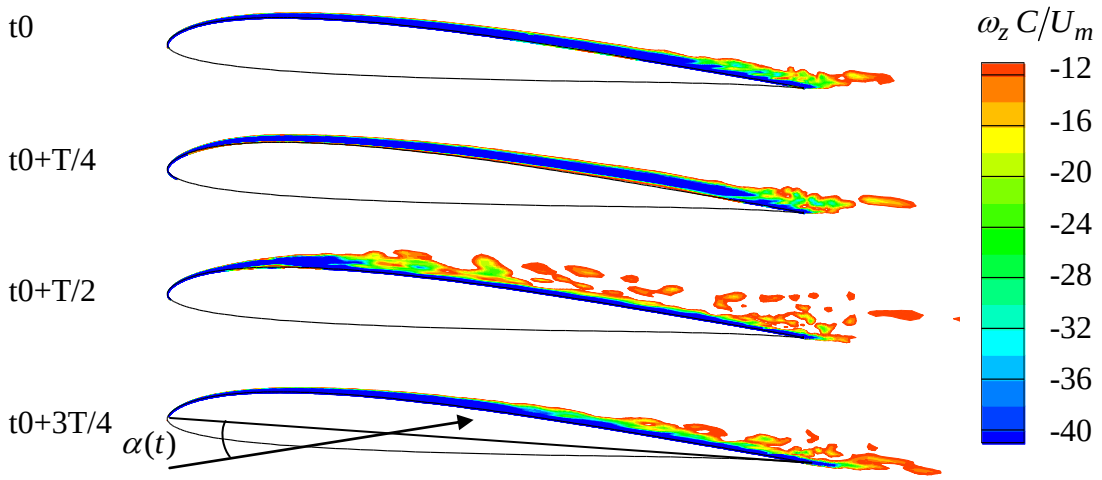

Figure 93: Instantaneous contours of spanwise-averaged z-vorticity ($\omega_z C/U_m$) for case A10 with $k=\pi/8$ and $\alpha_f=8^\circ$. At t0, α(t) = 4 °; at t0+T/4, α(t) = 12 °; at t0+T/2, α(t) = 4 °; at t0+3T/4, α(t) = -4 °.

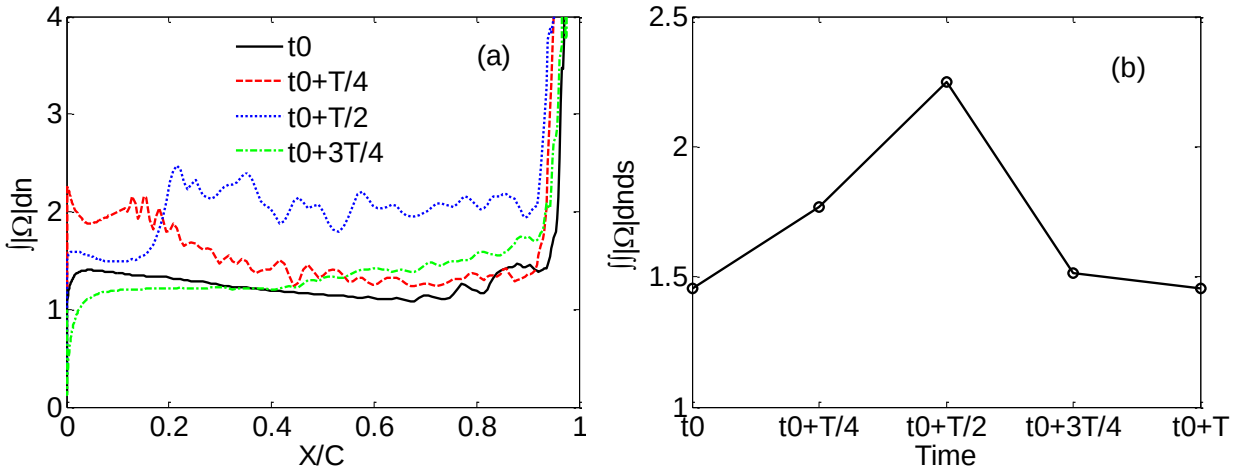

Figure 94: Integrals of spanwise-averaged vorticity magnitude |Ω| for case A10 with $k=\pi/8$ and $\alpha_f=8^\circ$. (a) Integrated along n axis; (b) integrated along n and then s axes.

5.2.3 Velocity fluctuations

The effect of freestream AoA oscillations on velocity fluctuations over the airfoil is studied in this section by considering the RMS values of various velocity components and TKE for case A6. Case A6 is selected since it has the highest frequency of k=2π and the largest amplitude of $\alpha_f=8^\circ$. Figure 95 shows that the integrated values of velocity RMS along airfoil surface

normal direction, (n), $\int (RMS)dn$ at four different times during a cycle of oscillation in AoA are nearly the same. This is further confirmed by the integrated values of velocity RMS along airfoil surface normal and tangent directions, (n, s), $\int\int (RMS)dnds$ in Figure 96 and those of TKE in Figure 97. It is evident that the velocity fluctuations at different phases, as measured by RMS values are similar when the oscillation in freestream direction has a high reduced frequency. It can also be seen in Figures 95 and 96 that the RMS of x-velocity and RMS of y-velocity components (u′ and v′) are comparable and are one order of magnitude higher than the RMS of z-velocity component (w′). The RMS of y-velocity is slightly higher than the RMS of x-velocity (Figure 96), which shows that the oscillation in freestream AoA can cause more fluctuation in y-velocity than in x-velocity.

The trends in Figures 96 and 97 are similar to those in Figures 63 and 64, indicating that qualitatively the effects of freestream oscillations in AoA on the airfoil flow velocity fluctuations are similar to those caused by oscillations in the freestream velocity magnitude. However, the velocity fluctuations induced by AoA oscillations are observed to be quantitatively much more significant than those caused by velocity magnitude oscillations.

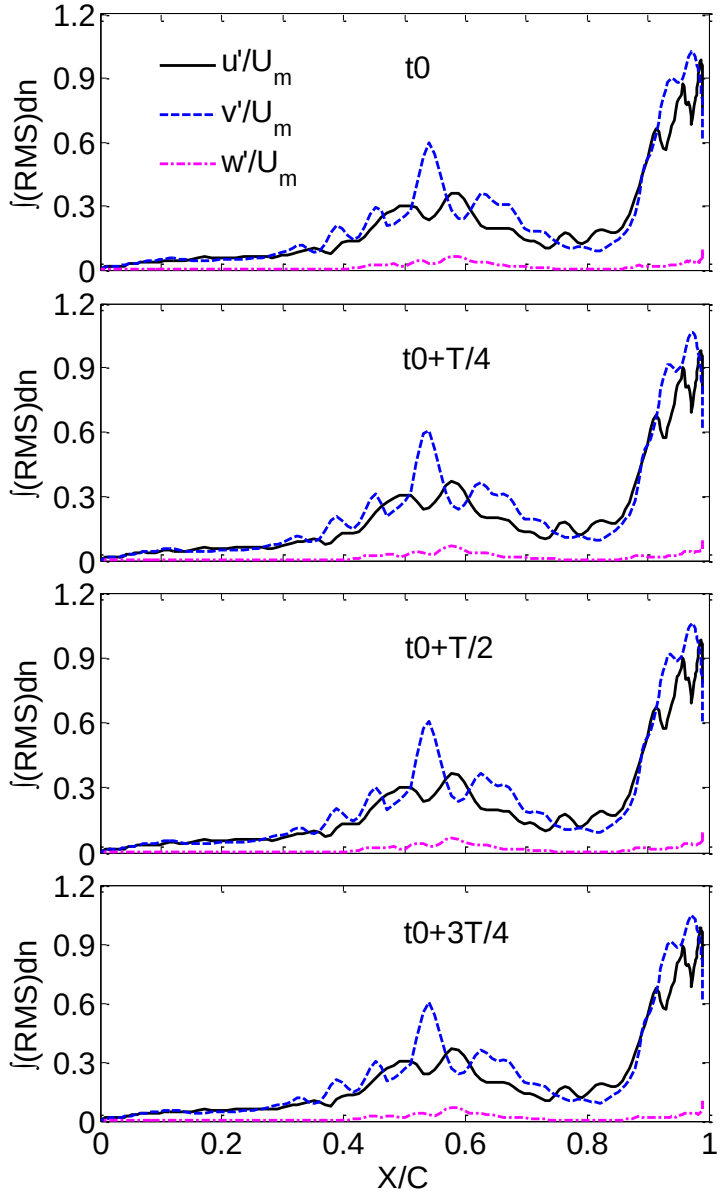

Figure 95: Integral of velocity RMS along airfoil surface normal direction, n for case A6 with $k = 2\pi$ and $\alpha_f = 8^\circ$.

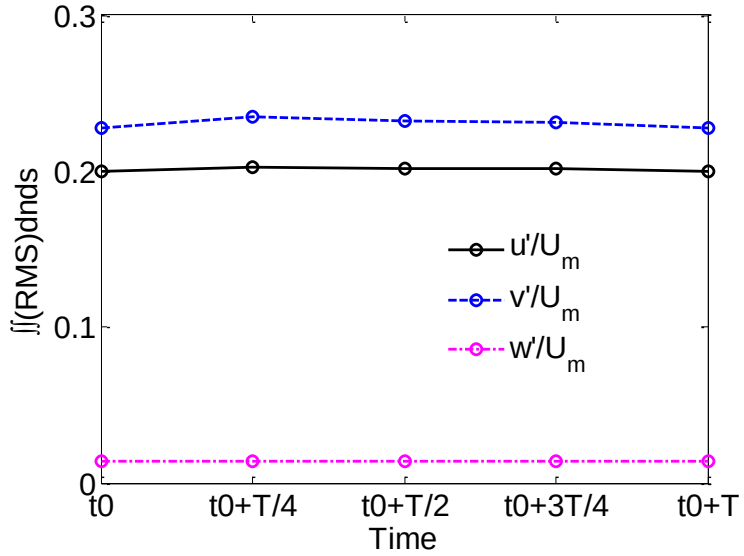

Figure 96: Integral of velocity RMS along n and s axes for case A6 with $k = 2\pi$ and $\alpha_f = 8^\circ$.

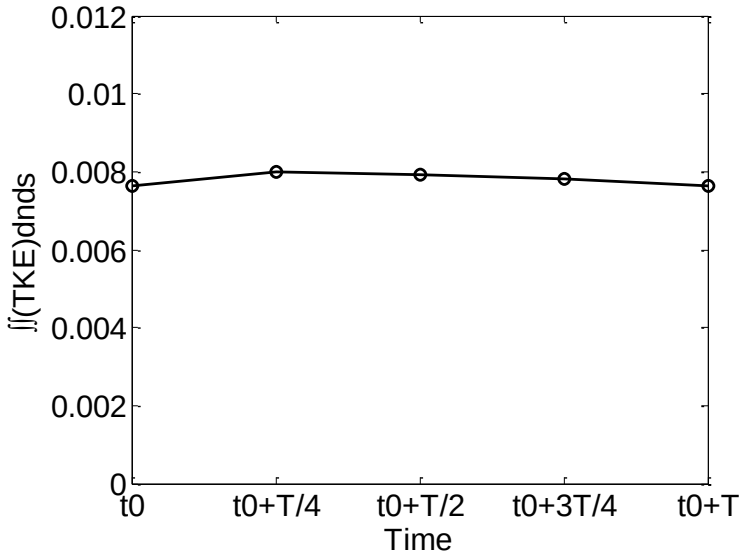

Figure 97: Integral of turbulence kinetic energy (TKE) along n and s axes for case A6 with $k = 2\pi$ and $\alpha_f = 8^\circ$.

5.2.4 Boundary layer separation and reattachment

In this section, the effects of oscillating freestream direction or AoA on the boundary layer separation and reattachment are examined. Mean and instantaneous values of the skin friction coefficient on the airfoil for cases A1, A3, A5, A6, and A10 are plotted in Figures 98-102. Similar plots for the steady freestream flow with Re=60,000 and AoA=4 ° were previously shown in Figure 66 in Section 5.1.4. A comparison between steady and unsteady cases indicates the C_F variation, or profile over the airfoil becomes very different when the freestream flow direction oscillates. The C_F profiles are also very different at different phases or times. Figures 98-100 show that as the reduced frequency of oscillation in AoA increases, the separation point moves less. This is in agreement with the observation made in the previous section that higher frequency of oscillation in freestream AoA leads to lower variation in the vorticity magnitude. Another observation made from C_F plots in Figures 98-100 is that, close to the trailing edge, C_F oscillates around the mean value with larger amplitude as the reduced frequency increases. This is due to vortex shedding from the trailing edge that occurs at high reduced frequencies (Figures 83, 84, 89 and 90). Because of oscillation in the freestream flow direction, the vortex shed from the airfoil upper surface near the trailing edge can move either upward or downward. For the vortex to be shed downward, the fluid above the airfoil upper surface and near the trailing edge will have to impinge the airfoil surface harder in comparison to the flow with the vortex shed upward, thus the instantaneous C_F has to be higher than the averaged C_F. A comparison between Figure 100 (case A1) and Figure 101 (case A6) shows that as the amplitude of oscillation in AoA increases, the instantaneous separation point moves upstream towards the leading edge, and the near trailing edge values of C_F also oscillate more. A comparison between Figure 101 (case A6) and Figure 102 (case A10) shows that the oscillation in C_F around the trailing edge subsides

significantly when the reduced frequency drops from 2π to $\pi/8$, which again shows the significance of vortex shedding at the trailing edge and the effect it has on the C_F.

The mean separation and reattachment points reported in Table 8 are obtained based on the mean skin friction coefficient. No separation (and thus reattachment) is found for cases A1 and A6-10. For cases A2-5 which have separation and reattachment points, the mean separation point is delayed by an increase in the reduced frequency. Compared to the flow with steady freestream velocity, results of the ten cases considered here show that oscillations in freestream flow AoA generally suppress the mean separation.

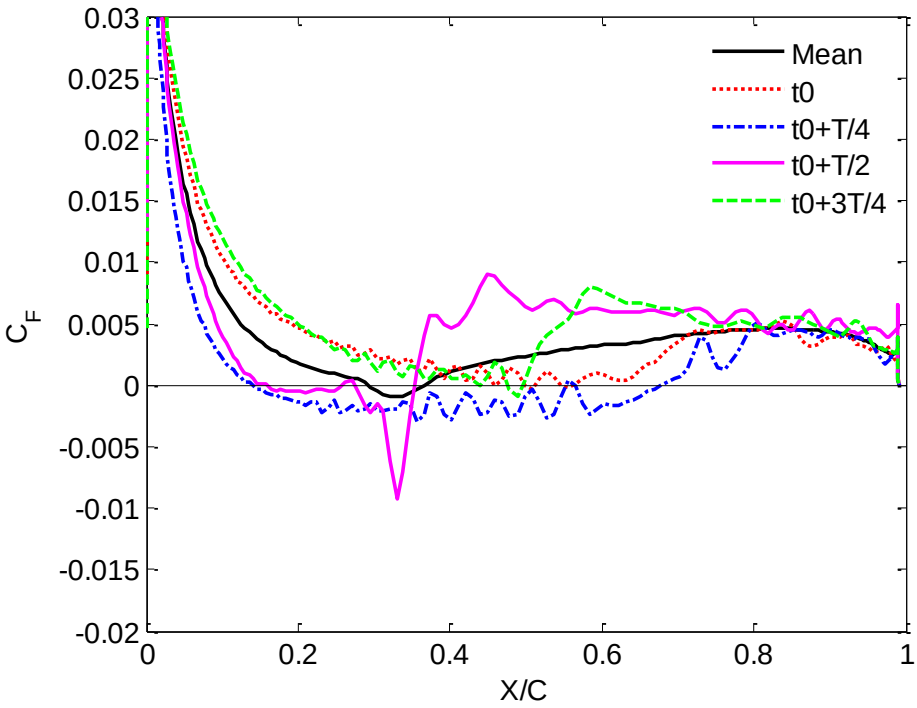

Figure 98: Time-averaged and instantaneous skin friction coefficient on the airfoil upper surface for case A5 with $k = \pi/8$ and $\alpha_f = 4^\circ$.

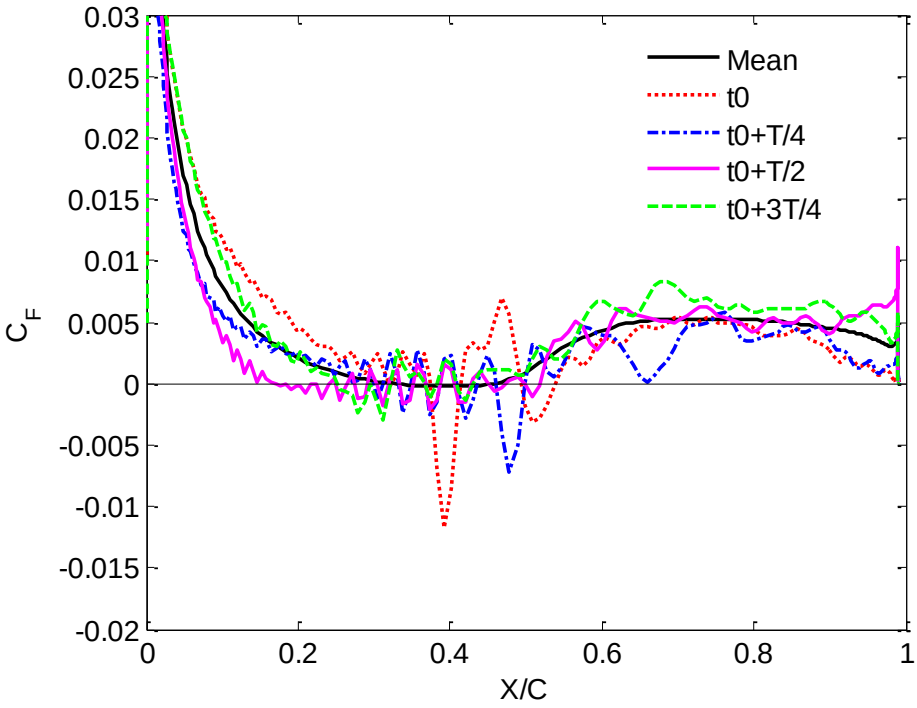

Figure 99: Time-averaged and instantaneous skin friction coefficient on the airfoil upper surface for case A3 with $k = \pi/2$ and $\alpha_f = 4^\circ$.

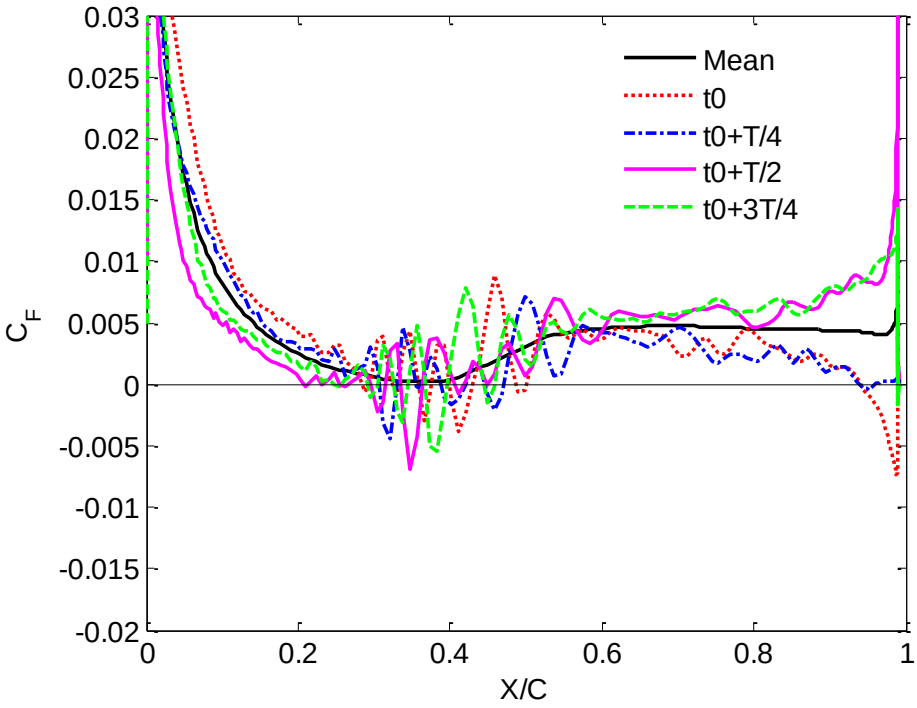

Figure 100: Time-averaged and instantaneous skin friction coefficient on the airfoil upper surface for case A1 with $k = 2\pi$ and $\alpha_f = 4^\circ$.

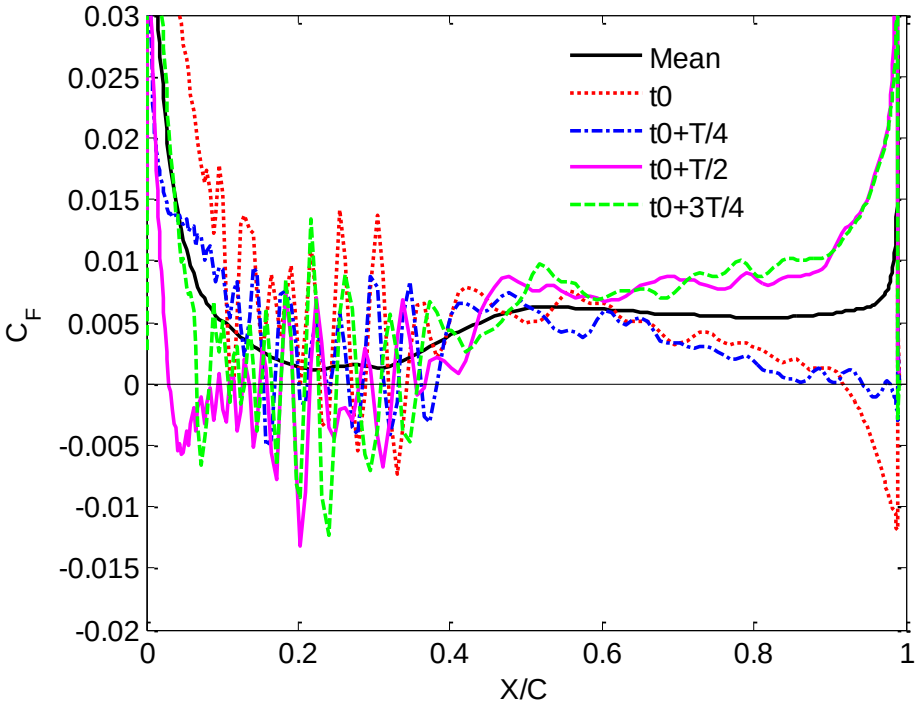

Figure 101: Time-averaged and instantaneous skin friction coefficient on the airfoil upper surface for case A6 with $k = 2\pi$ and $\alpha_f = 8^\circ$.

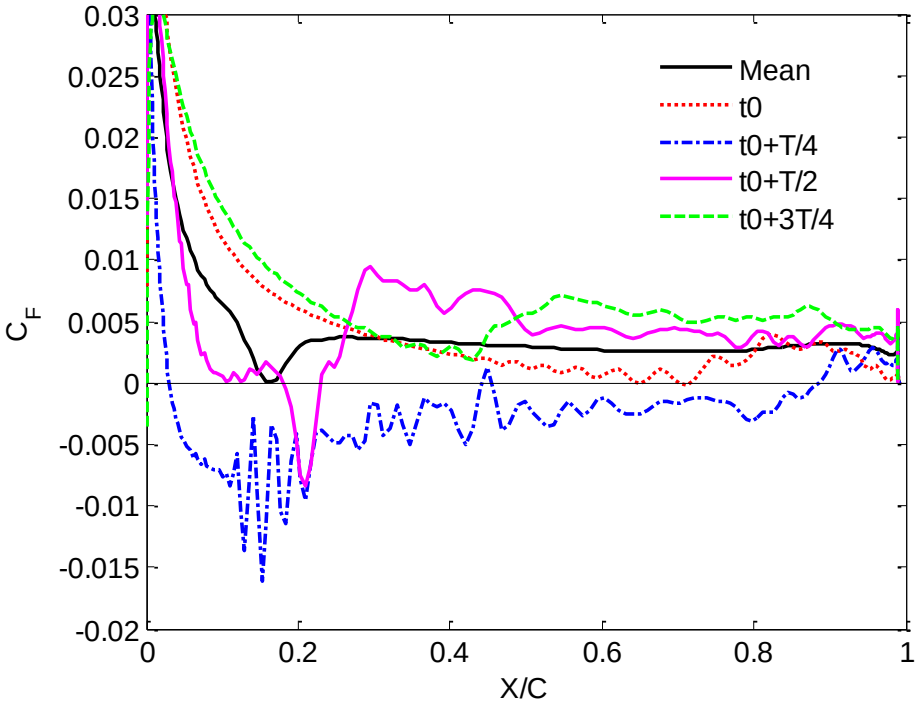

Figure 102: Time-averaged and instantaneous skin friction coefficient on the airfoil upper surface for case A10 with $k = \pi/8$ and $\alpha_f = 8^\circ$.

5.3 A Discussion Regarding Effect of Freestream Unsteadiness on Mean Separation and Reattachment Points

There have been some discussions in the literature regarding the effect of freestream flow perturbations on the mean separation and reattachment points. Measurements of laminar separation bubble (LSB) over SD7003 airfoil at Re=60,000 and AoA=4 ° were conducted at four different facilities [9, 29] including the tow tank at Institute for Aerospace Research (IAR), the low-noise wind tunnel at Technical University of Braunschweig (TU-BS), the free-surface water tunnel at Air Force Research Laboratory (AFRL), and the closed-circuit water tunnel at RWTH Aachen University. Mean separation and reattachment data from these facilities are listed in Table 9, along with the estimated freestream turbulence intensity in the facilities. Evidently, IAR and TU-BS data agree quite well, the slight difference can be partly due to the finite aspect ratio of the wing in the IAR facility which induces a smaller effective AoA than those in the other three cases [9]. In the AFRL experiment, the separation bubble forms considerably further upstream and the boundary layer reattaches also further upstream in comparison to IAR and TU-BS data, which is likely caused by a true AoA that may be slightly larger than the nominal [9]. The RWTH data show delayed separation and advanced reattachment (and consequently smaller LSB) compared to the other three data sets. This seems to be caused mainly by the substantially higher freestream turbulence intensity in the RWTH facility.

Data Set	Freestream Turbulence Intensity, (%)	Separation X_s/C	Reattachment X_r/C
IAR	0	0.33	0.63
TU-BS	0.1	0.30	0.62
AFRL	~0.1	0.18	0.58
RWTH	1	0.390	0.515

Table 9: Measured separation and reattachment points for AoA=4 ° and Re=60,000 from different experimental facilities.

Burgmann et al. [29, 52] at RWTH Aachen University measured the flow over SD7003 airfoil with Re=20,000 and AoA=4° at two levels of freestream turbulence. The freestream turbulence intensity was 1.5% in their earlier experiments, but with additional flow conditioning devices in their later experiments it was lowered to 1%. The measured separation and reattachment points from these experiments are reported in Figure 103, which clearly indicates that the separation point moves downstream at higher turbulence intensity, except in the case with an AoA of 8°. At this high AoA, the strong adverse pressure gradient at the separation region could make the effect of freestream turbulence intensity become insignificant. These data do not support the discussion about effect of turbulence intensity on reattachment, because the method of determining the reattachment point in the later experiments is fundamentally different from that in the earlier experiments. In the earlier experiments, both separation and reattachment points were determined using time-mean streamlines. In the later experiments, an instantaneous reattachment point was determined at each time step dividing the flow field into a main recirculation region and a region of shed vortices, and then the variables were averaged to be the time-mean reattachment point. It was noted by Burgmann et al. that this new method results in reattachment points to significantly move upstream in comparison with points obtained based on mean streamlines.

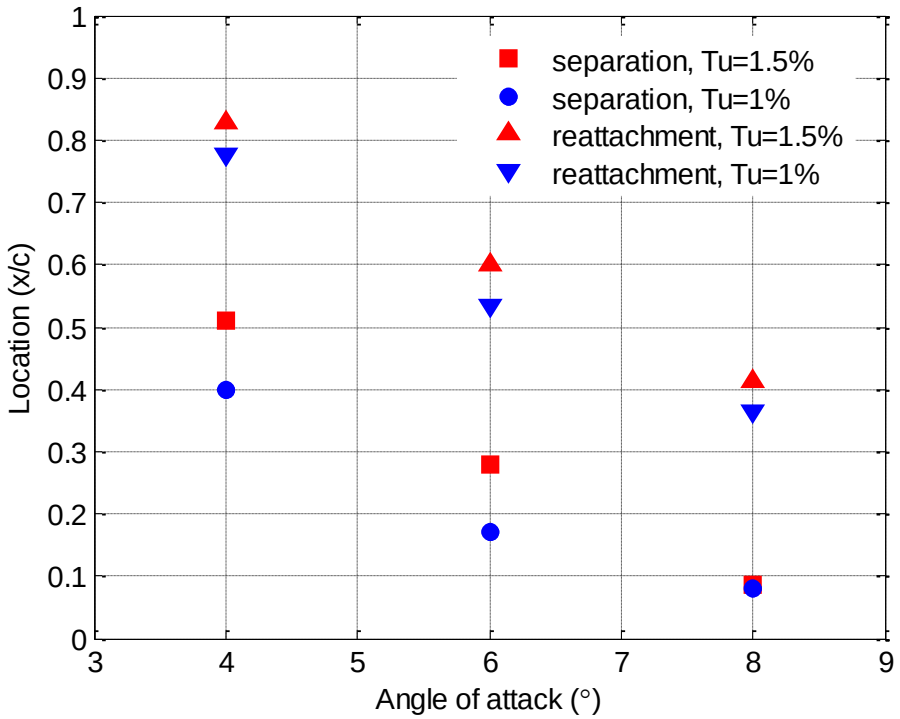

Figure 103: Comparison of the separation and reattachment points for freestream turbulence intensity of 1.0% and 1.5% at Re=20,000 [29, 52].

Galbraith [20] used LES to investigate the sensitivity of the separation bubble size and shape to the leading edge disturbances in steady flows. The disturbance was selected to be a wall normal zero-net mass-flow blowing/suction slot with a streamwise sinusoidal distribution, and the slot was positioned near the leading edge. Two disturbance velocity amplitudes, with 0.1% and 1% of the freestream velocity, were considered. It was found that, for both disturbance velocity amplitudes, the separation point moves downstream while the reattachment point moves upstream, resulting in diminished separation bubbles compared to the case without disturbances.

Olson [12] measured the LSB size over a stationary SD7003 airfoil under different levels of freestream turbulence and verified that the increased freestream turbulence moves the separation point downstream and the reattachment point upstream. It was further shown that the increase in

freestream turbulence can even eliminate the reversed flow region in the mean flow plots (within the resolution of the measurements).

In the current study, the mean separation and reattachment results in Sections 5.1.4 and 5.2.4 show that the harmonic oscillations of freestream velocity, either in magnitude or direction, will delay the mean separation, pushing it downstream and trigger earlier mean reattachment closer to the leading edge up to the point that the mean flow may become fully attached. Compared to the studies mentioned above, flows in this study have much higher level of freestream fluctuations. This implies that suppression of LSB could occur under much higher level of freestream fluctuations than freestream turbulence. Nevertheless, our findings are consistent with most of experimental data reported in the literature.

5.4 Flow with Wind Gust

This section considers the aerodynamic response of the SD7003 airfoil to a wind gust. Wind gust is difficult to predict or model as it depends on many factors such as the geographical location and season. This is evident in the measured time variation of wind speed shown in Figure 104 [56, 57]. As a universal model of wind gust is not realistic, and a simple model can be very helpful in better understanding of flow over airfoils in harsh wind gust environment.

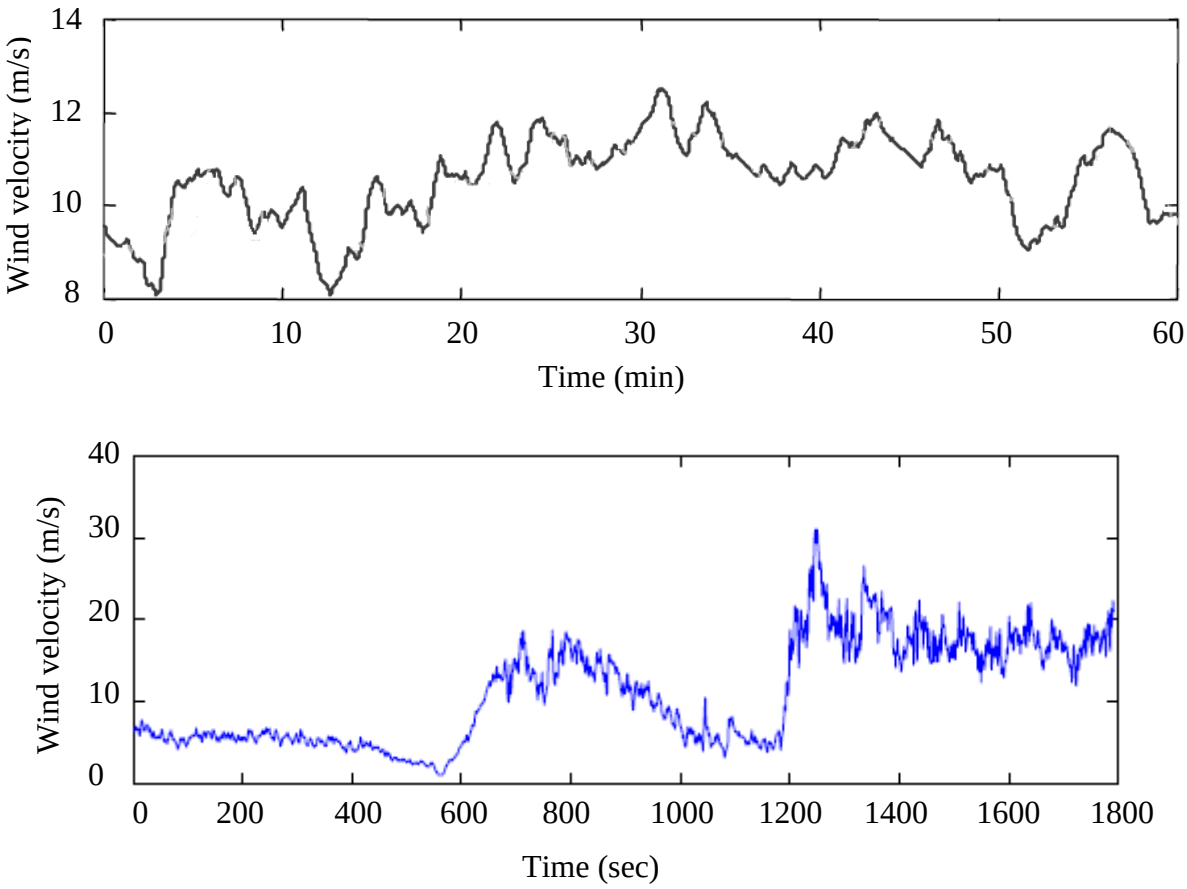

Figure 104: Measured wind speed at (upper) a sea mast in Vindeby offshore wind farm [56] and (lower) a 10 meter tower [57].

Here, the flow over SD7003 airfoil is computed by LES with a wind gust model [58] incorporated into the freestream flow. The model involves a sudden increase and smoother

decrease in wind speed with added oscillations, while the wind direction is kept constant with a fixed AoA of 4°. It takes the following form

$$U(t) = U_0 + G_1 + G_2 + G_3. \tag{44}$$

where U_0 is the freestream velocity prior to the wind gust, and G_1, G_2, G_3 are defined as

$$G_1 = D_1 t \exp(-D_2 t), \tag{45}$$

$$G_2 = D_3 erf\left(D_4 t\right), \tag{46}$$

$$G_3 = D_5 \exp\left(D_6 t\right) \sin\left(D_7 t\right), \tag{47}$$

$D_1 \sim D_7$ are the model constants. The "damping" function, G_1 causes a sudden increase in the freestream wind speed, the saturation function G_2 sets the speed after the wind gust, and G_3 controls the perturbations of the wind gust. The model constants can be adjusted to reflect different type of "wind gusts".

The model constants in Table 10 generate the wind gust shown in Figure 105. The Reynolds number for the steady flow before the wind gust is Re=60,000. The sudden increase in velocity drives the Reynolds number up to maximum Re=74,000. It takes about 3 residence times (residence time= C/U_0) for the freestream velocity to decline from the maximum velocity and stabilize at Re=63,000.

Constants	D1	D2	D3	D4	D5	D6	D7
Values	$700U_0$	$7/(3T_R)$	1	$1/T_R$	0.15	$7/(10T_R)$	$20\pi/T_R$

Table 10: Constants of the wind gust model.

The time variation of lift and drag coefficients obtained by LES is shown in Figure 105. The lift and drag coefficients are defined in the same way they were defined in the previous sections, with the freestream velocity prior to the wind gust U_0 as the reference velocity in both coefficients. Prior to the wind gust, the flow with steady freestream is fully developed with C_L and C_D fluctuating slightly around their time-averaged values of 0.59 and 0.020. As the wind gust moves over the airfoil, C_L and C_D rapidly increase to maximum values of 0.84 and 0.17, respectively, and then start to decrease as the freestream velocity declines. The lift coefficient closely follows the trend in the freestream velocity and stabilizes at a value slightly higher than that prior to the wind gust since the lift force is normalized by U_0 which is lower than U after the wind gust as shown in Figure 105, while the drag coefficient goes negative before it stabilizes at a value very close to that prior to the wind gust. The perturbation parameter G_3 generates oscillations in C_L and C_D with the frequency comparable to that of the freestream flow. The amplitudes of fluctuations in C_L and C_D diminish as the amplitude of wind perturbation decays. The maximum amplitude in G_3 is less than 1% of U_0, yet it causes fluctuations in C_L and C_D with amplitude up to 3% of the maximum C_L value and 15% of the maximum C_D value. This suggests that even a weak (low amplitude) wind gust can have a significant effect on the aerodynamic forces and the flight stability of MAVs. The lift and drag coefficients obtained by normalizing the forces with the time-dependent U(t) are also plotted in Figure 105, and as expected, are lower than those obtained by normalizing the forces with U_0.

The iso-surfaces of z-vorticity of the flow over the airfoil at various times are shown in Figure 106. As the freestream velocity suddenly increases due to the wind gust, the separation point is pushed downstream toward the trailing edge. But when the wind gust starts to diminish, the separation point begins to move back and even slightly passes its original (pre-wind gust)

position. As the freestream velocity continues to stabilize at a velocity slightly higher than the original velocity, the separation point gets close to steady state flow value.

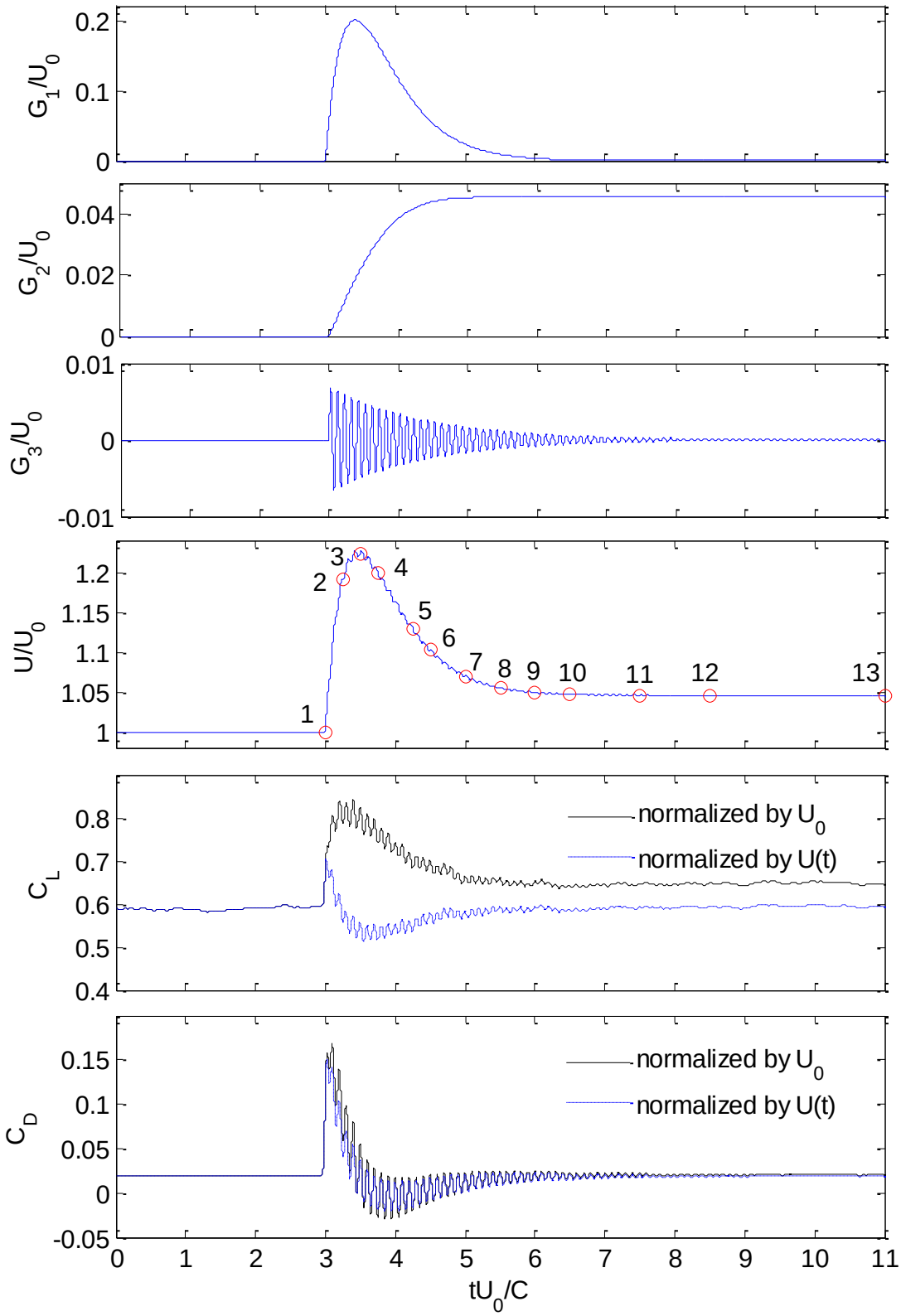

Figure 105: Time variations of the wind gust model parameters, velocity and lift and drag coefficients induced by the wind gust. C_L and C_D are computed by normalizing the lift and drag forces with U_0 and U(t), both.

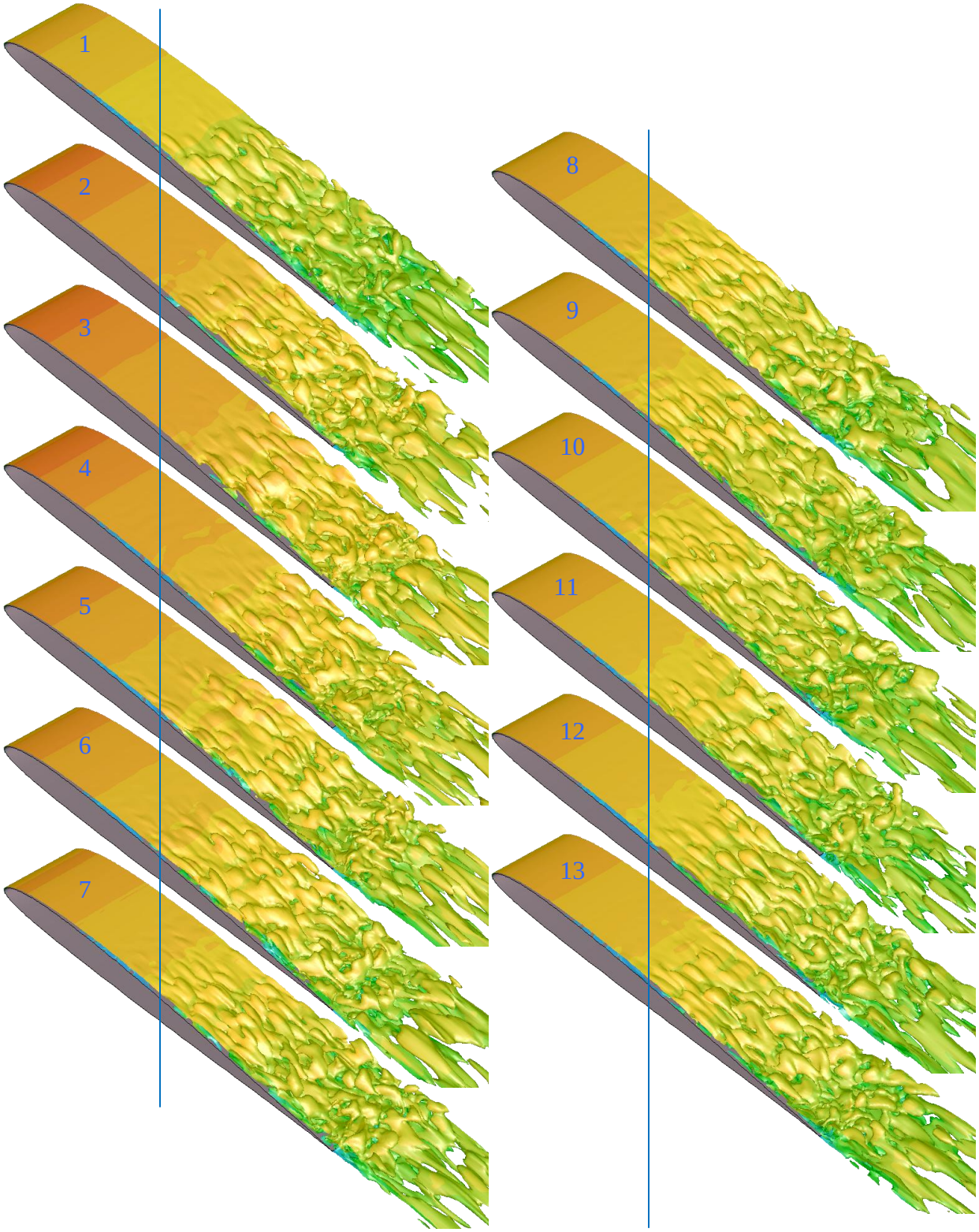

Figure 106: Instantaneous iso-surfaces of z-vorticity ($\omega_z C/U_0 = -10$) simulated by LES with wind gust at different times. The numbers on figures match the times in Figure 105.

6. Summary and Conclusions

Various methods are used to study flows around the SD7003 airfoil at different flow conditions. First, linear stability methods are used to investigate the local and global instability of the time- and spanwise-averaged two-dimensional base flow. Second, large eddy simulation (LES) method is used to simulate steady and unsteady freestream flows around the airfoil.

For the stability analysis, the LSB region of mean (time- and spanwise-averaged) flow field around the SD7003 airfoil at Reynolds number of 60,000 and AoA of $4°$ is employed. The base flow is obtained using a compressible model and an implicit LES solve. The eigenvalue system is solved in the global stability analysis and the classic Rayleigh equation is solved in the local stability analysis. The maximum growth rates obtained from the two methods are in agreement, and both methods correctly predict that the flow is unstable and will transition to turbulence.

To validate the LES method, a number of flows over SD7003 airfoil with steady freestream are simulated, and the results are compared to available numerical and experimental data. The LES results are found to compare reasonably well with other LES data in the literature. The LES results are also consistent with the experimental data, despite discrepancies among the experimental data obtained from different facilities.

The effect of flow three-dimensionality is studied by comparing two-dimensional (2D) and 3D solutions of flow over SD7003 airfoil. The 2D and 3D solutions are found to be generally different. While the difference in instantaneous velocity, pressure and vorticity fields are quite significant, the global quantities like the lift or drag coefficients are not very different unless in extreme situations in unsteady flows. The 2D solutions fail to capture the 2D to 3D transition due to lack of vortex stretching term and spanwise flow variables.

The main objective of this thesis is to study the aerodynamic response of the SD7003 airfoil to unsteady freestream flows. Three types of unsteady freestream conditions are considered. In the first type, AoA is fixed at 4°, while the freestream velocity magnitude varies periodically with mean Reynolds number of 60,000, reduced frequencies ranging from $\pi/8$ to 2π, and normalized oscillation amplitudes of 0.183 and 0.366. In the second type, the freestream velocity magnitude is fixed at Reynolds number of 60,000, while the freestream flow AoA varies periodically around the mean AoA value of 4° with the reduced frequency ranging from $\pi/8$ to 2π and the oscillation amplitudes of 4° and 8°. In the third type of unsteady flows considered in this thesis, a wind gust model is applied to the freestream flow, causing sudden increase and subsequent gradual decrease in velocity magnitude.

For flows with oscillating freestream velocity magnitude, the oscillations of aerodynamic forces, vorticity magnitude, separation and reattachment points are studied in details. Our results indicate that the amplitudes of lift and drag coefficients increase as the reduced frequency and amplitude of freestream velocity magnitude increase. However, the freestream velocity oscillation does not noticeably change the mean lift and drag coefficients from their steady mean freestream values. There is a phase shift between the aerodynamic forces and the freestream oscillation, which is mainly a function of reduced frequency. Compared to the inviscid theory, the lift coefficient obtained from the LES simulations have significantly higher amplitudes, while phase shifts are predicted similarly by the theory and simulation. The oscillating freestream velocity magnitude causes the vorticity field to change slightly during a cycle. For the cases studied, the changes in vorticity field are not significant enough to show a clear trend. However, the integral of the vorticity magnitude along the airfoil wall normal and tangent, n and s ($\int\int|\Omega|dnds$) shows strong correlation with the freestream velocity magnitude. The root-mean-

square (RMS) values of flow, calculated for the case with the highest reduced frequency and the largest amplitude indicate that the fluctuations in various velocity components represented by velocity RMS values are quite the same at different phases of a cycle. The intensity of fluctuations in x-velocity (u′) is slightly higher than that of y-velocity (v′), while the fluctuation of z-velocity (w′) has a much lower magnitude compared to the other two velocity components. Our results also indicate that the separation and reattachment points oscillate over a wider range as the reduced frequency and freestream amplitude increase.

Compared to the flows with oscillating freestream velocity magnitude, the flows with oscillating freestream direction have some similar features but are also different in some respects. The amplitudes of lift and drag coefficient increase as the reduced frequency and amplitude of oscillations in flow AoA increase. However, the lift amplitude is one order of magnitude larger than the drag amplitude. The phase shift between aerodynamic forces and freestream AoA is significantly affected by the reduced frequency. Compared to the flow with steady freestream condition, the mean lift is almost unchanged; but, the mean drag is reduced due to the Katzmayr effect. It is shown that lower reduced frequency and higher amplitude of oscillations in AoA lead to bigger reduction in drag. The amplitude and phase shift of the lift coefficient compare quite well with the inviscid theory developed for a pitching airfoil in a steady freestream, while there is significant difference in the mean lift. At low reduced frequencies and high AoA amplitudes, the vorticity field changes dramatically during a cycle, and this is related to the wide variations in the separation point. At high reduced frequencies, the vorticity field shows less variation in time, but strong vortex shedding at the trailing edge. The strong vortex shedding causes a wide variation in the skin friction coefficient near the trailing edge. For the case with the highest

reduced frequency and the largest amplitude of oscillations in flow AoA, the magnitude of velocity fluctuations is nearly unchanged in different phases.

Based on the mean separation and reattachment points calculated for unsteady flows with freestream velocity magnitude and direction (or AoA) oscillations, it is shown that the oscillations in freestream velocity, either in magnitude or direction, delay the mean separation and promote earlier reattachment of the boundary layer up to the point that the mean flow becomes fully attached.

Simulations conducted with the wind gust model shows sudden increase in the aerodynamic load at the beginning of the gust. Generally, the aerodynamic forces behave the same way as the freestream velocity but they show relatively high sensitivity to the small changes in freestream flow.

The current work can be expanded in several ways if substantially better computational resources become available. Stability analysis can be performed on finer mesh for more detailed analysis of the onset of instability over a bigger region to develop a broader and better picture of the flow instability. For flows with unsteady freestream, finer meshes should be used to obtain details of the flow in regions away from the airfoil and in the wake particularly for flows at high AoA. Much longer simulations are also needed for capturing the response of flow to very low frequency oscillations in the freestream. These details may provide a clearer picture of the development of boundary layer and wake vortices under the effect of oscillating freestream.

APPENDICES

APPENDIX A

The perturbation equations (13)-(16) are solved with the finite element method. For this, the velocity and pressure eigenfunctions are interpolated as

$$\hat{\mathbf{v}} = \Phi_\alpha \hat{v}_\alpha$$
$$\hat{p} = \Phi_\alpha \hat{p}_\alpha \qquad (\alpha = 1, 2, \cdots, n)$$

where $\hat{v}_\alpha$ and $\hat{p}_\alpha$ are the node values, Φ_α are the shape functions, and n is the number of grid nodes in an element. The coefficient matrices in Equation (19) for a 2D base flow are obtained via the following equations.

$$A = \begin{bmatrix} A_{uu} & A_{uv} & A_{uw} & A_{up} \\ A_{vu} & A_{vv} & A_{vw} & A_{vp} \\ A_{wu} & A_{wv} & A_{ww} & A_{wp} \\ A_{pu} & A_{pv} & A_{pw} & A_{pp} \end{bmatrix}, \qquad B = \begin{bmatrix} M & & & \\ & M & & \\ & & M & \\ & & & M \end{bmatrix}$$

$$A_{uu} = -\left\{ A_c + A_{ux} + \mathrm{R_e}^{-1} \left[(S + k^2 M) + \frac{1}{3} D_{xx} \right] \right\}$$
$$A_{uv} = -\left(A_{uy} + \frac{1}{3} \mathrm{R_e}^{-1} D_{xy} \right)$$
$$A_{uw} = -\frac{1}{3} k \, \mathrm{R_e}^{-1} C_x^T$$
$$A_{up} = M_a{}^{-1} C_x{}^T$$
$$A_{vu} = -\left(A_{vx} + \frac{1}{3} \mathrm{R_e}^{-1} D_{yx} \right)$$
$$A_{vv} = -\left\{ A_c + A_{vy} + \mathrm{R_e}^{-1} \left[(S + k^2 M) + \frac{1}{3} D_{yy} \right] \right\}$$
$$A_{vw} = -\frac{1}{3} \mathrm{R_e}^{-1} k C_y^T$$
$$A_{vp} = M_a{}^{-1} C_y^T$$
$$A_{wu} = -\frac{1}{3} \mathrm{R_e}^{-1} k C_x$$
$$A_{wv} = -\frac{1}{3} \mathrm{R_e}^{-1} k C_y$$

$$A_{ww} = -\left\{ A_c + \mathrm{R_e}^{-1}\left[(S + k^2 M) + \frac{1}{3} k^2 M \right] \right\}$$

$$A_{wp} = {M_a}^{-1} kM$$

$$A_{pu} = -\left(A_{px} + {M_a}^{-1} C_x \right)$$

$$A_{pv} = -\left(A_{py} + {M_a}^{-1} C_y \right)$$

$$A_{pw} = -k{M_a}^{-1} M$$

$$A_{pp} = -A_c$$

The elemental matrices are obtained from the following equations.

$$M = \int \Phi_\alpha \Phi_\beta d\Omega \qquad (\alpha, \beta = 1, 2, \cdots, n)$$

$$A_c = \int \Phi_\alpha \left(\Phi_\gamma U_\gamma \Phi_{\beta,x} + \Phi_\gamma V_\gamma \Phi_{\beta,y} \right) d\Omega \qquad (\gamma = 1, 2, \cdots, n)$$

$$A_{ux} = \int \Phi_\alpha \Phi_\beta \Phi_{\gamma,x} U_\gamma d\Omega$$

$$A_{uy} = \int \Phi_\alpha \Phi_\beta \Phi_{\gamma,y} U_\gamma d\Omega$$

$$A_{vx} = \int \Phi_\alpha \Phi_\beta \Phi_{\gamma,x} V_\gamma d\Omega$$

$$A_{vy} = \int \Phi_\alpha \Phi_\beta \Phi_{\gamma,y} V_\gamma d\Omega$$

$$A_{px} = \int \Phi_\alpha \Phi_\beta \Phi_{\gamma,x} P_\gamma d\Omega$$

$$A_{py} = \int \Phi_\alpha \Phi_\beta \Phi_{\gamma,y} P_\gamma d\Omega$$

$$C_x = \int \Phi_{\alpha,x} \Phi_\beta d\Omega$$

$$C_y = \int \Phi_\alpha \Phi_{\beta,y} d\Omega$$

$$D_{xx} = \int \Phi_{\alpha,x} \Phi_{\beta,x} d\Omega$$

$$D_{xy} = \int \Phi_{\alpha,x} \Phi_{\beta,y} d\Omega$$

$$D_{yx} = \int \Phi_{\alpha,y} \Phi_{\beta,x} d\Omega$$

$$D_{yy} = \int \Phi_{\alpha,y} \Phi_{\beta,y} d\Omega$$

$$S = D_{xx} + D_{yy}$$

APPENDIX B

The plots of z-vorticity iso-surface not shown in Section 5.1.2 for flows with oscillating freestream speed are presented here.

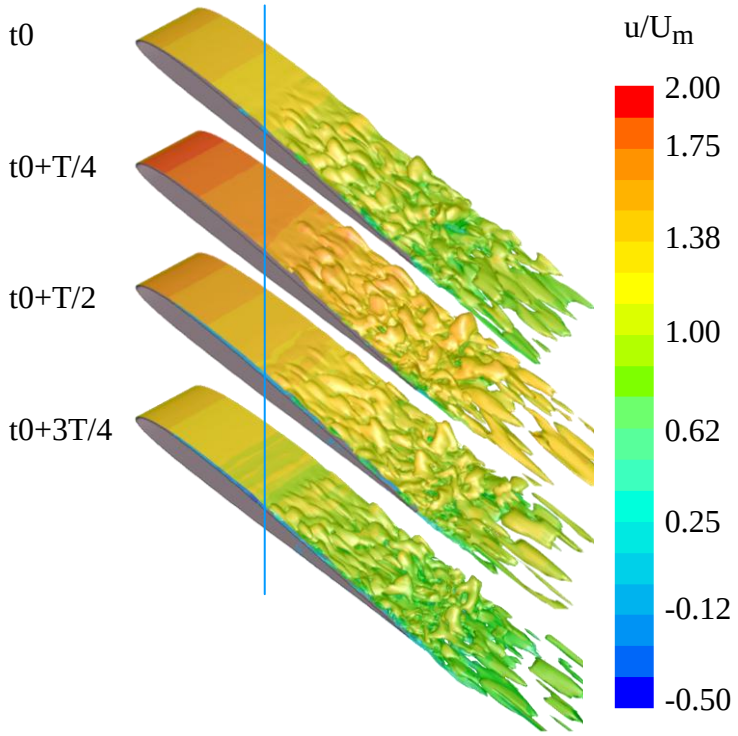

Figure 107: Instantaneous iso-surfaces of z-vorticity ($\omega_z C/U_m = -10$) for case U2 with $k = \pi$ and $\sigma = 0.183$.

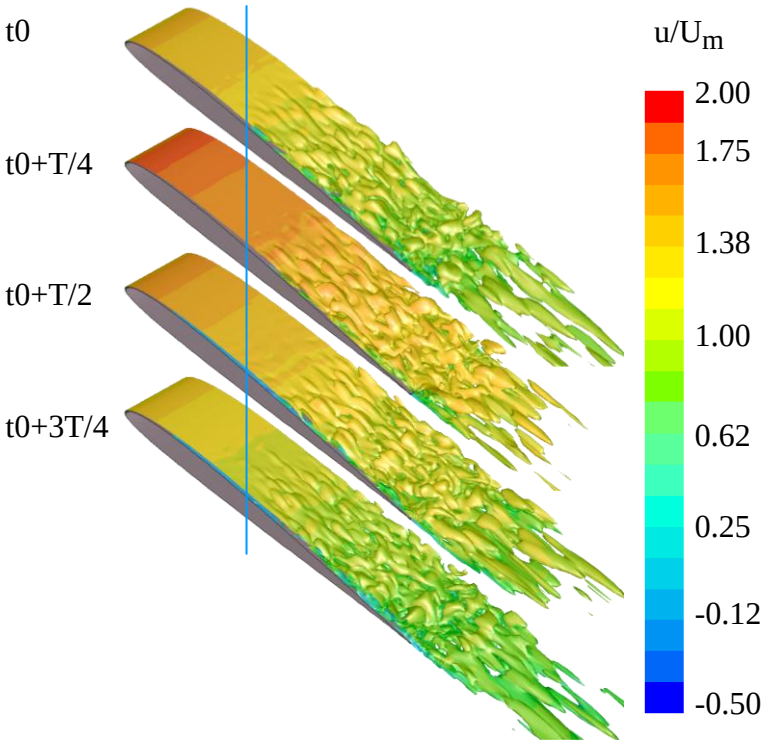

Figure 108: Instantaneous iso-surfaces of z-vorticity ($\omega_z C/U_m = -10$) for case U3 with $k = \pi/2$ and $\sigma = 0.183$.

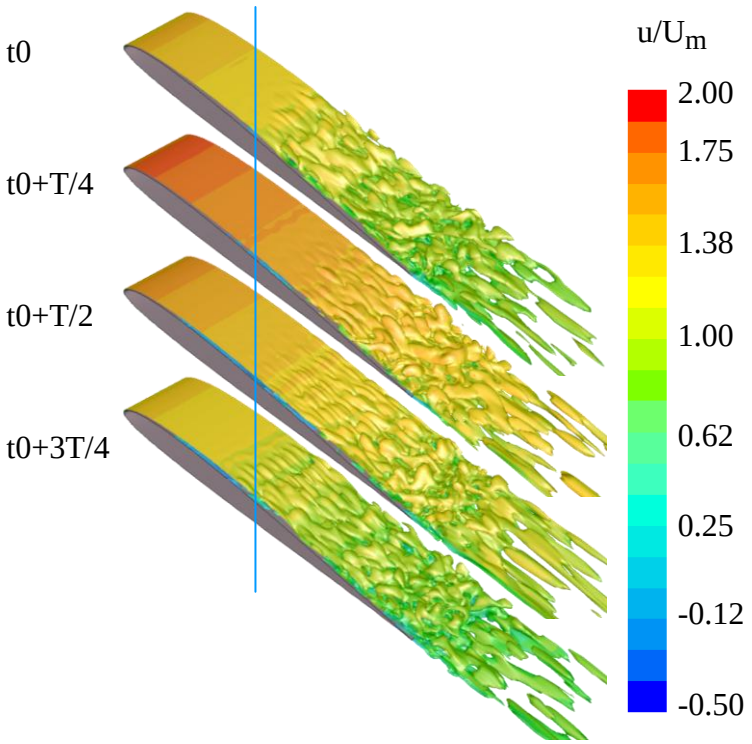

Figure 109: Instantaneous iso-surfaces of z-vorticity ($\omega_z C/U_m = -10$) for case U4 with $k = \pi/4$ and $\sigma = 0.183$.

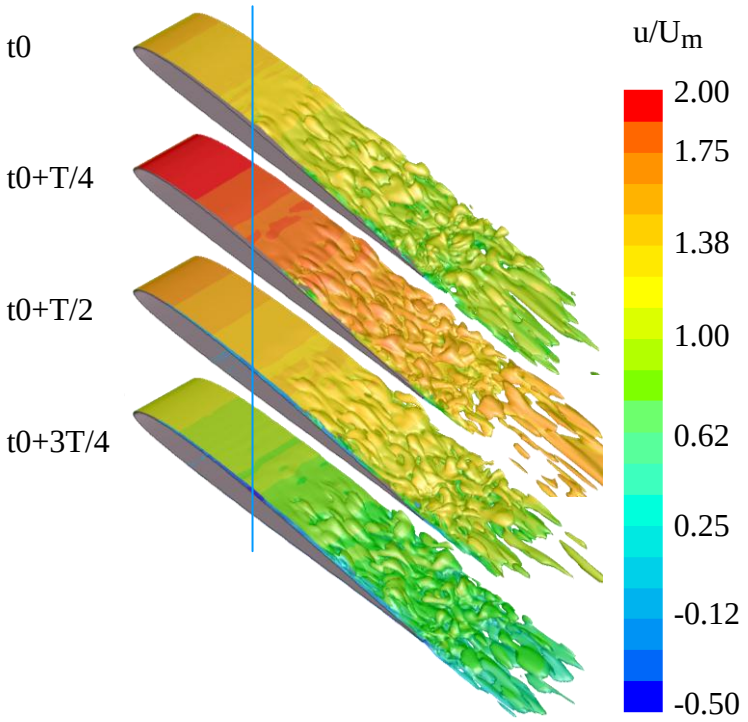

Figure 110: Instantaneous iso-surfaces of z-vorticity ($\omega_z C/U_m = -10$) for case U7 with $k = \pi$ and $\sigma = 0.366$.

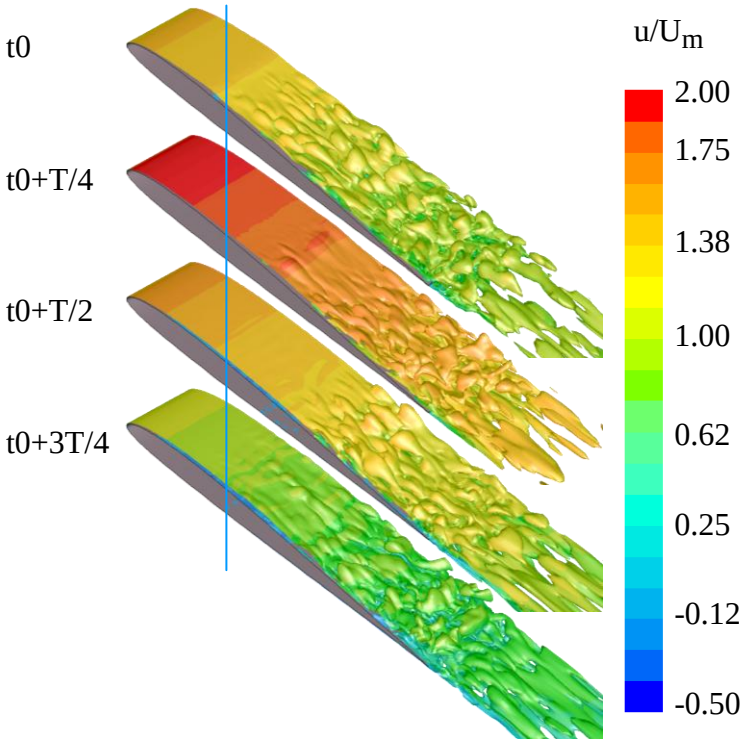

Figure 111: Instantaneous iso-surfaces of z-vorticity ($\omega_z C/U_m = -10$) for case U8 with $k = \pi/2$ and $\sigma = 0.366$.

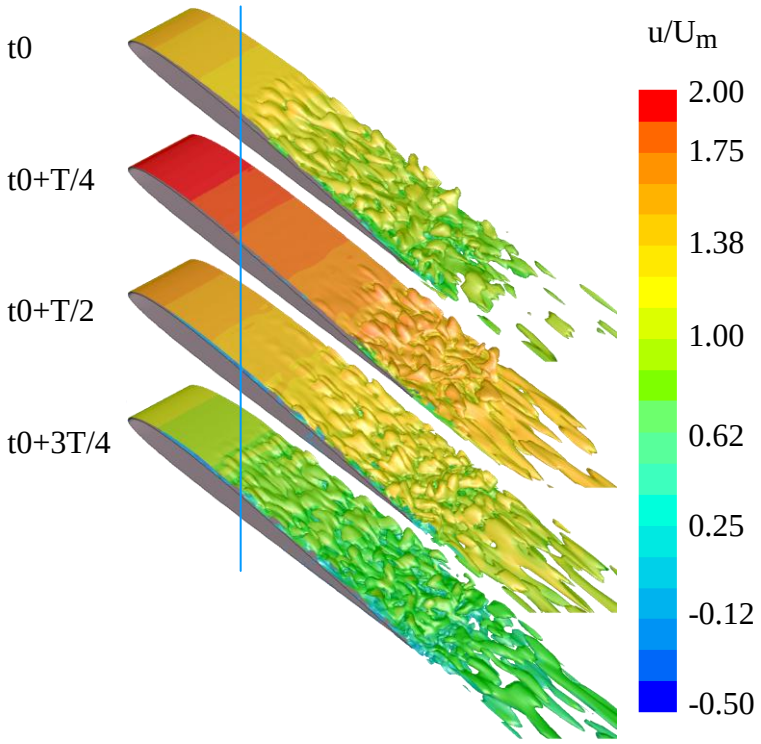

Figure 112: Instantaneous iso-surfaces of z-vorticity ($\omega_z C/U_m = -10$) for case U9 with $k = \pi/4$ and $\sigma = 0.366$.

APPENDIX C

The plots of z-vorticity iso-surface not shown in Section 5.2.2 for flows with oscillating freestream AoA are presented here.

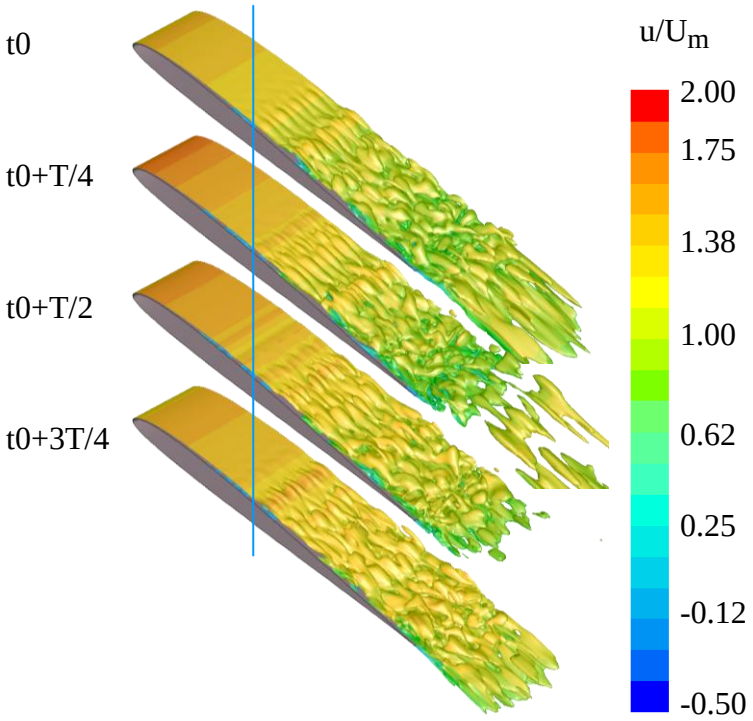

Figure 113: Instantaneous iso-surfaces of z-vorticity ($\omega_z C/U_m = -10$) for case A2 with $k = \pi$ and $\alpha_f = 4^\circ$.

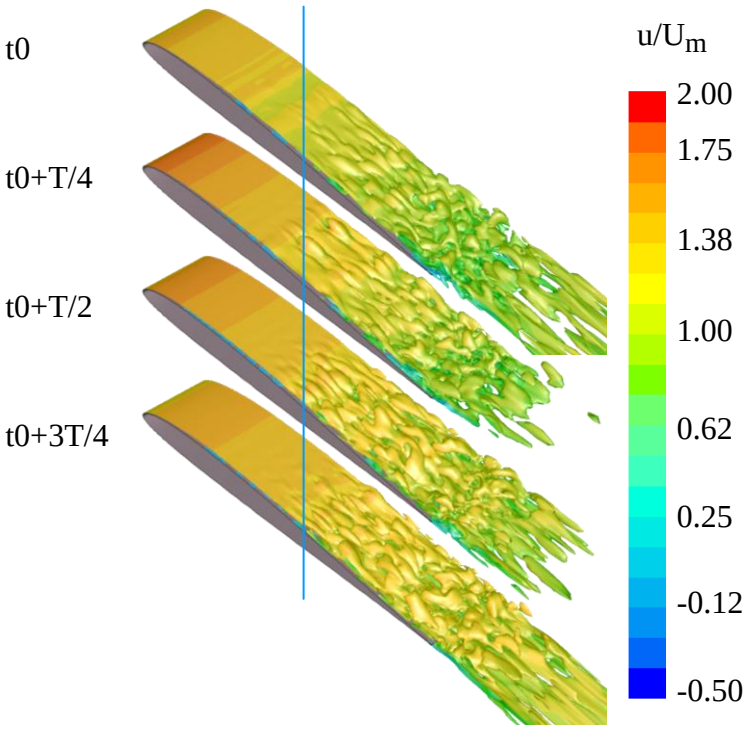

Figure 114: Instantaneous iso-surfaces of z-vorticity ($\omega_z C/U_m = -10$) for case A3 with $k = \pi/2$ and $\alpha_f = 4^\circ$.

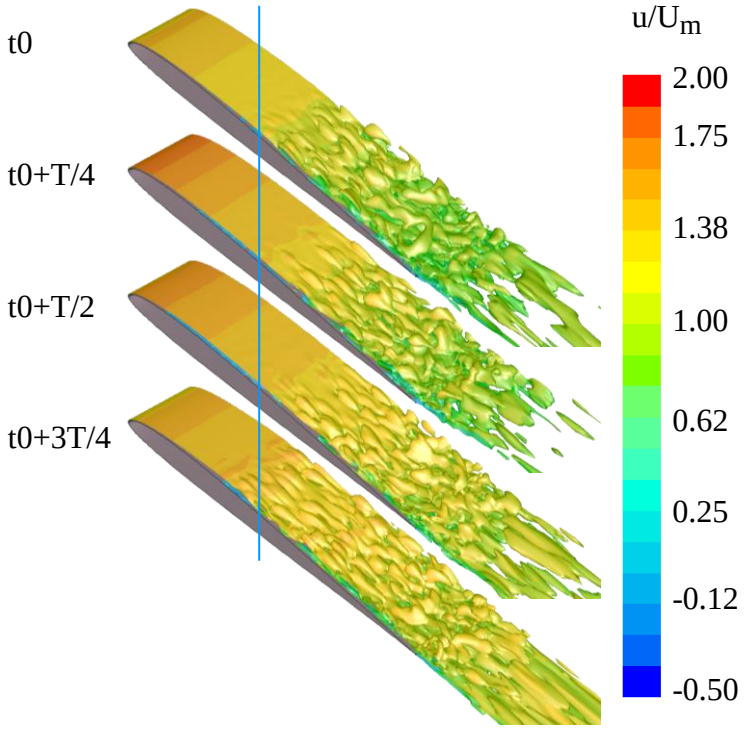

Figure 115: Instantaneous iso-surfaces of z-vorticity ($\omega_z C/U_m = -10$) for case A4 with $k = \pi/4$ and $\alpha_f = 4^\circ$.

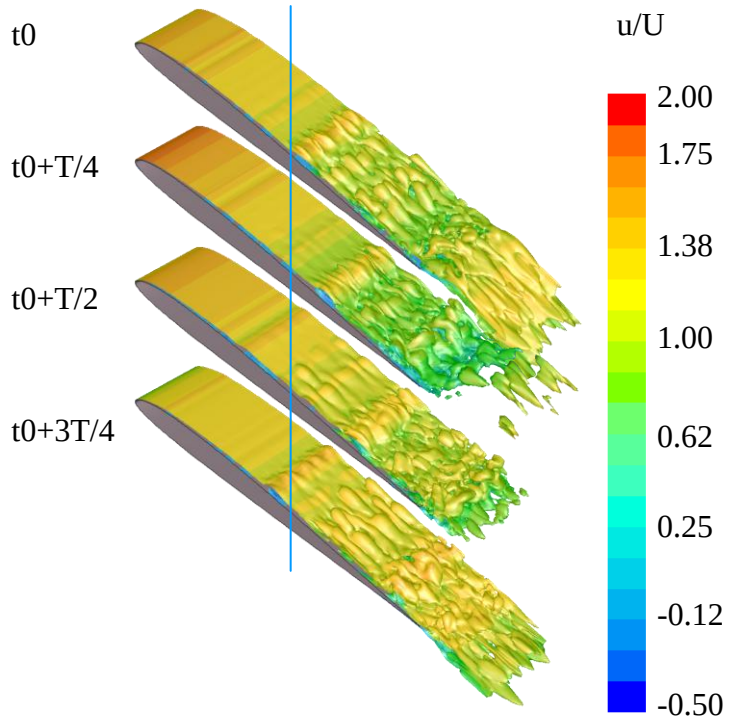

Figure 116: Instantaneous iso-surfaces of z-vorticity ($\omega_z C/U_m = -10$) for case A7 with $k = \pi$ and $\alpha_f = 8^\circ$.

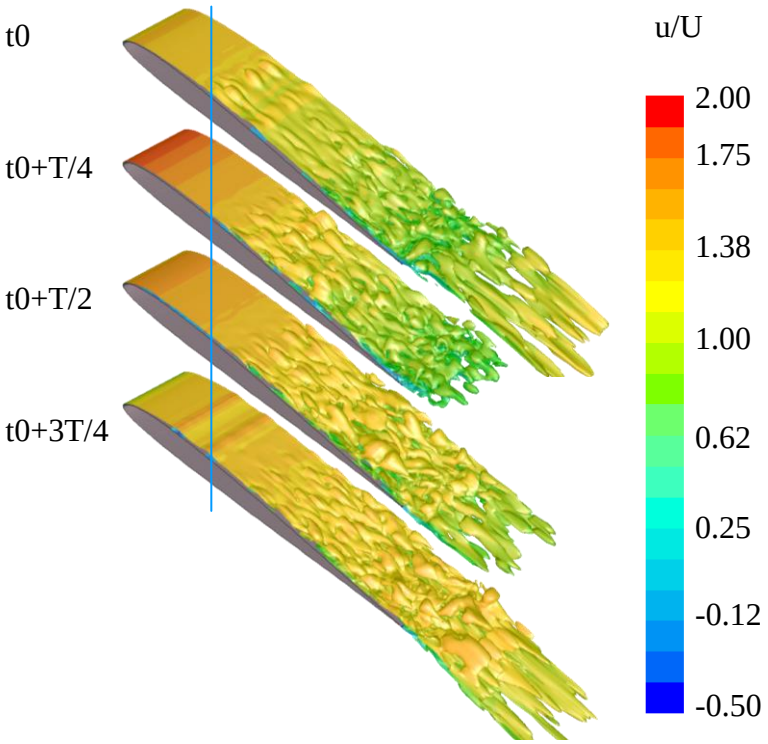

Figure 117: Instantaneous iso-surfaces of z-vorticity ($\omega_z C/U_m = -10$) for case A8 with $k = \pi/2$ and $\alpha_f = 8^\circ$.

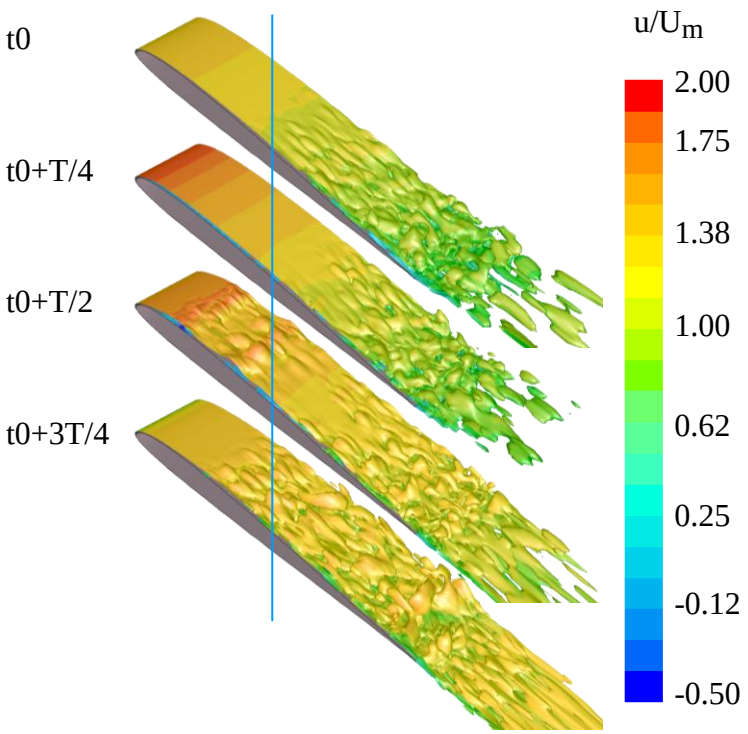

Figure 118: Instantaneous iso-surfaces of z-vorticity ($\omega_z C/U_m = -10$) for case A9 with $k = \pi/4$ and $\alpha_f = 8^\circ$.

BIBLIOGRAPHY

BIBLIOGRAPHY

[1] Jones, B. M., "Stalling," Journal of the Royal Aeronautical Society, Vol. 38, 1938, pp. 747–770.

[2] Young, A. D., and Horton, H. P., "Some Results of Investigation of Separation Bubbles," AGARD Conference Proceedings, Vol. 4, AGARD, London, 1966, pp. 779–811.

[3] Tani, I., "Low Speed Flows Involving Bubble Separations," Progress in Aeronautical Sciences, Pergamon, New York, 1964, pp. 70–103.

[4] Tezuka, A., "Global stability Analysis of Attached or Separated Flows over a NACA.0012 Airfoil," AIAA Paper 2006-1300.

[5] Hammond, D. A. and Redekopp, "Local and Global Instability Properties of Separation Bubbles," Eur. J. Mech. B/Fluids, Vol. 2, 1998, pp. 145-164.

[6] Theofilis, V., Hein, S. and Dallmann, U., "On the Origins of Unsteadiness and Three-Dimensionality in a Laminar Separation Bubble," Phil. Trans. Roy. Soc. Lond. A. Vol. 358, 2000, pp. 3229-3246.

[7] Galbraith, M. and Visbal, M., "Implicit large Eddy Simulation of Low Reynolds Number Flow Past the SD7003 Airfoil," AIAA Paper 2008-225.

[8] Radespiel, R., Windte, J., and Scholz, U., "Numerical and Experimental Flow Analysis of Moving Airfoils with Laminar Separation Bubbles," AIAA Paper 2006-501, Jan. 2006.

[9] Ol, M. V., McAuliffe, B. R., Hanff, E. S., Scholz, U., and Kähler, C., "Comparison of Laminar Separation Bubble Measurements on a Low Reynolds Number Airfoil in Three Facilities," AIAA Paper 2005-5149, Jun. 2005.

[10] Katz, A., Naguib, A., Koochesfahani, M., "Investigation of a low Reynolds number airfoil using molecular tagging velocimetry", American Physical Society, 62nd Annual Meeting of the APS Division of Fluid Dynamics, November 22-24, 2009.

[11] Katz, A., "Molecular Tagging Velocimetry Measurements of the Low-Reynolds-Number Flow Around an SD7003 Airfoil", Master Thesis, Michigan State University, 2010

[12] Olson, D., "Facility and Flow Dependence Issues Influencing the Experimental Characterization of a Laminar Separation Bubble at Low Reynolds Number," Master Thesis, Michigan State University, 2011.

[13] Olson, D., Katz, A., Naguib, A., Koochesfahani, M., Rizzetta, D., and Visbal, M., "An Investigation of the Effect of Freestream Turbulence on the Laminar Separation Bubble on

an SD7003 Airfoil", AIAA 2011-395, 49th AIAA Aerospace Sciences Meeting Including The New Horizons Forum and Aerospace Exposition , 4-7 January 2011, Orlando, Florida..

[14] Radespiel, R., Graage, K., and Brodersen, O., "Transition Predictions Using Reynolds-Averaged Navier–Stokes and Linear Stability Analysis Methods," AIAA Paper 91-1641, June 1991.

[15] Stock, H. W., and Haase, W., "A Feasibility Study of e^N Transition Prediction in Navier–Stokes Methods for Airfoils," AIAA Journal, Vol. 37, No. 10, 1999, pp. 1187–1196.

[16] Yuan, W., Khalid, M., Windte, J., Scholz, U., and Radespiel, R., "An Investigation of low Reynolds-Number Flows Past Airfoils," 23rd AIAA Applied Aerodynamics Conference, Toronto, AIAA Paper 2005-4607.

[17] Lian Y., and Shyy W., "Laminar-turbulent Transition of a Low Reynolds Number Rigid or Flexible Airfoil," AIAA Journal, vol. 45, No. 7, 2007.

[18] Sherer, S. and Visbal, M., "Multi-resolution Implicit Large Eddy Simulations Using a High-Order Overset-Grid Approach", International Journal for Numerical Methods in Fluids, Vol. 55, pp. 455-482, 2007.

[19] Rizzetta, D., Visbal, M. and Morgan, P., "A High-Order Compact Finite-Difference Scheme for Large-Eddy Simulation of Active Flow Control", Progress in Aerospace Science, Vol. 44, pp. 397-426, 2008.

[20] Galbraith, M., "Implicit Large Eddy Simulation of Low-Reynolds-Number Transitional Flow Past the SD7003 Airfoil", Master Thesis, University of Cincinnati, 2009.

[21] Visbal, M., Gaitonde, D. and Roy, S., "Control of Transitional and Turbulent Flows Using Plasma-Based Actuators", AIAA Paper 2005-5302, 36th AIAA Plasmadynamics and Lasers Conference, Toronto, Ontario, June 6-9, 2005.

[22] Bohl, D. and Koochesfahani, M., "MTV measurements of the Vortical Field in the Wake of an Airfoil Oscillating at High Reduced Frequency", Journal of Fluid Mechanics, Vol. 620, pp. 63-68, 2009.

[23] Visbal, M., "High-Fidelity Simulation of Transitional Flows Past a Plunging Airfoil", 47th AIAA Aerospace Sciences Meeting Including The New Horizons Forum and Aerospace Exposition 5 - 8 January 2009, Orlando, Florida.

[24] McGowan, G., Gopalarathnam, A., OL, M., Edwards, J., and Fredberg, D., "Computation vs. Experiment for High-Frequency Low-Reynolds-Number Airfoil in Pitch and Plunge," AIAA Paper 2008-0653, 2008.

[25] Koochesfahani, M., "Vortical Patterns in the Wake of an Oscillating Airfoil", AIAA Journal, Vol. 27, No. 9, 1989.

[26] Theodorsen, T., "General Theory of Aerodynamic Instability and the Mechanism of Flutter," N.A.C.A. TR No. 496, May 1934.

[27] von Kármán, T. and Sears, W. R., "Airfoil theory for non-uniform motion," J. Aeronaut. Sci. 5, 1938, 379 – 390.

[28] "Unsteady Aerodynamics for Micro Air Vehicles," RTO Technical report, TR-AVT-149, 2010.

[29] Burgmann, S., Dannemann, J., Schröder, W. "Time-resolved and volumetric PIV measurements of a transitional separation bubble on an SD7003 airfoil". Experiments in Fluids, 44, 2007, pp. 609-622.

[30] Isaacs, R., "Airfoil Theory for Flows of Variable Velocity," Journal of the Aeronautical Sciences, Vol. 12, No. 1, 1945, pp. 113-117.

[31] Greenberg, J. M., "Airfoil in Sinusoidal Motion in a Pulsating Stream," N.A.C.A. Report No. 1326, June 1947.

[32] Gursul, I., Lin, H., and Ho, C., "Effects of Time Scales on Lift of Airfoils in an Unsteady Stream", AIAA Journal, Vol. 32, No. 4, April 1994.

[33] Katzmayr, R., "Effect of Periodic Changes of Angle of Attack on Behavior of Airfoils", N.A.C.A. Technical Memorandum No. 147, 1922.

[34] Toussaint, Kerneis, Girault, "Experimental investigation of the effect of an oscillating airstream (Katzmayr effect) on the characteristics of airfoils," N.A.C.A. Technical Report No.202, 1924.

[35] Williams, D., Quach, V., Kerstens, W., Buntain, S., Tadmor, G., Rowley, C., Colonius, T., "Low-Reynolds Number Wing Response to an Oscillating Freestream with and without Feed Forward Control," AIAA 2009-143, 47th AIAA Aerospace Sciences Meeting Including The New Horizons Forum and Aerospace Exposition , 5-8 January 2009, Orlando, Florida.

[36] Gharali, K. and Johnson, DA., "Numerical modeling of an S809 Airfoil under Dynamic Stall, Erosion and High Reduced Frequencies", Appl Energy (2011), doi:10.1016/j.apenergy.2011.04.037.

[37] Ding Y, and Kawahara M., "Linear Stability of Impressible Flow Using a Mixed Finite Element Method," J. Comp. Phys, Vol. 139, 1998, pp. 243-273.

[38] Malkus, D., "Eigenproblems associated with the discrete LBB condition for incompressible finite elements," International Journal of Engineering Science, Vol. 19, 10, 1981.

[39] Frank M. White, "Viscous Fluid Flow (Third Edition)," McGraw-Hill, NY, 2006.

[40] Huerre P., and Monkewitz P. A., "Absolute and Convective Instability in Free Shear Layers," J. Fluid Mech, vol 159, 1985, pp. 151-168.

[41] Triantafyllou G. S., Triantafyllou M. S., and Chryssostomidis C., "On the formation of vortex streets behind stationary cylinders," J. Fluid Mech. Vol. 170, 1986, pp. 461-477.

[42] Zhuang, M., Dimotakis, P. E. and Kubota, T. [1990], "The Effect of Walls on a Spatial Growing Supersonic Shear Layer," Physics of Fluids, 2(4), 599-604.

[43] Zhuang, M., Kubota, T. and Dimotakis, P. E. "On the instability of inviscid, compressible free shear layers," AIAA Journal, Vol. 28, No.10, 1990, pp. 1728-1733.

[44] Theofilis, V., Duck, P., and Owen, J., "Viscous Linear Stability Analysis of Rectangular Duct and Cavity Flows", J. Fluid Mech. Vol. 505, 2004, pp. 249-268.

[45] ANSYS Inc, "FLUENT 6.3 Manual", 2008

[46] Pope, S., "Turbulent Flows", Cambridge University Press, UK, 2000.

[47] BARDINA, J., FERZIER, J. H. and REYNOLDS, W. C., "Improved subgrid-scale models for large eddy simulation", AIAA paper, 78, 1980.

[48] Hinze, J., "Turbulence", McGraw-Hill Publishing Co., New York, 1975.

[49] Nicoud, F. and Ducros, F., "Subgrid-Scale Stress Modeling Based on the Square of the Velocity Gradient Tensor", Flow, Turbulence, and Combustion, 62(3):183–200, 1999.

[50] Guleren, K., "Large-Eddy Simulation of Wall-Bounded Flows Subjected to Curvature and Rotation", PhD Dissertation, University of Manchester, 2007.

[51] Hodge, J. K., Stone, A. L., and Miller, T. E., "Numerical Solution for Airfoils near Stall in Optimized Boundary-Fitted Curvilinear Coordinates," AIAA Journal, Vol. 17, No. 5, 1979, pp. 458-464.

[52] Burgmann, S., Schröder, W. Investigation of the vortex induced unsteadiness of a separation bubble via time-resolved and scanning PIV measurements". Experiments in Fluids, 45, 2008, pp. 675-691.

[53] Greenberg, J.M., "Airfoil in Sinusoidal Motion in a Pulsating Stream," N.A.C.A. TN-1326, 1947.

[54] Leishman, J. G., "Principles of Helicopter Aerodynamics", Cambridge University Press, 2000.

[55] Ober, S., "Note on the Katzmayr effect on airfoil drag," N.A.C.A. Technical Report No. 214, 1925.

[56] Sorensen, P., Hansen, A., Andre, P., Rosas, C., "Wind models for simulation of power fluctuations from wind farms". Journal of Wind Engineering and Industrial Aerodynamics, Vol. 90, 2002, pp. 1381-1402.

[57] Gast, K., "A Comparison of Extreme Wind Events as Sampled in the 2002 Thunderstorm Outflow Experiment", Master's Thesis, Texas Tech University, Lubbock.

[58] Hemida, H., Krajnovic, S., "Transient Simulation of the Aerodynamic Response of a Double-Deck Bus in Gusty Winds". Journal of Fluids Engineering, Vol. 131, 2009.